2009

Pyrolysis oil combustion characteristics and exhaust emissions in a swirl-stabilized flame

Derek Wissmiller
Iowa State University

Recommended Citation

Wissmiller, Derek, "Pyrolysis oil combustion characteristics and exhaust emissions in a swirl-stabilized flame" (2009). *Graduate Theses and Dissertations*. 10889.
http://lib.dr.iastate.edu/etd/10889

Pyrolysis oil combustion characteristics and exhaust emissions in a swirl-stabilized combustor

by

Derek Wissmiller

A dissertation submitted to the graduate faculty

in partial fulfillment of the requirements for the degree of

DOCTOR OF PHILOSOPHY

Co-majors: Mechanical Engineering; Biorenewable Resources and Technology

Program of Study Committee:
Robert C. Brown, Co-major Professor
Terrence R. Meyer, Co-major Professor
Song-Charng Kong
Brent H.Shanks
Hui Hu

Iowa State University

Ames, Iowa

2009

To my wife, Kristine

TABLE OF CONTENTS

LIST OF FIGURES

LIST OF TABLES

ABSTRACT

An optically accessible domestic-scale swirl-stabilized combustor has been developed to allow for the investigation of combustion characteristics of biomass derived pyrolysis oils in pressure-atomized and air-atomized spray flames. Pine and corn fiber derived pyrolysis oil have been studied, with light fuel oil (LFO) used as a baseline fuel for comparison. Gaseous and particulate exhaust emissions have been measured, and the particulate samples studied with scanning electron microscopy (SEM) to investigate morphology and composition. In-situ visualization studies have been performed by employing high speed imaging of flame luminosity and several laser diagnostic methods including Mie scattering, hydroxyl radical planar induced fluorescence (OH-PLIF), fuel planar laser-induced fluorescence (Fuel-PLIF), and laser induced incandescence (LII). Spray characteristics have been investigated by employing Mie scattering and phase Doppler particle analysis(PDPA). Particulate emissions in pyrolysis oil have been found to consist predominately of unburned fuel residues (cenospheres), rather than soot, with higher emissions than LFO. Cenosphere emissions have been found to be greater for pressure atomization compared to air atomization, lean conditions relative to rich conditions, and low atomization air flowrates compared to high atomization air flowrates. Variation in combustion air preheat temperature from 100 to 400 °C, variation in water content from 23 to 26%, and variation in fuel fixed carbon content from 15 to 51% did not show significant effects on cenosphere characteristics.

CHAPTER 1. INTRODUCTION

1.1 Motivation

Concerns over energy supplies, national security, and global warming have increased interest in the development of liquid fuels from sources other than fossil fuels. Biomass has gained interest as a feedstock for producing liquid fuels because it has a closed carbon cycle. Biomass-derived fast pyrolysis oil has the potential to become one of the lowest cost biofuel options because of its relatively simple production process and its ability to convert lignin to fuel, in addition to cellulose and hemicellulose. Pyrolysis oil is oil is produced through the rapid thermal decomposition of organic material in an oxygen depleted environment followed by a condensation of the vapors to yield a liquid fuel [1-3].

Pyrolysis oil has been demonstrated for use in boilers, turbine, and diesel engines; however, issues with regard to the fuels acidity, ignition characteristics, coking/clogging tendency, and particulate emissions have limited its implementation [4, 5]. Because most of the research in pyrolysis oil combustion has been demonstrative in nature, the combustion characteristics of pyrolysis oil are not well understood. Therefore, the core objective of this research is to develop a better understanding of pyrolysis oil combustion in regards to the operating conditions used during combustion and the chemical and physical properties of the oil.

The majority of researchers who have investigated pyrolysis oil combustion have found particulate emissions to be higher than those of conventional fuels [4, 5]. However, none of these studies have revealed the root causes of the increased emissions and as such, it is of great interest to further investigate the characteristics of particulate emissions in pyrolysis oil combustion.

Given the aforementioned challenges in pyrolysis oil combustion, it seems likely that this fuel would be used initially in boilers or gas turbines, rather than in internal combustion engines. Burners designed for these applications typically employ swirl-stabilized flames, which utilize recirculation of hot combustion products to enhance flame stabilization. Therefore, as part of this research, an optically accessible swirl-stabilized combustion apparatus has been developed, with a design that is based on a domestic scale burner (< 30 kW). Although the primary goal has been in developing a burner which allows for controlled investigation of pyrolysis oil combustion, it is of secondary benefit to study the combustion phenomena at this scale given that domestic heating applications have been suggested as a potential market for pyrolysis oil [6].

1.2 Objectives

Objective 1: To develop an optically accessible combustion apparatus that is capable of achieving stable combustion of pyrolysis oils over a wide range of operating conditions and fuel properties, and which provides adequate control and measurement of key combustion parameters.

Objective 2: To investigate the fundamental characteristics of pyrolysis oil combustion and sprays as they differ from conventional light fuel oil, especially in regard to the production and emission of particulate matter.

Objective 3: To investigate the effects of burner equipment and operating conditions on pyrolysis oil combustion, especially in regard to the production and emission of particulate matter.

Objective 4: To investigate the effects of pyrolysis oil physical and chemical properties on pyrolysis oil combustion characteristics, especially in regard to the production and emission of particulate matter.

1.3 Dissertation Outline

Chapter 2 begins with a description of spray flames, swirl stabilization, combustion chemistry, and combustion exhaust emissions. This is followed by a summary of the current state of the art in pyrolysis oil combustion. Chapter 3 outlines the combustion apparatus that has been developed as part of this research, along with measurement techniques employed to characterize the fuel properties and combustion behavior. Chapter 4 presents the results of this research with detailed discussions of the findings. Chapter 5 summarizes the findings of this work, relating it to prior research in pyrolysis oil combustion and suggesting future studies in this field which are of interest.

CHAPTER 2. LITERATURE REVIEW AND BACKGROUND

2.1 Spray Flames

Combustion of liquid fuels is most often achieved through the ignition of a finely atomized fuel spray [7]. Because of their inherently high volumetric energy density, liquid fuels are often an ideal choice for transportation uses. However, liquid fuels, fuel oils in particular, continue to be used widely in powering turbines, furnaces, and boilers for heat and power generation systems.

Flames are typically categorized broadly as either *premixed* or *diffusion* flames [8]. This designation refers to the condition of the combustion reactants prior to the combustion reaction. A premixed flame is one in which the fuel and oxidizer are uniformly mixed prior to reaction, whereas a diffusion flame is one in which the fuel and oxidizer are initially separated. With this, laminar premixed flames are considered kinetically limited, while laminar diffusion flames are considered mass transfer limited. When turbulence is introduced to a premixed flame, burning velocities are increased because the turbulent eddies in the flow *wrinkle* the reaction sheet, giving it more surface area and allowing it to propagate more rapidly [9]. In a nonpremixed turbulent flame, overall flame speeds are increased from those in a laminar diffusion flame, predominately because the turbulence serves to increase mass transfer rates between the fuel and oxidizer.

In liquid fuel spray flames, the fuel is commonly sprayed directly into the combustion environment where it vaporizes before undergoing a gas phase reaction with the oxidizer [10]. Given that the time required for fuel vaporization is commonly long enough such that liquid fuel droplets exist within the flame region, spray flames are typically nonpremixed, since the fuel vapor must diffuse from the droplet surface to the flame front.

The characteristics of a flame can vary rather significantly with regard to flame size, heat release rates, and pollutant formation depending on the location of the fuel droplets in relation to the flame front. Williams addressed this issue by defining two extremes of spray combustion phenomena [11]. In one limit, termed *homogeneous* combustion, the droplets are considered to fully evaporate before mixing with the oxidizer and burning. In the other extreme, termed *heterogeneous* combustion, the droplets are considered to burn individually, with a diffusion flame enveloping each droplet. This terminology is derived from a consideration of the initial state of the chemical reactants, with fuel (and oxidizer) existing initially in the gas phase for the *homogenous* combustion regime and fuel existing in the liquid phase for *heterogeneous* combustion. However, even in the *heterogeneous* combustion regime fuel is vaporized prior to combustion such that the reaction is purely gas phase, and therefore, homogeneous with regard to the terminology as it is commonly used in Chemistry [10]. Nonetheless, in combustion terminology, flames are still commonly referred to as homogeneous and heterogeneous in the manner set forth by Williams.

Chiu et- al. set forth a somewhat more detailed description of the droplet-flame interaction, outlining four possible scenarios; external sheath combustion, external group combustion, internal group combustion, and single droplet combustion [12]. External sheath combustion is such that the flame surrounds the spray of droplets which includes regions of the spray which are too fuel rich to allow for further vaporization of some of the droplets. External group combustion describes a flame which surrounds a spray of droplets, in which all of the droplets are vaporizing. Internal group combustion describes a flame such that some of the droplets reach beyond the limits of the main flame front, with those droplets surrounded by individual envelope or wake flames. Finally, single droplet combustion describes a spray flame in which every droplet is surrounded by an individual flame.

Whether a flame will be governed predominately by external (homogeneous) combustion or internal (heterogeneous) combustion depends on the rate of oxidizer entrainment into the spray relative to the rate of droplet vaporization [10]. If the oxidizer entrainment is fast relative to droplet vaporization then internal combustion will be favored. However, if the rate of oxidizer entrainment is slow relative to droplet vaporization, then external combustion will likely dominate.

Experimental evidence that external combustion occurs in spray flames is apparent in work carried out by Onuma and Ogasawara et- al. [13, 14]. Combustion studies performed in a nonpremixed turbulent flame with propane and kerosene showed that almost no difference existed between the flame structure and species concentration profiles between the two fuels [13]. This is attributed to the fact that the droplets vaporize rapidly in fuel-rich regions before reaching the flame front. Further studies performed between kerosene and heavy fuel oil, yielded very similar findings, suggesting that this behavior is not strongly dependent upon fuel volatility [14].

When very fine atomization is achieved, the description of internal vs. external combustion becomes moot, because droplets can vaporize so rapidly that they behave as a gaseous fuel [7]. An analytical treatment of a one-dimensional spray flame of an alkane fuel reveals an order of magnitude estimate that for droplets lower than 10 μm, droplets vaporize rapidly enough that they behave as a gaseous fuel [10]. Experimental investigation in to the combustion of a stream of monodispersed tetralin droplets by Burgoyne and Cohen have confirmed this with the finding that for droplet sizes less than 10 μm, flame speeds were the same as that of fully premixed gaseous flames [15]. Therefore, when droplet sizes are very small, volatile liquid fuels behave not only like a gaseous fuel, but moreover the flame behaves as though it were premixed.

In heating and power applications, fine sprays are typically achieved through the use of either pressure or air-assisted atomization [7]. Pressure nozzles force fuel through a small orifice with a large pressure drop to achieve atomization. Both flowrate and droplet size are affected by the fuel pressure delivered to the nozzle. The flowrate through the nozzle is typically proportional to the square root of the pressure difference across the nozzle, making it difficult to achieve a wide turndown ratio.

Air-assist atomization nozzles utilize a secondary flow of a gas (typically air or steam) to pass by the liquid fuel, aiding the atomization process by shearing the liquid into a fine spray [16]. Air atomization nozzles typically achieve finer droplet sizes than pressure nozzles. Further, air atomization nozzles allow for a wide turndown ratio as well as independent control of fuel flowrate and spray quality. However, because air atomization requires additional air (or steam) handling equipment it is more costly to implement than pressure atomization.

Given the turbulent nature of spray formation, droplets produced during atomization have a wide distribution of droplet sizes [17]. It is desirable to consider an *average* droplet diameter when comparing different spray options. This is typically done by calculating the Sauter mean diameter (SMD) from a spray defined as

$$SMD = \frac{\sum nD^3}{\sum nD^2} \tag{2.1}$$

where D is diameter and n is the number of droplets of a particular diameter. This *average* represents a droplet diameter which has the same volume to area ratio as the entire spray; this is a relevant parameter in spray flames given the effects of droplet thermal capacitance and heat and mass transfer rates. Several researchers have developed SMD correlations for pressure and air-assist nozzles under varying conditions. For air atomization nozzles operating under atmospheric conditions with a low viscosity liquid, the SMD is inversely proportional to the relative velocity between the air and liquid [16].

2.2 Flame Stabilization

For a stationary flame, the flow of reactants to the flame zone cannot exceed the speed of flame propagation against the flow of reactants or else flame blow-off will occur [18]. Flame speeds can be increased by increasing the turbulence in the flame; however, for situations requiring high fuel throughput and therefore high speed flows, additional aides may be required to achieve stable combustion.

Two common methods for enhancing flame stabilization in stationary flames are bluff body and swirl stabilization [19]. In bluff body stabilization, an obstruction is placed in the path of the combustion reactants, producing a recirculation zone on the downstream side of the object as shown in Figure 2.1. This allows for recirculation of hot combustion products to the incoming reactants, which serves to ignite the incoming reactants. A disadvantage of bluff body stabilization is that the bluff body can experience fouling, abrasion, and corrosion.

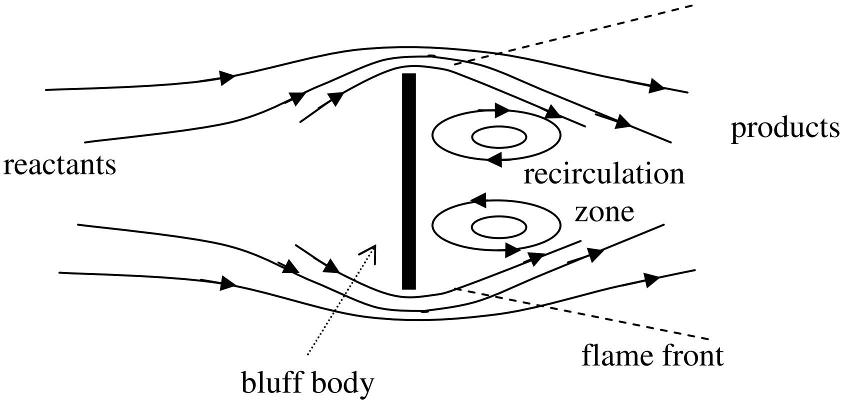

Figure 2.1 Bluff body stabilization of a flame.

In swirl stabilization, a cyclonic flow is produced with flow vanes, a tangentially introduced flow, or mechanical rotation of the flow supply line [19]. The centrifugal forces in the swirling flow produce both radial and axial pressure gradients which establish a recirculation zone in the center of the flow as shown in Figure 2.2. As in the case of bluff body stabilization, this zone allows for recirculation of the hot combustion products which ignite the incoming reactants.

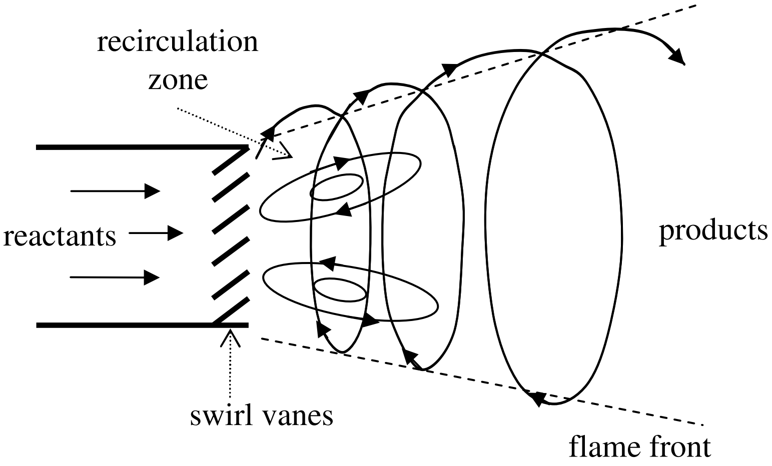

Figure 2.2 Swirl stabilization of a flame.

In swirl-stabilized spray flames, such as those in boilers and gas turbines, the air flow delivered for combustion is commonly swirled around the fuel spray to provide the flame stabilization as shown in Figure 2.3 [19]. Designs which establish good flow matching between the fuel spray and air swirl pattern can reduce pollutant emissions, while improper matching or misalignment can lead to significant increases in pollution and a reduction of flame stability.

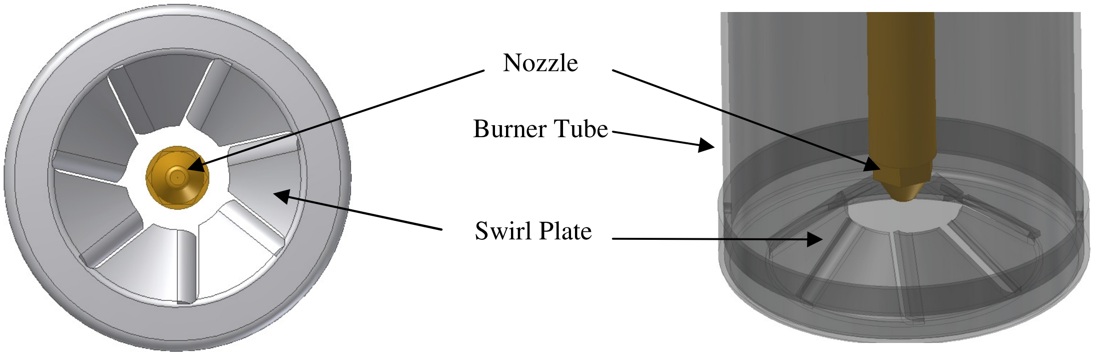

Figure 2.3 Typical fuel nozzle and air swirler configuration.

2.3 Combustion Chemistry and Pollutant Emissions

In ideal combustion of an organic fuel under fuel-lean conditions, hydrogen would be fully converted to water and carbon converted predominately to carbon dioxide with a small equilibrium concentration of carbon monoxide. However, given the rate dependent nature and complex physiochemical phenomena in flames, other reaction products are formed, which can contribute to combustion inefficiencies and/or pollutants. The most significant combustion pollutants are carbon monoxide (CO), unburned hydrocarbons (HC), nitrogen oxides (NOx), sulfur oxides (SOx), and particulate matter (PM) [20].

2.3.1 Carbon Monoxide

Carbon monoxide (CO) forms in flames as part of the combustion reaction pathway, as is indicated by in-flame concentrations which are greater than equilibrium concentration in under adiabatic conditions [20]. Because this trend occurs for premixed flames, as well as diffusion flames, CO production and destruction in flames is considered to be a kinetically controlled phenomenon. Carbon monoxide production rates are typically very rapid and CO oxidation rates are governed by the local flame temperatures and radical concentrations. If the flame temperature is quenched or radicals are eliminated through competing reaction pathways, CO will fail to oxidize, surviving as a stable species in the exhaust.

2.3.2 Unburned Hydrocarbons

Unburned hydrocarbons (HC) typically refer to gaseous fuel species which pass through the combustion environment without oxidizing [21]. Hydrocarbons can fail to burn due to flame quenching or mass transfer limitations between fuel and oxidizer

2.3.3 Nitrogen Oxides

Nitrogen oxides (NOx) are considered to be predominately governed by reaction kinetics [20]. Nitric oxide (NO) appears in combustion emissions as a result three possible mechanisms: 1) *thermal* NOx formation, 2) *prompt* NOx formation, and 3) fuel-bound nitrogen oxidation. All three mechanisms generate NO, which can further react to form nitrogen dioxide (NO_2) and nitrous oxide (N_2O), with the sum of these emissions commonly referred to as NOx.

Thermal NOx formation is governed by three principle reactions shown below, known as the Zeldovich mechanism [22].

$$O + N_2 \rightleftarrows NO + N \tag{1}$$

$$N + O_2 \rightleftarrows NO + O \tag{2}$$

$$N + OH \rightleftarrows NO + H \tag{3}$$

Because of the strong triple bond in the N_2 molecule, very high temperatures are required to break the bond, making the first of these three reactions the rate limiting step in the thermal

NOx mechanism. Given the strong temperature dependence of this mechanism, NO, can be reduced by reducing peak flame temperatures; however, significant cooling can lead to increased CO and HC emissions.

Prompt NOx forms as a result of an interaction of N_2 with the CH radical along the flame front by first producing hydrocyanic acid (HCN) and monatomic nitrogen according to the following reaction [22].

$$CH + N_2 \rightleftarrows HCN + N \quad (4)$$

Once the monatomic nitrogen is formed, NOx can be formed according to reactions (2) and (3) from the Zeldovich mechanism. The production rates of prompt NOx are coupled to the oxidation rates of the hydrocarbon fuel.

Fuel-bound NOx arises as a result of nitrogen present in the fuel, as the name implies [20]. The degree to which fuel-bound nitrogen is converted into NOx is not significantly influenced by the chemical structure of the nitrogen in the fuel, but is rather affected by the local combustion temperatures and stoichiometry, as well as the mass fraction of nitrogen in the fuel. Fuel-bound nitrogen also typically produces HCN and ammonia (NH_3), which may further react to NO. In rich combustion the sum of these components is minimized, such that staged combustion can be employed to reduce the formation of NO from fuel bound nitrogen.

2.3.4 Sulfur Oxides

Sulfur oxides (SOx) refers to several sulfur containing species which can be emitted during combustion, predominately in the form of SO_2, SO_3, and H_2SO_4 [20]. SOx emissions are a result of the release of the sulfur contained in fuels, which is often bound in the fuel in the same chemical structure (i.e. SO_2, SO_3, and H_2SO_4). In heavy fuel oils and coal, sulfur contents can be very high; as much as 7% by weight. For biomass and biomass derived fuels, SOx emissions are typically very low because these fuels are very low in sulfur content [23].

2.3.5 Particulate Matter

Particulate matter (PM) refers to any nongaseous emissions from combustion, including ash, soot, polycyclic aromatic hydrocarbons, and unburned fuel residues [21] [24]. Particulate matter is categorized as $PM_{2.5}$ and PM_{10} corresponding to particulate below 2.5 and 10 micron respectively [25]. The $PM_{2.5}$ category particulate is regulated more strictly than PM_{10} because they are capable of penetrating more deeply into the lungs.

2.3.5.1 Ash

Ash is a result of inorganic fuel materials which exit the exhaust in the condensed phase [11]. Aside from emissions as a pollutant, often these inorganic species will condense on equipment surfaces (i.e. boiler tubes, turbine blades) leading to wear and reduced performance.

2.3.5.2 Soot and Polycyclic Aromatic Hydrocarbons

Soot is a carbonaceous solid material consisting of very large, complex aromatic polymer structures produced from gas-phase condensation reactions of fuel species at high temperatures [21]. Soot radiates as a blackbody strongly in flames, giving flames their often characteristic yellow color.

In premixed flames of alkane, alkene, or alkyne fuels, soot is not formed until conditions become fuel rich [21]. However, aromatic fuels have a higher sooting tendency, producing soot at lean conditions with equivalence ratios as low as 0.87, where equivalence ratio is defined in Equation 2.2 [26].

$$\Phi = \frac{\left({m_{air}}/{m_{fuel}} \right)_{Stoichimetric}}{\left({m_{air}}/{m_{fuel}} \right)_{Actual}} \tag{2.2}$$

This fuel dependent sooting tendency suggests that soot formation is a kinetically controlled process. In diffusion flames, soot is formed in regions high in fuel vapor concentration that are at elevated temperatures and beyond the sooting limit. Therefore, in spray flames operating under globally lean conditions (below $\phi = 0.87$), soot is formed as a result of mass transfer limitations between fuel and oxidizer, in addition to fuel-dependent kinetic phenomena.

Although the kinetics and reaction pathways of soot formation are very complex, soot production in flames can be characterized by three overlapping phenomena: 1) particle inception, 2) coagulation and agglomeration, and 3) surface growth [21]. Particle inception occurs through a series of polymerization reactions in the gas phase leading to condensed-phase polycyclic structures on the order of 1.5 to 2 nm. After inception, Brownian motion leads to collisions between the particles, allowing them to coagulate into larger particles or agglomerate into large groups of smaller particles. Continued growth of the soot particles then follows due to heterogeneous reactions of gas phase fuel hydrocarbons to create additional polycyclic structures. The final soot structure consists of particles in the range of 10 to 40 nm. Although these particles can exist singly, they are commonly found to exist as large agglomerates containing up to hundreds of primary particles in branch-like structures.

The soot that is emitted in the exhaust of a flame is much less than the peak soot concentrations within a flame, indicating a strong mechanism of soot oxidation [21]. Oxidation of soot can be achieved directly by O_2; however, the hydroxyl radical (OH) has been shown to be much more dominant as a soot oxidizing agent. If soot is quenched or the local OH concentration is low, soot oxidation will not go to completion and soot will exit the combustion environment.

Polycyclic aromatic hydrocarbons (PAH) share many similar characteristics to soot [21]. Like soot, PAH is formed through polymerization reactions of fuel vapors to generate larger aromatic molecules. However, these structures do not continue to grow. If PAH fails to oxidize in the flame, it can leave the combustor as a vapor; however, it is most often adsorbed into soot particles, where it retains a chemical identity that is distinct from soot.

Soot and PAH production can be reduced by achieving stronger fuel-oxidizer mixing in fuel-lean nonpremixed flames. Simple additives to diffusion flames including, CO_2, H_2, H_2O, N_2, and He have all been found to be equally effective in reducing sooting tendencies when judging them in terms of their heat capacities. This suggests that the effect of these additives of soot production is that of reducing the existence of high temperature fuel rich regions in the flame, rather than by affecting chemical reaction pathways.

2.3.5.3 Stack Solids

For medium and heavy fuel oils, solid carbonaceous fuel residues (stack solids) can remain after lighter components in the fuel have been burned [11, 24]. These coke-like residues are generally in the shape of hard, hollow spheres, called cenospheres, and are formed by thermal decomposition of heavier components in the fuel, although the exact reaction pathways of this process are not well understood. As a droplet of heavy fuel oil is burned, the volatile components are first vaporized and ignited, followed by a swelling and frothing, until a hard cenosphere is formed and burned. Cenospheres can be larger than the original droplet size, with burning rates that are as little as 10% of the burning rate during the volatile combustion phase.

Aside from being a potential pollution problem, these unburned fuel residues can be a significant source of combustion inefficiencies, with cenospheres containing as much as 10% of the mass of the original fuel droplet [11]. Further, these residues can build up on equipment surfaces leading to wear and reduced performace.

Fuel oils which are high in asphaltene content and high in viscosity tend to have the highest tendency to form cenospheres [11]. However, this is best characterized by Conradson carbon number test, which measures the amount of fuel residue remaining after pyrolysis of a fuel under controlled conditions [24]. The quantity of fuel residue which leaves the combustor as stack solids can be greatly reduced by improving fuel atomization. Vanadium present in heavy fuel oils has been shown to help catalyze these solid residues to burn more rapidly; however, this metal is very corrosive at high temperatures, making this an unlikely prospect for use in turbine applications.

2.4 Pyrolysis Oil Combustion

Much of the research in pyrolysis oil combustion thus far has focused either on practical applications or fundamental studies of single droplet combustion. There has been almost no research performed which has utilized flame visualization techniques and investigated the causes of exhaust emissions in realistic spray flames. The utilization of pyrolysis oil in heat and power production systems has been reviewed in recent publications by Chiaramonti et. al [4] and Czernik et. al [5], who provide comprehensive discussions of findings in pyrolysis oil combustion .

2.4.1 Pyrolysis Oil Fuel Properties

Biomass-derived fast pyrolysis oils are produced through a rapid thermal decomposition of organic material [1-3]. Small biomass particles (< 5 mm) are volatized in an oxygen depleted environment at temperatures in the range of 400 to 500 °C and the vapors condensed in a very short time period (< 2 s) to prevent further decomposition to simpler molecules. Up to 70% of the biomass can be recovered as fast pyrolysis liquids. The rest of the biomass is either converted to simple gases (CO_2, CO, H_2) or remains unvoltalized and is collected as carbonaceous solids (char).

Pyrolysis oil properties can vary widely depending upon the biomass feedstock used and process conditions employed during the conversion process. Typical pyrolysis oil properties are listed below compared to light and heavy fuel oils as compiled by Chiaramonti et al.[4].

Table 2.1 Typical pyrolysis oil, light fuel oil, and heavy fuel oil properties [4].

	Pyrolysis Oil	Light Fuel Oil (#2)	Heavy Fuel Oil (#6)
Carbon [wt-%]	32–48	86	85.6
Hydrogen [wt-%]	7–8.5	13.6	10.3
Nitrogen [wt-%]	0.4	0.2	0.6
Oxygen [wt-%]	44–60	0	0.6
Water [wt-%]	20–30	0.025	0.1
Solids [wt-%]	<0.5	0	0.2–1.0
Ash [wt-%]	<0.2	0.01b	0.03
Viscosity [cSt]	15–35 (@ 40 °C)	3.0–7.5 (@ 40 °C)	351 (@ 50 °C)
Density [kg/L]	1.10–1.30	0.89	0.94–0.96
LHV [MJ/kg]	13–18	40.3	40.7
pH	2-3	Neutral	n.a.

The fuel properties of pyrolysis oil vary substantially from those of typical hydrocarbon fuels. Pyrolysis oils have high oxygen and water content compared to petroleum derived fuels. This results in a low energy content of the fuel, with a lower heating value (LHV) less than half that of fuel oils.

Pyrolysis oil also typically tends to have viscosities which are somewhat higher than light fuel oil, but which are typically much lower than heavy fuel oil. This characteristic, along with the increased solids content, has led some researchers to develop custom nozzles for achieving pyrolysis oil sprays [27-29].

The high acidity of pyrolysis oil also poses a challenge for its utilization in equipment designed for petroleum fuels. Mild steels and aluminum are not sufficient to resist corrosion from pyrolysis oil and therefore stainless steels, or polymers such as polyethylene and polypropylene must be used in their place [30, 31].

Oasmaa et- al. has been very prolific in discussing pyrolysis oil properties, characterization methods, and standards [6, 30-33]. Oasmaa et- al. cites the properties of homogeneity, water content, solids content, stability, and flash point as the most critical parameters for standardization to implement pyrolysis oil into existing applications [6, 33]. With regard to water content she has noted that increased water content can reduce oil viscosity; however, it negatively impacts the heating value, ignition rates, and stability of the oil. The high solids content has proven to be a challenge as Oasmaa and other researchers have noted that it is very difficult to filter pyrolysis oils [34-36]. The instability of pyrolysis oils, shown by their tendency to increase in viscosity over time and separate, also presents several challenges for use as a fuel [6, 30-33, 37-39]. Volatilization of these oils results in the significant quantities of carbonaceous solid residues [33, 37]. The ignition rates of pyrolysis oils can vary greatly between various pyrolysis oils, especially as a function of water content. Moreover, ignition rates are difficult to quantify for pyrolysis oils with high flash points (> 100 °C) because the water will evaporate from the sample before ignition can occur during flash point measurements [6].

2.4.2 Use in Internal Combustion Engines

Several researchers have investigated the use of pyrolysis oil in internal combustion (diesel) engines [40-45]. All of the research reviewed reports challenges in injection systems due to high solids content and/or the acidic nature of the oil. Such challenges required equipment modifications for filtration systems, injection designs, and/or dual fuel delivery to achieve stable engine performance.

Shihadeh and Hochgreb have found pyrolysis oil to have longer ignition delays, reduced pressure cylinder pressures, and delayed heat release profiles compared to diesel fuel combustion [42]. They attribute the delayed heat release behavior to pyrolysis oil having slower reaction kinetics than fuel oil. Further research by Shihadeh and Hochgreb investigated two different oils produced from different methods, both in their original state, and with the addition of water to provide the same water content in the two oil samples [43]. They found that ignition performance was best for oils which had lower water content and a greater degree of thermal decomposition (as quantified by the average molecular weight of the oil).

2.4.3 Use in Gas Turbine Engines

Pyrolysis oil has been investigated for use in gas turbine systems by several researchers [46-51]. All of these investigators employed fuel preheating to reduce the viscosity of the oil for improved spray behavior. Additionally, all researchers used a fossil fuel for start up before switching to pyrolysis oil, to preheat the combustion environment for enhanced fuel ignition.

Andrews et al. performed some of the earliest work with pyrolysis oil utilization in gas turbines, by carrying out studies in an Orenda GT2500, 2500 kWe turbine [46, 49, 50]. In addition to fuel preheating and a separate start up fuel, a prototype dual-fuel nozzle was developed along with a hot section cleaning system. The authors reported alkalai erosion of turbine blades and tar deposits on the combustion liner, nozzle, and air swirler that could be removed by utilizing another fuel during shut-down.

Strenzoik et al. performed pyrolysis oil combustion studies in a 75 kWe Deutz T216 gas turbine [48]. The researchers were unable to operate the turbine on pure pyrolysis oil and instead utilized a dual-fuel pressure nozzle with diesel fuel. Once again, deposits were found on the combustion chamber and turbine blades; however, these deposits had to be removed by mechanical action. Carbon monoxide (CO) and unburned hydrocarbon (HC) emissions were found to be significantly higher than that of diesel fuel; however, nitrogen oxides (NOx) emissions were found to be slighter lower. These differences were considered to be attributed to low quality combustion of the pyrolysis oil.

2.4.4 Use in Industrial Boilers

Several researchers have investigated the use of pyrolysis oil for the operation of medium- to large-scale industrial boilers (> 200 kW) [27-29, 34-36, 52-56] [57]. Similar to the work carried out with turbines, most of this research has been demonstrative and developmental with many similarities between these various studies.

Throughout these studies, several atomization techniques have been employed, including pressure atomization, [34, 35] [52, 54], air atomization [27, 29, 36, 55, 58, 59], steam atomization [29, 36, 55]. Throughout all of the studies, fuel preheating was utilized to reduce viscosity. Gust et- al. were able to achieve successful combustion using standard pressure nozzles with increased pressure and fuel temperature; however, the droplet sizes were still not as small as that for No. 2 light fuel oil (LFO) [34, 35]. Several authors achieved successful combustion with air atomizers; however, Shihedah et al found steam atomization to be preferred to air atomization as it reduced coking levels in the nozzle [36].

However, with steam atomization, Van De Kamp et al. noted that the steam flow must be kept high or else nozzle coking would occur [29, 55]. A few authors utilized custom nozzles which tended to yield beneficial results compared to commercially available nozzles [27-29]. Preto et al. noted that when a commercially available nozzle designed for No. 6 heavy fuel oil (HFO) was used, significant amounts of deposits collected in the bottom of the combustor, whereas, a custom steam atomization nozzle designed for coal-water slurry mixtures was very effective at achieving clean combustion [28]. Although most authors showed the capability of achieving satisfactory atomization and combustion, several reported challenges with nozzle clogging and coking [28, 29, 34-36, 52, 53, 55].

Aside from nozzle considerations, all the researchers discussed here utilized a startup fuel to preheat the combustion chamber before switching to pyrolysis oil [27-29, 34-36, 52-56]. Although this greatly improved the ignition of the oil, some investigators found that additional measures were necessary to achieve stable combustion. Oasmaa et al. and Gust et-al. added an additional radiative section at the beginning of the flame to increase radiative heating to the spray and flame improving fuel ignition [34, 35, 53]. Kyto et al. increased the strength of the air swirl to improve the flame retention, leading to a shorter, more intense flame [52].

With regard to pollutant emissions, most researchers compared pyrolysis oil to either No.2 light fuel oil (LFO) or No. 6 heavy fuel oil (HFO). Carbon monoxide (CO) emissions were typically found to be only slightly higher in pyrolysis oil than LFO [27, 29, 36, 55, 58]; however, Oasmaa et al. and Wickboldt et. al found them to be significantly greater [53, 57] while Gust. et- al. found CO emissions to be very similar to LFO [34, 35].

Nitrogen Oxide (NOx) emissions from pyrolysis oil were found to be only slightly higher than those from LFO [27, 34-36, 53, 58]. With respect to HFO Oasmaa et al. found NOx emissions from pyrolysis to be lower [53], while Van De Kamp et- al. had significantly higher NOx emissions [29, 55]. In the work by Van De Kamp et al. the high NOx levels were attributed partially to the fuel bound nitrogen in pyrolysis oil; however, the authors were able to reduce the NOx by 30-50% by utilizing staged combustion [29, 55].

Particulate matter (PM) emissions from pyrolysis oil were always found to be higher than those for LFO, with most researchers reporting significantly higher levels [27, 34-36, 52-54, 58]. In comparison to HFO, Rossi et. al had lower PM levels [54], while Van De Kamp et al. and Oasmaa et- al. had higher values [29, 53, 55]. Between CO, NOx, and PM emissions, particulate matter has arisen as one of the most challenging aspects of pyrolysis oil combustion given its consistently high readings. Beyond the particulate emissions which are measured in the exhaust of the combustor, particulates have been observed to collect on burner surfaces [28, 53].

Huffman et al. and Rossi et al. were the only researchers to report sulfur oxide (SOx) emissions [27, 54, 58]. Both reported very low SOx emissions, as expected for a biomass derived fuel.

2.4.5 Use in Domestic-Scale Heating Applications

To date there have only been two sets of researchers who have investigated pyrolysis oil combustion in flow ranges below 30 kW. Stamatov et al. burned slow-pyrolysis oil in varying mixtures with ethanol for comparison with No. 2 light fuel oil (LFO), with special attention given to NOx emissions in a laboratory developed swirl-stabilized combustor [60, 61]. They found that 100% and 80% pyrolysis oil mixtures burned to give NOx emissions which were higher than that predicted by theoretical calculations of thermal NOx. However, it was also found that too high of an increase in ethanol concentration leads to a reduction of heat flux from the flame. As such, the authors report that an optimal mixture of pyrolysis oil and a polar solvent (ethanol) exists which can reduce NOx, while maximizing flame heat flux and improving spray behavior. The authors did not report any findings with regard to particulate emissions.

Bandi et al. modified a WS FLOX burner for combustion of pyrolysis oil and coupled it to a SOLO^{TM} stirling engine [62]. The FLOX (flameless oxidation) combustion process uses very strong exhaust gas recirculation and combustion air preheating to produce a more uniform combustion environment. This reduces thermal NOx production as well as providing a long flame residence time. An air-atomization nozzle was utilized and a mechanical nozzle cleaning system was installed to clean the nozzle upon blockage. The authors reported very clean combustion with zero soot emission and no fuel residues remaining in the combustor. Further, CO and NOx levels were low, yet the authors noted that the NOx levels may be attributed to fuel bound nitrogen.

2.4.6 Single-Droplet Combustion Studies

Several researchers have carried out studies of the combustion behavior of single droplets of pyrolysis oil [63-67]. Wornat et al. performed the pioneering investigation in this field by observing the combustion of 320 micron diameter droplets falling through a drop furnace reactor at 1600 K [67]. Wornat et al. found pyrolysis oil to burn with a distinctive behavior including four stages of combustion:

1) initiation of a blue flame which ends abruptly once the light volatiles in the droplet are consumed
2) distortion and swelling of the droplet, followed by a microexplosion caused by a rapid expansion and production of vapors within the droplet
3) coalescence of droplet fragments into larger particles
4) final combustion of the remaining particle which occurs with a sooty, yellow flame

Wornat et- al. notes that the microexplosion event observed in the pyrolysis oil is due to the highly multicomponent nature of the fuel, with components of widely varying boiling points [67]. Despite the complex, multi-stage nature of the pyrolysis oil combustion event, Wornat et al. found that the burnout time for pyrolysis oil is comparable to that of No. 2 light fuel oil (LFO). As the oxygen content in the combustion environment was increased, the burnout time of the pyrolysis oil decreased; however, the timing of the events in the four stages of combustion remained unchanged.

For some studies the burnout time was long enough that the final stage of combustion was not able to go to completion and unburned fuel particles exited the reactor [67]. These particles were collected and studied in an electron scanning microscope (SEM). Wornat found two types of morphologies in the particles; 1) dense, glassy spheres and 2) hollow, fragile spheres. Wornat refers to the later of these as cenospheres; however, she notes that these particles do not look like the cokes that are produced in the combustion of heavy fuel oils. This observation led her to suggest that these cenospheres are formed from polymerization reactions of heavy components in the oil. Elemental analysis of the cenospheres revealed that they do not contain any inorganic materials present in the original oil. The cenospheres were observed to be nearly as large as the original fuel droplet.

Shaddix et al. carried out further droplet studies in the same reactor used by Wornat et- al.--the biomass fuels combustion system (BFCS) at Sandia National Laboratory [65, 66]. In the first of the two studies carried out by Shaddix et al. three different pyrolysis oils were evaluated, which varied according to the degree to which they were thermally cracked during the pyrolysis oil production process [65]. For all three pyrolysis oil samples, the same combustion stages and large cenospheres were observed as those seen by Wornat et al.; however, the timing of the events, and size of the cenospheres formed during combustion varied slightly between each sample. The oils which had higher water content and lower dry oxygen content (oxygen not bound in water) tended to have more delayed and effective microexplosion events, with slightly smaller cenospheres formed at the end of the combustion event. Because the oils with higher water content also had lower oxygen content, it was difficult for the authors to discern the cause of the microexplosions and cenospheres. The authors note that it seems likely that the higher water content would delay the microexplosion and make it more effective at dispersing the fuel particle. However, the authors also note that it seems likely that with a reduced oxygen content in the oil, the degree of polymerization leading to cenosphere formation would be reduced, also aiding in the microexplosion event.

In further work carried out by Shaddix et al. mixtures of pyrolysis oil with 5% and 10% water added were tested to better understand the effects of water on the combustion event [66]. With the 5% water batch, there was no significant change in the combustion event; however, for the 10% water batch the microexplosion was more delayed and more violent with less post-explosion fragmentation of the remaining particles. Additional tests carried out with char and/or methanol added to the oil yielded a more rapid onset of microexplosion; however, it was less effective at dispersing the particle into smaller fragments.

D'Alessio et al performed droplet experiments of pure pyrolysis oil and pyrolysis oil/LFO emulsions [64]. Studies were carried out in a drop furnace similar to that used by Wornat et al. and Shaddix et al.; however, the researchers were able to achieve smaller droplets (50-100 μm) by mixing the pyrolysis oil with acetone and then generating droplets of the mixture. The acetone is immiscible with the oil and it evaporates very rapidly such that by the time the droplet enters the combustion environment it is composed only of pyrolysis oil. The diameter of the pyrolysis oil droplet was measured to assure that it did not change in size during the evaporation of the acetone. Once again, D'Alessio et al. observed the same characteristics of pyrolysis oil droplet combustion [64]. Further, cenospheres were collected and analyzed via SEM imaging and the same characteristic morphology was observed, as well as a lack of inorganic content (i.e. ash) in the particles. However, the size of the final droplet before burnout (i.e. cenosphere) was observed to be relatively larger than the original droplet diameter in comparison to the findings of Wornat et- al., with diameters nearly twice as large as the original droplet diameter.

2.4.7 Pyrolysis Oil Spray Studies

The amount of research in pyrolysis oil spray characteristics is limited to only a few researchers [57, 68, 69]. Wickboldt et al. state that they measured velocity and particle size from a pyrolysis oil spray using laser Doppler velocimetry (LDV); however, they do not report any of their results [57]. Attempts at locating additional work from Wickboldt et- al. in which these values are reported has been unsuccessful.

Garcia-Perez et al. studied pyrolysis oil sprays from Delavan pressure atomization nozzles in the range of 1 to 2 gal/hr, measuring flowrates and droplet sizes from the nozzle as a function of fuel pressure and temperature [68]. Droplet sizes were measured using Malvern Master-sizer equipment and a Sauter mean diameter (SMD) calculated. Garcia-Perez et al. found that at 80 °C fuel preheat temperature the pyrolysis oil behaves as a Newtonian fluid with regard to its flowrate versus pressure relationship through the nozzle. The authors were able to achieve SMD values lower than 50 μm; however, some droplets were as large as 150 μm. The diameter distribution range was slightly greater for pyrolysis oil sprays than for water or fuel oil sprays.

Wiemer et al. utilized particle image velocimetry (PIV), laser Doppler anemometry (LDA), and phase Doppler particle analysis(PDPA), to examine sprays of water/glycol mixtures as a surrogate liquid with similar fluid properties to those of pyrolysis oil. [69]. The authors found that the SMD of the droplets decreased as the air-to-liquid ratio through the air atomization nozzle was increased. The authors did not report any results from the PIV analysis. The results in this publication are very limited and attempts at locating additional work from Wiemer et- al. for these studies has been unsuccessful.

CHAPTER 3. EQUIPMENT AND METHODS

The core objective of the research is to characterize pyrolysis oil combustion in a swirl-stabilized flame at small-scale heating loads. The combustion apparatus developed in this research is based on a Beckett AF domestic-scale LFO burner. Several design modifications have been made to achieve stable pyrolysis oil combustion and to develop a system with improved control and instrumentation of the various operating parameters. Further, the apparatus has been designed to allow for optical access for flame visualization studies.

The physical and chemical properties of the fuels used in this study have been well characterized. This information has been used to establish a test matrix which allows for meaningful comparisons between the different fuels.

During the combustion studies, exhaust emissions have been measured to quantify combustion performance. These measurements include CO, HC, NOx, and PM.

Additionally several optical techniques have been performed to characterize combustion and spray behavior. These techniques allow for visualization of fuel, soot, and other species present during the combustion event, which allow for a more complete understanding of the flame phenomena.

Samples of exhaust particulates have also been analyzed using SEM to characterize morphology and elemental composition.

3.1 Combustion Apparatus

The combustion apparatus developed during this research is based on a standard home-heating oil furnace. A custom burner housing based on the original burner design has been constructed to allow for improved instrumentation and control as shown in Figure 3.1. Several modifications to the burner have been made to improve flame stabilization and burner control systems, including fuel preheating, air preheating, nozzle type, swirl strength, fuel delivery systems, and air delivery systems. The result is a burner that serves as a well characterized combustion apparatus for studying fuels and operating conditions in a swirl-stabilized spray flame.

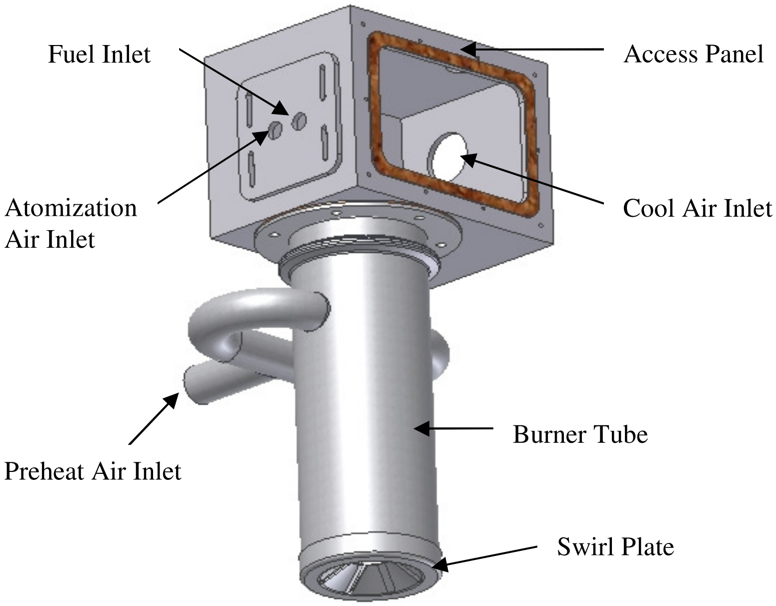

Figure 3.1 Combustor housing.

The flame is fired vertically, rather than horizontally, to aid in the use of laser diagnostic techniques and downward firing is used instead of upward firing to prevent unburned fuel from collecting on the burner head during unstable combustion events. The internal dimensions of the chamber are 9 x 9 x 30 inches, with refractory bricks lining the inside of the chamber. The bricks are surrounded by Inswool ceramic blanket insulation which is then covered by aluminum frames which serve as window mounts as shown in Figure 3.2. One side of the burner has narrow slit windows which allow for the passage of a laser sheet into the chamber, while the adjacent side of the burner has full view windows for visualizing the full flame zone. The window mounts are designed with a slot for a refractory shield to be slid in front of the windows to keep them clean during sooty combustion conditions. The windows are fused silica which allows for optical transmission into the deep UV. Optical access to the nozzle exit and flame stabilization location is partially restricted because of the placement of the nozzle within the burner tube.

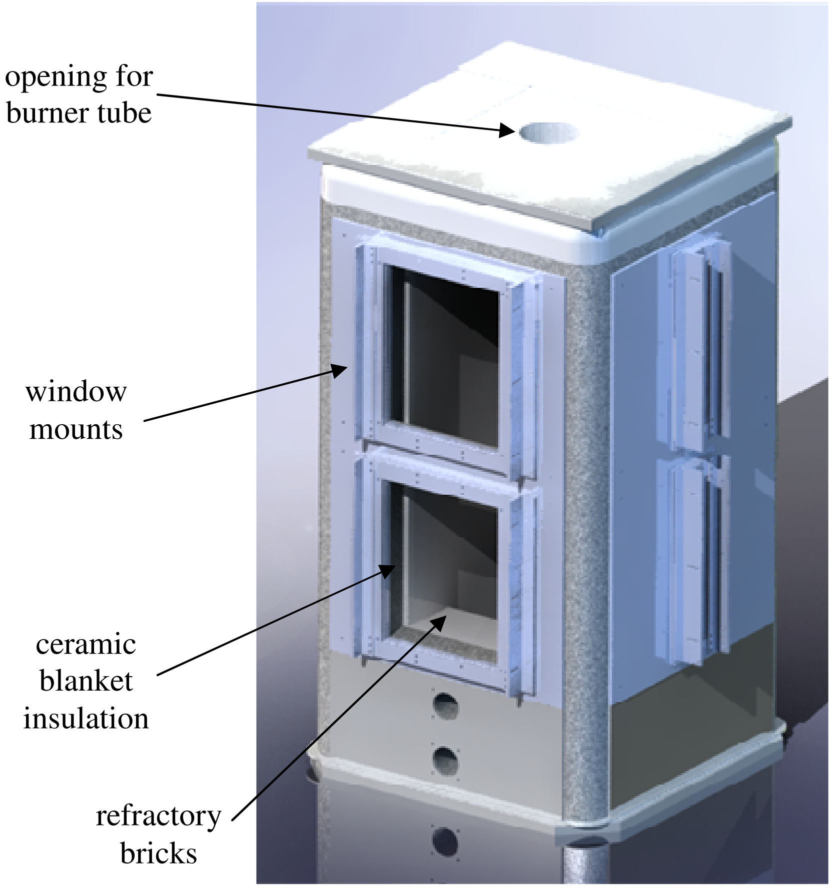

Figure 3.2 Combustion chamber.

The entire combustion apparatus system is shown in Figure 3.3.

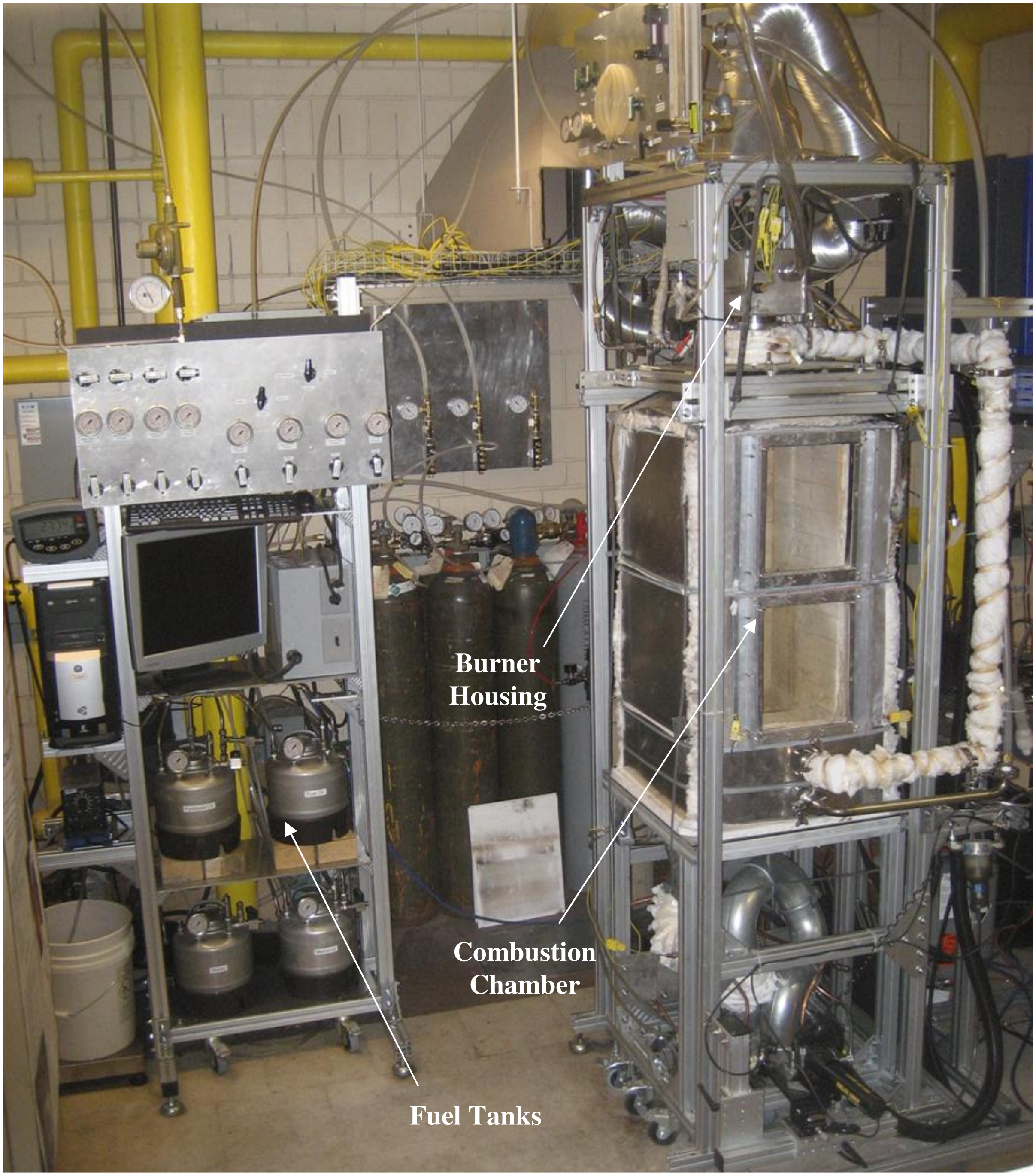

Figure 3.3 Combustion apparatus.

3.1.1 Flame Stabilization

To understand the combustion properties of the fuels to be studied, it is important to have a well-stabilized flame. Initial attempts at burning pyrolysis oil in the standard Beckett AF burner with pressure atomization nozzles failed due to an inability to maintain stable ignition of the fuel. With improvements in fuel heating and re-radiation to the flame, ignition of pyrolysis oil could be maintained; however, the flame was poorly stabilized as shown in Figure 3.4 (b).

(a) **(b)**

Figure 3.4 Photographs of a (a) stabilized fuel oil flame and (b) unstabilized pyrolysis oil flame in a Beckett AF burner with minor modifications.

To improve the flame stabilization a heat exchanger was designed and installed in the bottom of the combustion chamber as shown in Figure 3.5. This heat exchanger allowed for combustion air temperatures up to 400 °C.

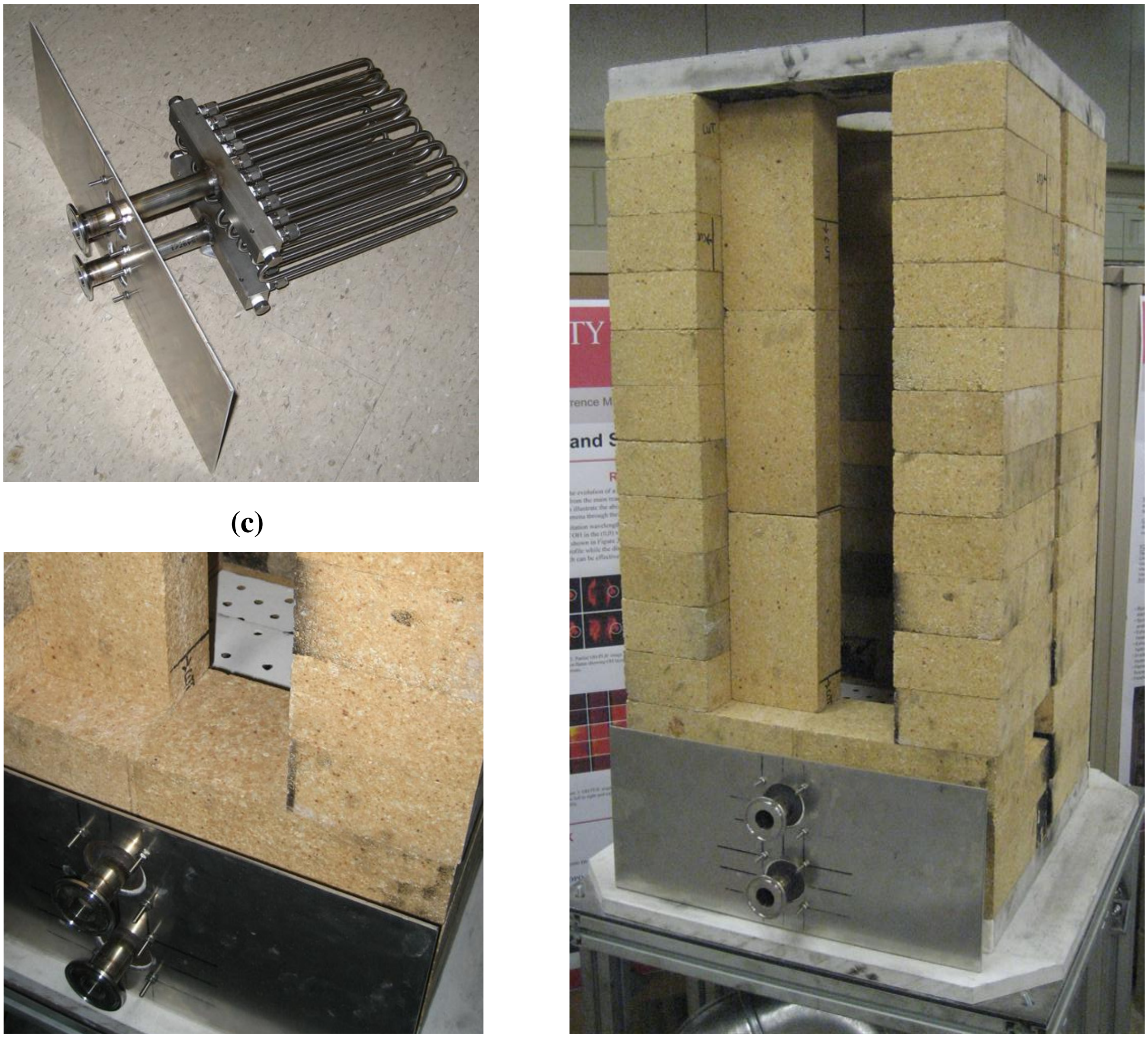

(a) (b) (c)

Figure 3.5 Images of the air heater (a) with its installation in the chamber (b) and the refractory plate installed to insulate it from the combustion zone (c).

In addition to preheating the air used for combustion, the air swirler has been modified to increase the strength of recirculation in the flame. A standard F3 air swirl used in the Beckett AF burner is shown in Figure 3.6. As can be seen, the swirl vanes are not very large, and as such the swirl strength is limited. For combustion of fuel oil, this degree of swirl is sufficient to achieve a clean burning, stable flame. However, for pyrolysis oil, the swirl strength has been shown to be too weak.

Figure 3.6 Standard F3 air swirler used in the Beckett AF burner.

A standard F3 swirler has been modified to provide a greater degree of swirl. The modified swirler, shown in Figure 3.7, has significantly larger swirl vanes, which serve to greatly increase the swirl of the air flow.

Figure 3.7 Modified air swirler.

The combination of combustion air preheat and modified swirl design has a coupled effect on improving the flame stabilization. By preheating the air, not only is the ignition of the fuel improved due to the higher air temperatures, but the swirl is also increased because of the lower density of the hot air. The lower density air moves through the swirl vanes with a higher momentum, thus generating a stronger recirculation zone.

The distance between the nozzle exit and the swirl plate can also have a significant effect on flame stabilization. The burner housing has been designed to allow for the nozzle position to be moved upwards or downwards as shown in Figure 3.8. By moving the nozzle further back from the air swirler, the fuel has more time to vaporize before reaching the flame stabilization point.

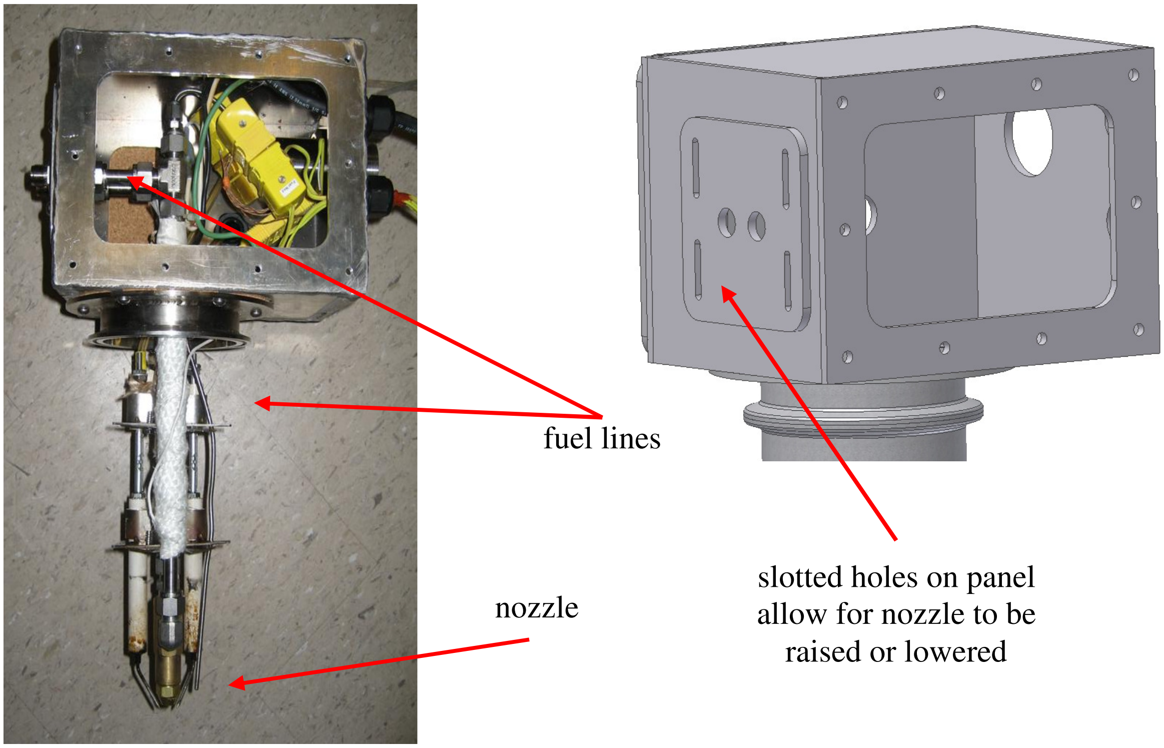

Figure 3.8 Burner housing.

With these modifications, a stable pyrolysis oil flame could be achieved. However, as will be discussed, the flame stabilization with air atomization nozzles was much improved over that of pressure atomization nozzles.

3.1.2 Fuel Delivery and Control

Both pressure atomization and air atomization nozzles have been employed in this research. As such, two different systems are required for fuel delivery and control. For both systems, pyrolysis oil was preheated and filtered prior to reaching the nozzle. Further, fuel oil was delivered to the nozzle during start up to heat the combustion chamber prior to switching to pyrolysis oil. Water and methanol were also used during start up to aid in the pyrolysis oil preheating process and during shut down to flush the oil from fuel lines and filters.

3.1.2.1 Pressure Atomization Fuel Delivery and Control

The process flow diagram for the fuel delivery and control system when using pressure atomization nozzles is shown in Figure 3.9. For delivery of all fuel oil, pyrolysis oil, methanol, and water, pressure tanks with dip tubes have been utilized. Nitrogen delivered from a compressed gas cylinder is used to pressurize the tanks to the desired level. The pressure nozzles used in this work are designed to provide their designated flowrate when fuel oil is delivered to them at 100 psig; however, the flowrate and atomization quality can be adjusted by increasing or decreasing the delivery pressure. To allow for independent control of the fuel oil and pyrolysis oil spray properties, separate nitrogen bottles were used to pressurize these tanks.

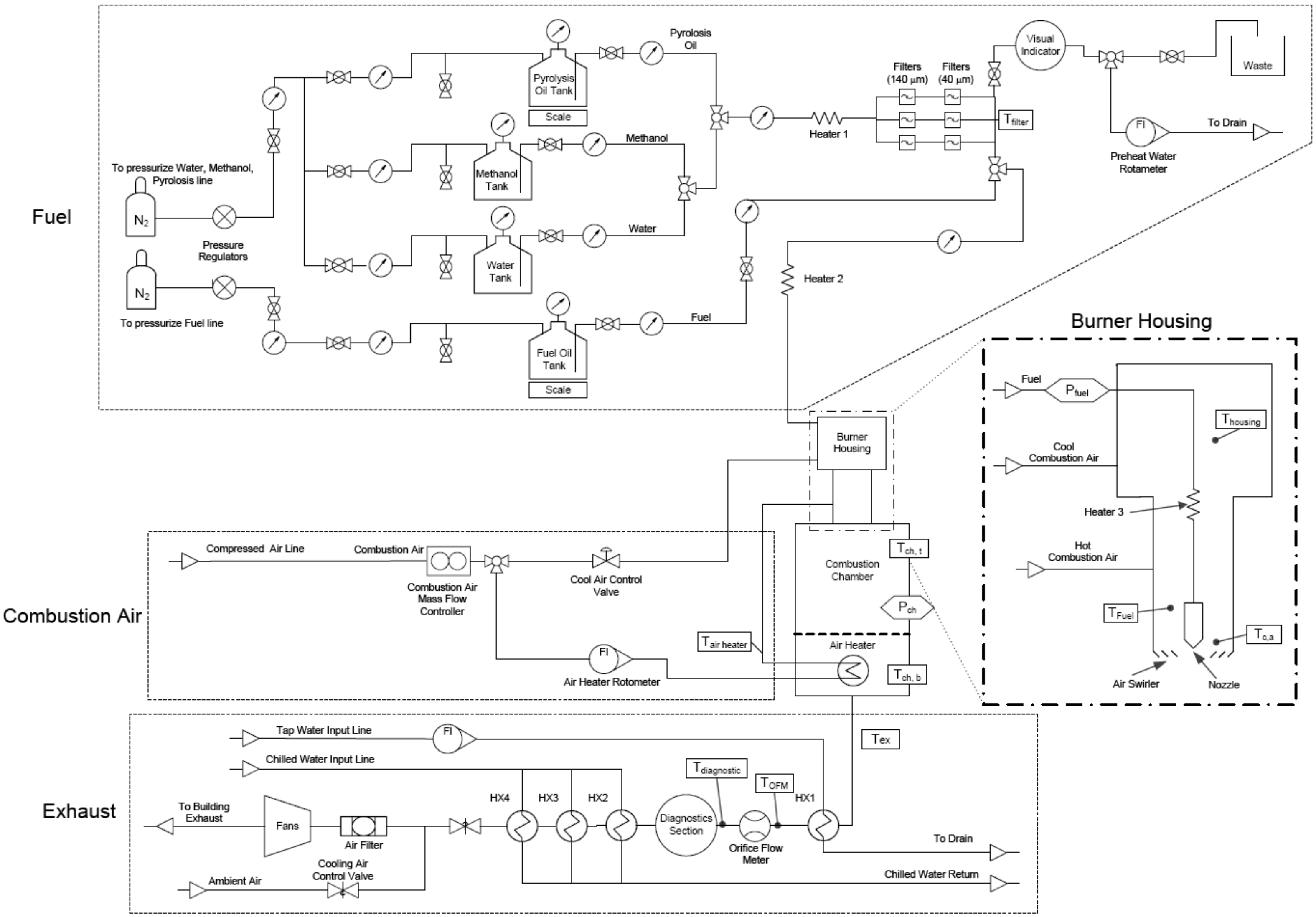

Figure 3.9 Process flow diagram of combustion apparatus for pressure atomization.

The flowrate of the fuel was measured by measuring the mass of fuel consumed. This was achieved by placing the fuel tank (either fuel oil or pyrolysis oil) on a scale. Weight measurements are recorded every 3 seconds by the data acquisition system, and measurements taken 90 seconds apart were used to calculate an average flowrate over that time period. Thus, every 3 seconds the flowrate was updated; however, this reading was based on the previous 90 seconds of flow.

To further improve the accuracy of the fuel flowrate measurement, a moving time average was performed on the fuel flowrate measurements. The previous 90 seconds worth of calculated fuel flowrate values (30 values) were averaged together to provide a moving average. This averaging resulted in a measurement of fuel flowrate to within 0.01 gph. However, this method averaged a total of 180 seconds worth of measurements such that there was a significant time delay. As such, tests were carried out under steady-state operation.

To aid in the atomization of pyrolysis oil, the fuel was preheated to reduce its viscosity. Heating of the oil was performed in the lines while travelling to the nozzle, rather than by heating the oil batch in the fuel tank. Because rapid aging of pyrolysis oil can occur if the oils are held at elevated temperatures (~80 °C) [70], in-line heating of the oil was used to limit fuel aging and to provide better conservation of the limited fuel supplies.

Two sets of heaters were used, each controlled with its own temperature controller. The first heater employs heat tape wrapped around the fuel lines leading up to the filters and the filters themselves. The temperature at the end of the filters was controlled to be 65 °C, to reduce the viscosity for filtration. The second heater employed heat tape wrapped around the fuel line leading to the burner housing and along the fuel line leading to the nozzle. This temperature was measured and controlled approximately 3 inches upstream of the nozzle exit. Typically fuel oil was not intentionally preheated prior to reaching the nozzle; however, its temperature could be elevated and controlled by utilizing the second set of heaters.

The pressure nozzles used in this research were Delavan type A nozzles with a 70-degree spray angle. The nozzles were equipped with a 60 micron sintered filter at the inlet of the nozzle to achieve fine filtration before passing through the nozzle opening. Before reaching the nozzle, the pyrolysis oil was passed through three 140 micron filters in parallel followed by three more 40 micron filters in parallel. This level of filtration was sufficient to prevent nozzle clogging ; however, the 40 micron filters would clog in a very short time (~3 hours). Fuel oil passing to the nozzle passed through a single 40 micron filter before reaching the nozzle and this level of filtration has been found to be sufficient and robust.

The main control for fuel flowrate and spray behavior was the pressure at which the fuel is delivered to the nozzle. This pressure was measured to within ± 0.75 psig and controlled by adjusting the pressure regulator at the compressed nitrogen bottle.

To switch from fuel oil to pyrolysis oil and maintain flame stabilization, it was necessary to ensure that the pyrolysis oil is at a high enough temperature that it could be filtered and sprayed effectively. Therefore, the heaters needed to reach a steady state condition with a fluid flowing through them before switching to pyrolysis oil. This was done by flowing water through the first heater section and then bypassing that flow to a rotameter which was used to control the water flowrate. With the flowrate set to the desired level and the heater on, the temperature controller was able to operate effectively to maintain a steady temperature for the given flow conditions. With fuel oil being delivered through the second heater and nozzle to provide combustion for heating the chamber, the second fuel heater and temperature controller could be turned on to stabilize to the desired operating temperature.

Once the fuel preheat temperatures at the filters and at the nozzles are stabilized to the desired temperatures, the switch to pyrolysis oil could be made. This was first done by switching from water flow through the filters to methanol. This was then followed by a switch to pyrolysis oil. The brief period of methanol flow allows for a smooth transition from water to pyrolysis oil. If pyrolysis oil follows water flow directly, phase separation of the pyrolysis oil would occur in the fuel lines (hence water insoluble fraction), leading to blockage of the fuel filters. The visual indicator section in the fuel line allowed for an observation of the switch from methanol to pyrolysis oil in the fuel lines. Once this observation had been made in the visual indicator section, then the filters were filled with pyrolysis oil and the final switch to pyrolysis oil could be made. This was done by stopping flow to the water rotameter and switching the final valve from fuel oil to pyrolysis oil, allowing for flow to the nozzle.

3.1.2.2 Air Atomization Fuel Delivery and Control

The process flow diagram for the fuel delivery and control system when using air atomization nozzles is shown in Figure 3.10. The air atomization nozzles used in this research are type SNA siphon style air atomization nozzles made by Delavan. These nozzles are very sensitive to changes in pressure such that a 1 -inH2O change in pressure can lead to roughly a 0.01 gph change in flowrate. Given this high sensitivity to pressure, it is not possible to achieve accurate control of fuel flowrate by controlling the fuel delivery pressure as was done for the pressure nozzles.

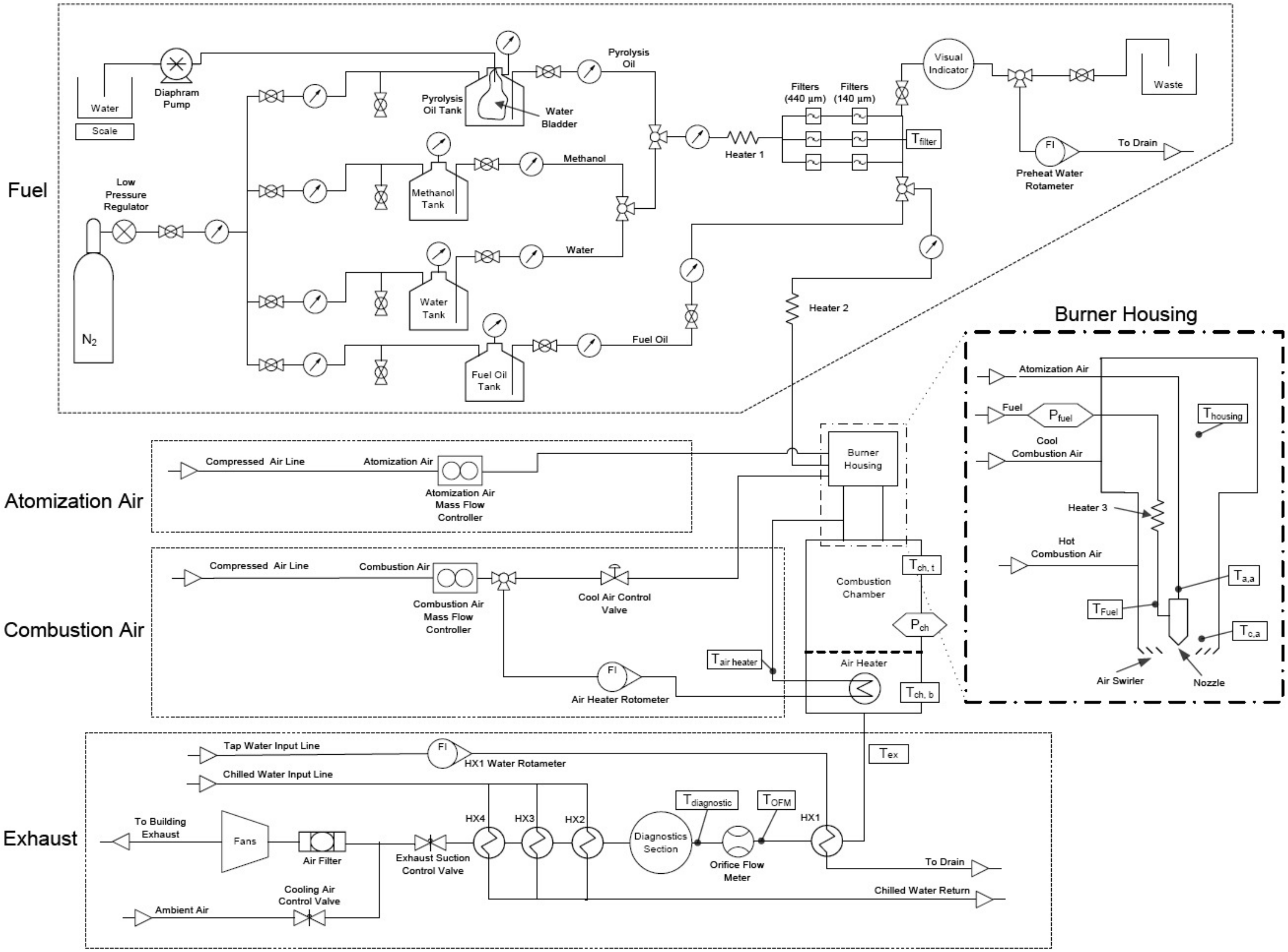

Figure 3.10 Process flow diagram of combustion apparatus for air atomization.

It was desired to utilize a pump to deliver pyrolysis oil to the nozzles at a known flowrate; however, efforts to acquire an affordable pump which could handle flammable fuels with high solids and high acidity at low flowrates proved unsuccessful. Instead, a low-cost diaphragm pump was used to pump water into a flexible bladder installed inside of the fuel tank to displace the fuel in the tank, as shown in Figure 3.11. Prior to pumping water into the bladder, the tank was compressed slightly with nitrogen (~3 psig) to get the fuel to a pressure high enough to overcome the static head of the fuel in the line flowing up to the nozzle.

(a) **(b)**

Figure 3.11 Picture of pump (a) and displacement chamber (b).

The fuel preheating system and method for switching between fuels is the same as that used with pressure atomization. Because the air atomization nozzles have much larger passages for fuel flow, the requirements for filtration are not as stringent. For the air atomization nozzles, three 140 micron filters were used in parallel.

The diaphragm pump provides ample control over the flowrate of the water into the bladder. The flowrate of fuel from the tank is dictated by the head between the fuel tank and nozzle. As the atomization air flowrate through the nozzle was varied, the head between the tank and nozzle exit varied due to the siphoning effect of the nozzle design.

If the atomization air rate is decreased such that the siphoning effect is reduced generating a higher fuel pressure at the nozzle, then the pressure in the tank must increase slightly to deliver the same fuel flowrate. As water was pumped into the bladder, the fluid level in the tank was allowed to increase and the nitrogen in the head space of the tank allowed to compress, such that the pressure in the tank could increase.

If the flow through the nozzle reached a steady state condition, the pressure at the nozzle would stabilize at a steady-state reading. Under these conditions, the rate of water flow into the bladder would be equal to the flow of water out of the tank. The fuel flowrate was then determined by measuring the weight of water leaving the water tank, in similar fashion to the flowrate method used in pressure atomization. Once the nozzle pressure was found to stabilize at a constant reading, then the volumetric flowrate of the water is equal to the flowrate of the fuel. The pressure transducer used at the nozzle has an accuracy of 0.7 -inH2O, with an operating range of ±5 psig. It was necessary to measure at both positive and negative gauge pressures, as the atomization air rate through the nozzle could allow for the fuel pressure to range from negative to positive.

To achieve warm up and shut down with fuel oil, the fuel was delivered to the nozzle by controlling the pressure in the fuel oil tank. Although this was a crude method of delivering the fuel to the nozzle, it was sufficient for operation during warm up and shut down. For studies in which fuel oil was studied, a bladder was placed in the fuel oil tank and the same fuel delivery and control system as that of the pyrolysis oil was utilized.

The flow of atomization air to the nozzle was controlled through the use of an Alicat mass flow controller supplied with compressed air. The range of the controller is 0-100 slpm with an accuracy of ±(0.8% of reading + 0.2% of full range).

3.1.3 Combustion Air Delivery and Control

The flow of combustion air to the combustor wascontrolled with an Alicat mass flow controller with a range of 0-1500 slpm with an accuracy of ±(0.8% of reading + 0.2% of full range). Compressed air was used to supply this flow.

The combustion air flowing to the chamber was divided before reaching the chamber, with a portion of the flow travelling through the heat exchanger in the bottom of the combustion chamber and the remainder of the flow travelling directly to the burner housing. The hot air was introduced slightly downstream of the burner housing, directly into the burner tube as shown in Figure 3.8. Each of the combustion air pathways have a needle valve which allows for control of the flowrates. A rotameter was installed to observe the flowrate of air through the heat exchanger. This adjustment allows for control over the final combustion air temperature which was measured at the exit of the burner tube directly before the air swirler.

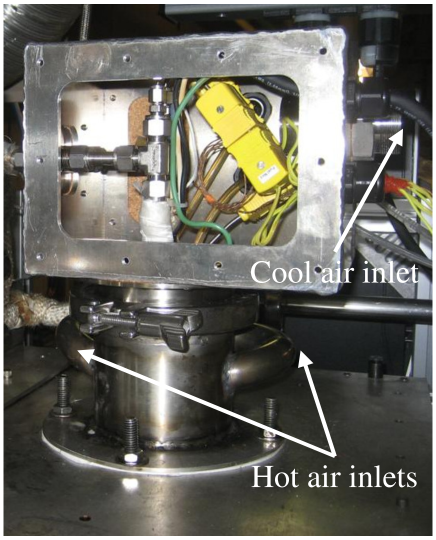

Figure 3.12 Combustion air inlets on burner tube and housing.

3.1.4 Exhaust Handling

The hot exhaust gases were required to be filtered and cooled to 60 °C before exiting into the building duct system. To meet these requirements a 4 stage heat exchanger was developed. Each heat exchanger consists of water flowing through ¼" copper tubing coiled inside of a 4" exhaust duct.

The first heat exchanger stage utilized tap water flowing in a counter-flow arrangement. Under typical heat loads, the water boiled in the heat exchanger, providing very high heat transfer rates and a significant decrease in exhaust temperatures.

The next three heat exchangers utilized chilled water split in parallel between the three sections. These heat exchangers use the same copper tubing/exhaust duct design. By splitting the chilled water in parallel between three sections, the water flowrate through the heat exchangers could be increased significantly. All three heat exchangers operated in a counter-flow arrangement.

Two duct fans are used to pull the exhaust gases through the heat exchangers. A tee joint with a valve allows for additional air from the room to be pulled into the exhaust for further temperature reduction. Filters were placed on both the inlet and exits of the fan to ensure that the exhaust gas is free of particulate before entering the building duct system.

3.1.5 Orifice Flowmeter

The duct fans used to pull the exhaust from the chamber were capable of pulling a slight vacuum in the chamber such that additional air could leak into the exhaust gases. A valve installed in the exhaust allowed for the suction of the fans to be reduced so that the mass flow into the chamber could be equated to the mass flow of exhaust leaving the chamber. This flowrate was measured with an orifice flowmeter which has been built and calibrated for use in this combustion apparatus. The design and calibration of this instrument is discussed in APPENDIX A.

3.1.6 Data Acquisition System

A National Instruments cDAQ-9172 data acquisition card and LabVIEW software were used to take measurements necessary for monitoring the combustion apparatus (shown in Figure 3.13 and Figure 3.14). The thermocouple readings are shown throughout the process flow diagram in Figure 3.10. Two of the pressure transducers were used to measure the pressure difference across the orifice flowmeter. Another pressure measurement was used for readings of the chamber pressure and the final pressure measurement monitored the pressure of the fuel at the nozzle.

Figure 3.13 Data acquisition control box.

Serial port connections to the computer were used to communicate with the Alicat mass flow controllers. A serial port connection was also used to record readings from the scale used to determine the fuel flowrate measurement. Omega CN7800 temperature controllers were used to control the temperatures for each of the fuel heaters.

The accuracy of control over some of the key variables in this work is outlined in Table 3.1. For most of the combustion studies performed, it was desirable to set the equivalence ratio of combustion. Based on the values in Table 3.1 the accuracy in setting the equivalence ratio in these studies was approximately ± 0.01.

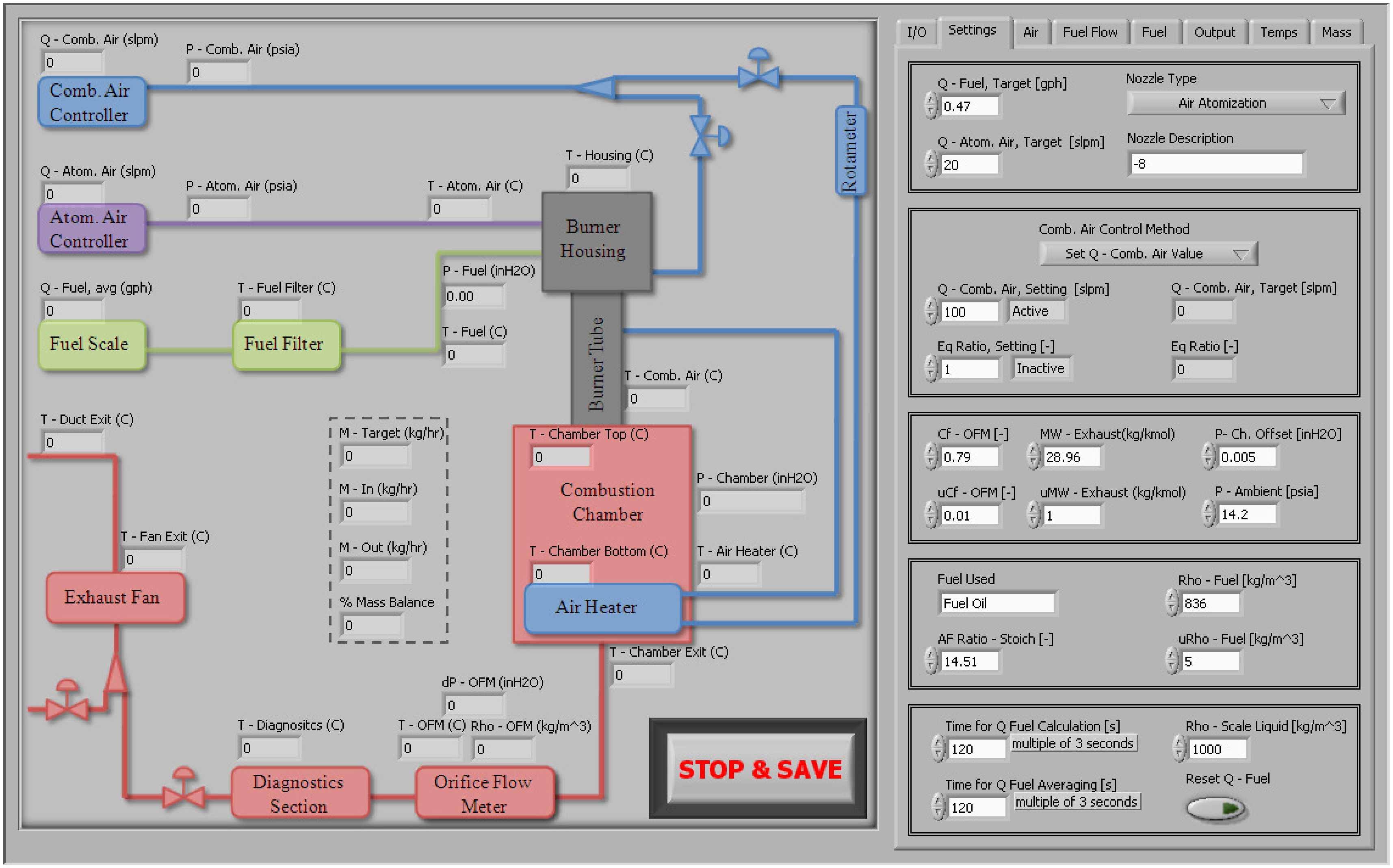

Q - Comb. Air (slpm) 0
P - Comb. Air (psia) 0
Q - Atom. Air (slpm) 0
P - Atom. Air (psia) 0
T - Atom. Air (C) 0
T - Housing (C) 0
Q - Fuel, avg (gph) 0
T - Fuel Filter (C) 0
P - Fuel (inH2O) 0.00
T - Fuel (C) 0
T - Comb. Air (C) 0
T - Duct Exit (C) 0
M - Target (kg/hr) 0
M - In (kg/hr) 0
M - Out (kg/hr) 0
% Mass Balance 0
T - Chamber Top (C) 0
P - Chamber (inH2O) 0
T - Chamber Bottom (C) 0
T - Air Heater (C) 0
T - Fan Exit (C) 0
T - Chamber Exit (C) 0
dP - OFM (inH2O) 0
T - Diagnositcs (C) 0
T - OFM (C) 0
Rho - OFM (kg/m^3) 0

Q - Fuel, Target [gph] 0.47
Nozzle Type Air Atomization
Q - Atom. Air, Target [slpm] 20
Nozzle Description -8

Comb. Air Control Method Set Q - Comb. Air Value
Q - Comb. Air, Setting [slpm] 100 Active
Q - Comb. Air, Target [slpm] 0
Eq Ratio, Setting [-] 1 Inactive
Eq Ratio [-] 0

Cf - OFM [-] 0.79
MW - Exhaust(kg/kmol) 28.96
P- Ch. Offset [inH2O] 0.005
uCf - OFM [-] 0.01
uMW - Exhaust (kg/kmol) 1
P - Ambient [psia] 14.2

Fuel Used Fuel Oil
Rho - Fuel [kg/m^3] 836
AF Ratio - Stoich [-] 14.51
uRho - Fuel [kg/m^3] 5

Time for Q Fuel Calculation [s] 120 multiple of 3 seconds
Rho - Scale Liquid [kg/m^3] 1000
Time for Q Fuel Averaging [s] 120 multiple of 3 seconds

Figure 3.14 Screenshot of data acquisition system software interface.

Table 3.1 Measurement and/or control accuracies of key variables.

Variable	Accuracy
Fuel Flowrate	± 0.01 gph
Fuel Temperature	± 2 °C
Fuel Pressure (Pressure Atomization)	± 0.75 psig
Fuel Pressure (Air Atomization)	± 0.7 -inH2O
Atomization Air Flowrate	± 0.3 slpm
Combustion Air Flowrate	± 5 slpm
Combustion Air Temperature	± 5 °C
Exhaust Flowrate	± 0.75 kg/hr (± 10 slpm air)

3.2 Fuel Property Measurements

The fuels studied in this research have been well characterized, with measurements of water content, water insoluble fraction, higher heating value, viscosity, and surface tension. Additionally, ultimate and proximate analyses have been performed. For each of these measurements a minimum of three tests were performed on each sample. Further, gas chromatography/mass spectroscopy (GC-MS) has been used to determine the chemical species in the fuel samples and energy-dispersive X-ray spectroscopy has been used to analyze the elemental composition of the ash found in the oil.

Six different fuel samples have been investigated in this research. This first of these is No. 2 light fuel oil (LFO), which has served as a baseline fuel for comparison. This sample is referred to as “Fuel Oil.” Two samples of pine-derived pyrolysis oil have been studied, both of which were produced by Biomass Technology Group. These samples differ only in that they came from two different batches, such that their properties were slightly different. These samples are referred to as “Pine I” and “Pine II.” An emulsion of 30% Pine I oil in Fuel Oil was produced with Atlox 4912 used as a surfactant. This sample is referred to as “Emulsion,” however, the quality of this emulsion was poor given that it was stable only for a few days after being vigorously mixed.

The final two samples were made by Biomass Technology Group and produced from corn fiber, which is the outer shell of corn kernels and is a byproduct of wet-milling of corn grains. The raw batch of corn fiber derived oil was found to have significant variability with regard to its properties as will be discussed. This variability was found to correspond with variations in sample density as well, such that a natural separation occurred in the oil given sufficient time. By drawing samples of the corn fiber derived oil after it settled sufficiently, a greatly improved degree of measurement repeatability was achieved. The raw batch of the corn fiber derived oil is referred to as “Corn Mix” while the extracted sample of oil is simply referred to “Corn Fraction.”

Water was added to the Pine I oil in varying amounts to investigate the effects of water content on pyrolysis oil combustion. These samples are labeled “Pine II - 23% Water,” “Pine II – 24.5% Water,” and “Pine II – 26% Water.”

3.2.1 Water Content

The mass fraction of water present in the fuel samples has been measured using Karl Fischer titration according to standard ASTM E203. The reagent used is Hydranal

Composite 5K and the solvent used is Hydranol Working Medium K, which are appropriate for mixtures containing aldehydes and ketones.

3.2.2 Higher Heating Value

The higher heating value of the fuel samples has been measured using a Parr 1341 Oxygen Bomb Calorimeter. These measurements follow standard ASTM D240.

3.2.3 Ultimate Analysis (C,H,N,O)

The carbon (C), hydrogen (H), and nitrogen (N) contents of the fuel samples has been measured using a LECO TruSpec CHN Analyzer. Carbon and hydrogen are detected through non-dispersive infrared absorption (NDIR), while nitrogen is detected with a thermal conductivity sensor. These measurements follow standards ASTM D5291 and ASTM D5373. Oxygen is calculated by difference, assuming that the whole of the fuel is composed only of C, H, N, and O. Sulfur was not measured as the pyrolysis oil samples were expected to be very low in sulfur content.

3.2.4 Proximate Analysis

Proximate analysis of the fuel samples has been performed using a Mettler Toledo TGA/DSC 1 thermogravimetric analyzer. Measurements have been carried out according to standard ASTM D5142 to provide the mass fractions of moisture, volatiles, fixed carbon, and ash present in the samples. The moisture value measured in the proximate analysis is generally higher than the water content measured through Karl-Fischer titration, because this moisture value includes all chemical present in the sample which volatilize at 100 °C.

3.2.5 Acidity

The acidity of the fuels used in this study was characterized by determining the pH level of the samples. The pH level was measured using a Corning 320 pH meter.

3.2.6 Solids Content

The mass fraction of solid content in pyrolysis oil is determined by dissolving a sample oil methanol at a ratio of 1:100 and separating the remaining sediment which fails to dissolve in the methanol through filtration[33, 70]. The methanol insoluble fraction is considered to represent the solid particulate content in the oil as outlined by Oasmaa and Meier [33, 70].

3.2.7 Water Insoluble

The water insoluble fraction of the oil is determined by dissolving pyrolysis oil at a ratio of 1:20 in water at 50 °C. After thorough mixing, the sediment remaining is collected and weighed to determine the mass fraction of water insoluble content in the oil. This methodology has been developed by the Center for Sustainable Energy and Technology (CSET) at Iowa State University, and is a modification to methods outlined by Oasmaa and Meier [33, 70].

Researchers have historically considered the water insoluble fraction of oil to represent the fraction of pyrolysis oil which is derived from lignin in the biomass [33, 70]. However, this view has come under review by researchers at CSET and others in the field [71].

3.2.8 Viscosity

Viscosity of the fuel samples has been measured using a Brookfield DVII+ viscometer. This device measures the torque on a rotating cylinder which is submerged in the fluid to be tested. The torque is correlated to the shear stress on the fluid, while the rotational speed of the spindle is correlated to the shear rate of the fluid. This information is then used to determine the viscosity of the fluid. By taking measurements at varying rotational speeds (i.e. shear rates), the shear-dependent nature of the viscosity can be determined. Further, this device allows for measurements at varying sample temperatures both above and below ambient temperature. Measurements of viscosity have been made for temperatures up to 90 °C.

3.2.9 Surface Tension

Surface tension was measured using a KSV Sigma 703 surface tensiometer. This device operates by measuring the force of a sample fluid acting on a thin plate at the surface of the fluid as shown in Figure 3.15.

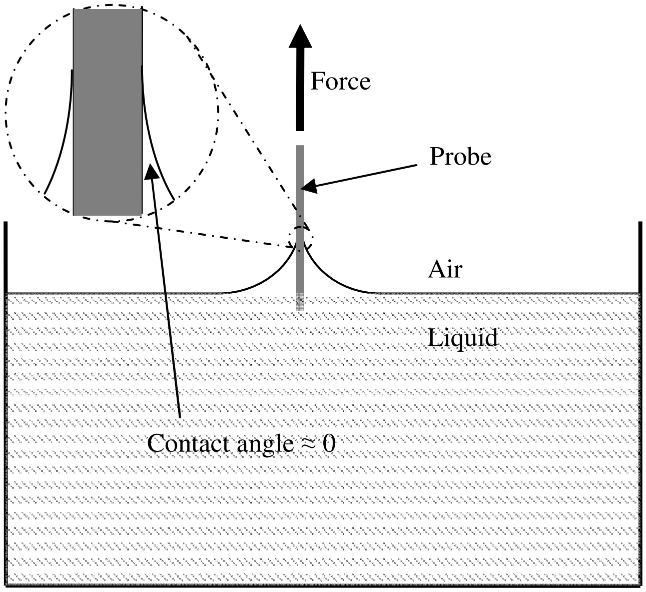

Figure 3.15 Surface tension measurement method.

To achieve a proper measurement of surface tension, the probe must be made of a material with a high wettability, such that the contact angle between the probe and the fluid approaches zero. The probe which is utilized with the KSV Sigma 703 device is made of platinum because of its inherently high wettability. However, this presents a potential problem for measuring the surface tension of pyrolysis oils.

Pyrolysis oil is very sticky and can stain surfaces easily. As such, there is some potential of causing damage to the platinum probe. Moreover, one of the most effective solvents for cleaning pyrolysis oil is methanol. Unfortunately, platinum catalyzes methanol to formaldehyde in a highly exothermic reaction. As such, attempts to clean the probe with methanol could also damage the probe as well.

Rather than risking damage to the platinum probe, a glass probe was developed instead. Glass has a high wettability and is chemically resistant to both pyrolysis oil and methanol. The glass probe developed weighs 1.06 g and has a width of 22 mm, while the platinum probe weights 1.15 g and has a width of 19.6 mm. Although the probes are not identical, calibration of the probe has allowed for repeatable and accurate readings.

Because combustion and spray studies are being performed with the fuels operating at elevated temperatures, it is of interest to know the temperature dependence of the surface tension. To attain this information, the sample container has been placed on a hot plate and the temperature of the sample measured with a K-type thermocouple.

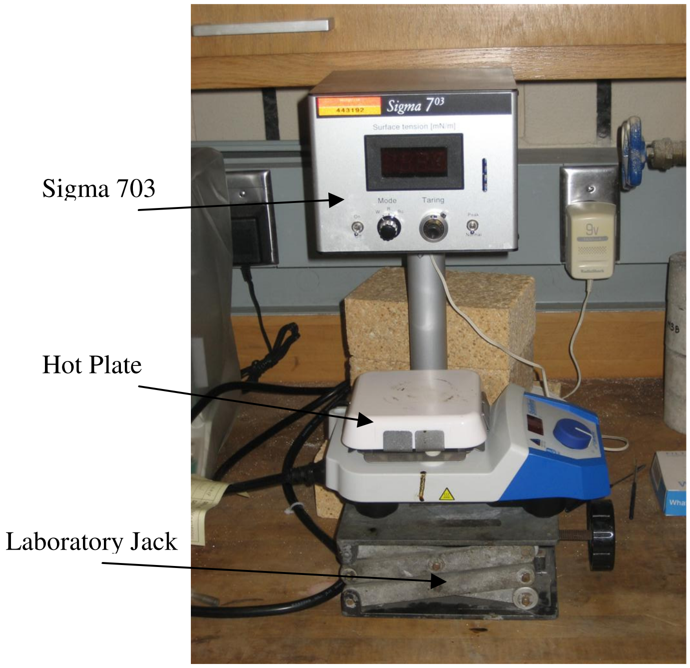

Figure 3.16 Picture of modified surface tension apparatus.

To calibrate the glass probe, fluids of varying surface tension were measured at different temperatures with both the platinum and glass probes. Mixtures of ethanol and water in different ratios provided a wide range of surface tension values for calibration. The calibration curve for the glass probe is shown in Figure 3.17.

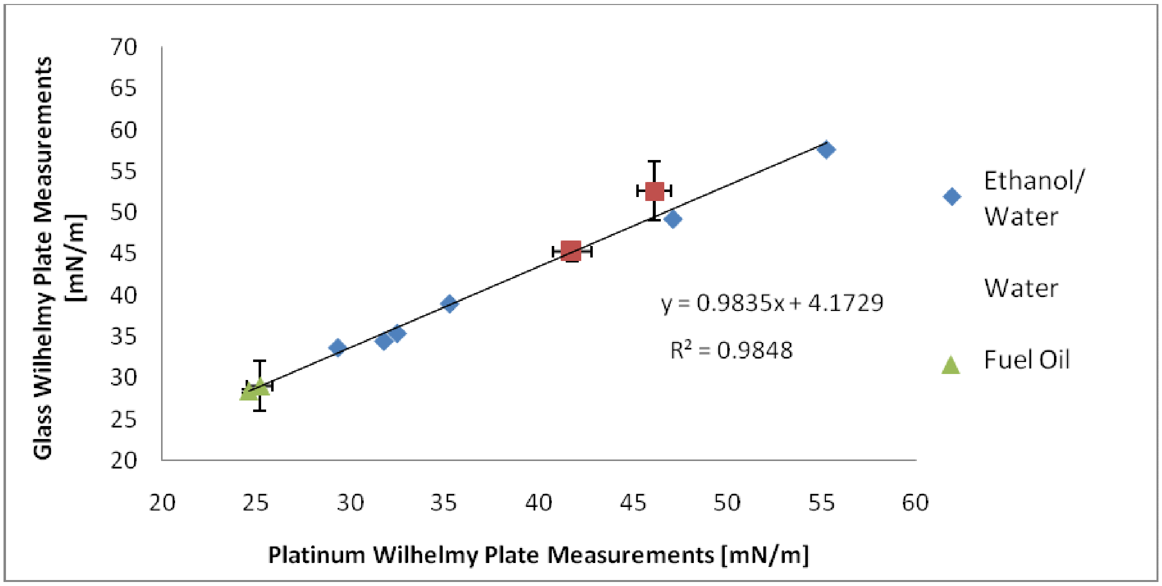

Figure 3.17 Calibration curve for glass probe for surface tension measurement.

The calibration of the probe follows a linear profile; however, this correlation does not pass through the origin as would be expected. This could be caused by an offset in material wettability. The uncertainties in the fuel oil and water data points were fairly large; however, the ethanol/water mixtures provided very repeatable results.

3.2.10 Gas Chromatography/Mass Spectrometry

A Varian Saturn 2200 GC/MS with an internal standard was used to perform gas chromatography/mass spectroscopy analyses of the fuel samples to reveal differences in the chemical compositions of the fuels. Because pyrolysis oils are comprised of many chemical components, several of the species present in the oil remain unidentified in the data presented from the measurements. However, the data presented does serve as an indicator of chemical differences between various fuel samples.

3.2.11 Energy-Dispersive X-ray Spectroscopy

A JEOL 840A SEM was used to image samples of ash collected during TGA analysis of the fuel samples. Energy-dispersive X-ray Spectroscopy (EDS) was used to analyze the samples to determine the elemental composition of these samples

3.2.12 Fuel Property Measurement Results

The uncertainty of the fuel property measurements varied with regard to the test performed and the fuel studied. The typical repeatability in the measurement values is shown in Table 3.2, based on a 95% confidence interval.

For all fuel samples, the fuel batch was well stirred for 5 minutes before withdrawing a sample, to ensure that a representative sample was drawn. For the pine derived pyrolysis oil samples this method worked very well; however, for the corn fiber derived oils, there was significant variation between each sample drawn. This variability is shown in Table 3.3.

The variations in properties of this oil are very noteworthy and would likely serve as an interesting study in and of themselves. However, for the sake of studying a fuel with a well characterized set of properties, this variation is undesirable. Samples A and B of the Corn Mix both had high densities with properties somewhat more similar to the pine derived oils, allowing for more meaningful comparisons to be drawn between the fuels. By allowing the batch of oil to settle for several days, a fraction of the oil was extracted from the bottom of the container and each sample characterized. These samples showed a greatly reduced variation in properties as seen in Table 3.4.

Table 3.2 Typical repeatability of fuel characterization measurements.

	Repeatability
Water Content	1.2 wt-%
Density	0.009 kg/L
Solids Content	0.08 wt-%
Water Insolubles	0.03 wt-%
HHV	0.15 MJ/kg
Proximate Analysis	
Moisture	1.2 wt-%
Volatiles	1.6 wt-%
Fixed Carbon	0.7 wt-%
Ash	0.02 wt-%
Ultimate Analysis	
C	0.7 wt-%
H	0.1 wt-%
N	0.02 wt-%
Kinematic Viscosity [cSt]	
at 40 °C	37 % of measurement
at 50 °C	11 % of measurement
at 60 °C	7 % of measurement
at 70 °C	2.6 % of measurement
at 80 °C	1.1 % of measurement
at 90 °C	0.7 % of measurement
Surface Tension [mN/m]	2 % of measurement

The fuel properties of the Pine I samples of varying water content are shown in Table 3.5. Each value reported is an average of at least three measurements. Viscosity and surface tension values were measured for the Pine II - 24.5% Water and Pine II - 26% Water samples; however, all other values were calculated based on the measurements of the baseline Pine II oil (i.e. Pine II - 23% Water) and the knowledge of the amount of water added to the other samples. The detailed findings of the viscosity and surface tension measurements are discussed in 0 and APPENDIX C, respectively.

Table 3.3 Summary of Corn Mix oil properties

	Corn Fiber Mix A	Corn Fiber Mix B	Corn Fiber Mix C	Corn Fiber Mix D	Corn Fiber Mix Average
Water [wt-%]	24.3	10.7	23.6	20.3	19.7
Density [g/ml]	1.176	1.021	1.178	1.121	1.124
Water Insolubles [wt-%]	76.2	n.m.	n.m.	48.8	62.5
HHV [MJ/kg]	18.73	29.02	19.09	22.77	22.40
Proximate Analysis [wt-%]					
Moisture	22.8	3.9	26.8	8.7	15.6
Volatiles	59.1	91.4	52.5	81.2	71.0
Fixed Carbon	19.6	4.7	20.7	10.0	13.8
Ash	0.04	0.04	0.02	0.12	0.06
Ultimate Analysis [wt-%]					
C	42.9	63.5	43.5	49.5	49.9
H	7.8	9.6	8.0	8.5	8.5
N	1.45	0.91	1.50	1.32	1.30
O	47.8	26.0	47.1	40.6	40.4
O, fuel-bound	26.2*	16.5*	26.1*	22.5*	22.8*
Kinematic Viscosity [cSt]					
at 40 °C	139	288	177	547	288
at 50 °C	64	131	67	218	120
at 60 °C	29	105	33	63	58
at 70 °C	18.5	75.5	19.7	48.1	40.5
at 80 °C	12.3	31.4	13.1	25.8	20.7
at 90 °C	8.7	25.0	9.2	17.1	15.0

n.m. = not measured
*calculated from other known property data

Table 3.4 Summary of Corn Fraction oil properties

	Corn Fiber Fraction A	Corn Fiber Fraction B	Corn Fiber Fraction C	Corn Fiber Fraction D	Corn Fiber Fract. Average
Water [wt-%]	26.0	27.0	26.8	26.3	26.5
Density [g/ml]	1.207	1.209	1.218	1.198	1.208
Water Insolubles [wt-%]	26.7	27.2	n.m.	n.m.	27.0
HHV [MJ/kg]	16.47	16.69	16.59	16.74	16.62
Proximate Analysis [wt-%]					
Moisture	28.3	28.3	28.4	28.6	28.4
Volatiles	51.9	49.2	50.5	49.2	50.2
Fixed Carbon	19.8	22.4	21.1	22.1	21.3
Ash	0.03	0.09	0.02	0.05	0.05
Ultimate Analysis [wt-%]					
C	39.1	39.0	38.8	39.0	39.0
H	7.6	7.6	7.6	7.6	7.6
N	1.60	1.58	1.67	1.58	1.61
O	51.7	51.8	51.9	51.9	51.8
O, fuel-bound	28.5*	27.8*	28.1*	28.5*	28.3*
Kinematic Viscosity [cSt]					
at 40 °C	66.5	66.8	67.8	67.3	67.1
at 50 °C	38.2	38.8	38.8	38.9	38.7
at 60 °C	23.7	24.1	23.7	24.5	24.0
at 70 °C	15.4	15.9	15.5	15.9	15.7
at 80 °C	10.8	11.1	11.2	11.2	11.1
at 90 °C	8.1	8.6	8.3	8.4	8.4

n.m. = not measured
*calculated from other known property data

The property data for the five major fuel samples tested in this research are summarized in Table 3.6. The Pine I and Pine II samples have similar properties, with the water content being slightly lower for Pine II. This corresponds to a slight increase in heating value and viscosity. The difference in heating value between Pine I and Pine II appears to be attributable to more than just the difference in water content, suggesting that there may be some difference in species concentration. This may also be explained by the fact that the measurement uncertainty in the water content measurement is approximately 1wt-%, causing a misinterpretation of the impact of water content between the Pine I and Pine II oils. The significance of the change of heating value can be seen in the difference between the adiabatic flame temperatures of the Pine I and Pine II oils, especially in regard to the small difference which occurs between the varying water contents of the Pine II oil as shown in Table 3.5. Surface tension measurements were not taken for Pine II, because given the similarity between Pine I samples of varying water content shown in Table 3.5 and the other similarities between Pine I and Pine II, it is likely that the surface tension values will not differ substantially. The pine derived and corn fiber derived oils differed slightly with regard to energy content and heating value, with the Corn Fraction fuel having a higher water content and lower energy content. However, despite the increased water content, the Corn Fraction oil is more viscous that the pine derived oils. On an elemental analysis, the corn fiber derived oil has rather high nitrogen content, although the fuel-bound oxygen levels are very similar to that of the pine oils. The proximate analysis shows that the Corn Fraction oil has a slightly reduced moisture content and slightly increased fixed carbon content .

The GC-MS retention time plots for Pine I and Pine II fuels are shown in Figure 3.18. As expected, the Pine I and Pine II fuels have nearly identical chemical compositions.

The GC-MS retention time plots for Pine I and Corn Fraction fuels are shown in Figure 3.19. The Corn Fraction sample appears to have far fewer and diminished peaks when compared with Pine I fuel. There are several peaks in the Pine I sample which do not appear in the Corn Fraction sample and vice-versa. Further, there are a few peaks near the phenol groups which are unidentified. Some of the identified species may be nitrogen containing compounds.

Table 3.5 Summary of Pine II oil properties

	Pine II (23% Water)	Pine II - 24.5% Water	Pine II - 26% Water
Water [wt-%]	23.0	24.5*	26.0*
Density [g/ml]	1.180	1.176*	1.172*
Water Insolubles [wt-%]	28.9	28.4*	27.8*
HHV [MJ/kg]	17.99	17.65*	17.30*
Adiabatic Flame Temp. [K]†	2188*	2182*	2161*
Air-Fuel Ratio [-]	5.48*	5.35*	5.27*
Proximate Analysis [wt-%]			
Moisture	33.5	n.m.	n.m.
Volatiles	51.0	n.m.	n.m.
Fixed Carbon	15.4	n.m.	n.m.
Ash	0.02	n.m.	n.m.
Ultimate Analysis [wt-%]			
C	43.2	42.4*	41.6*
H	7.7	7.7*	7.8*
N	0.0	0.0*	0.0*
O	49.1	49.9*	50.6*
O, fuel-bound	28.7*	28.1*	27.5*
Kinematic Viscosity [cSt]			
at 25 °C	99.3	90.3	69.8
at 40 °C	35.4	33.6	30.1
at 50 °C	20.5	19.0	17.1
at 60 °C	12.8	12.0	11.0
at 70 °C	8.6	7.9	7.3
at 80 °C	6.0	5.6	5.2
at 90 °C	4.5	4.1	3.9
Surface Tension [mN/m]			
at 25 °C	34.6	34.7	34.9
at 40 °C	33.1	33.7	33.6
at 60 °C	32.3	31.8	32.4
at 80 °C	31.5	31.3	31.3

n.m. = not measured
*calculated from other known property data
†neglecting dissociation

Table 3.6 Summary of fuel properties.

	Fuel Oil	Emulsion	Pine I	Pine II	Corn Fraction
Water [wt-%]	0.0	6.6*	22.0	23.00	26.5
Density [g/ml]	0.833	0.939*	1.187	1.180	1.208
Solids [wt-%]	n.m.	n.m.	0.3	n.m.	n.m.
Water Insolubles [wt-%]	n.m.	n.m.	33.4	28.9	27.0
HHV [MJ/kg]	45.98	37.78*	18.65	17.99	16.62
Adiabatic Flame Temp. [K]†	2430*	2401*	2244*	2188*	2200*
Air-Fuel Ratio [-]	14.44*	11.77*	5.53*	5.48*	4.84*
Proximate Analysis [wt-%]					
Moisture	n.m.	n.m.	31.44	33.5	28.4
Volatiles	n.m.	n.m.	53.23	51.0	50.2
Fixed Carbon	n.m.	n.m.	15.32	15.4	21.3
Ash	n.m.	n.m.	0.03	0.02	0.03
Ultimate Analysis [wt-%]					
C	86.9	73.9*	43.6	43.2	39.0
H	13.1	11.5*	7.7	7.7	7.60
N	0.01	0.02*	0.04	0.00	1.61
O	0.00	14.6*	48.7	49.1	51.8
O, fuel-bound	0.00*	8.8*	29.2*	28.7*	28.3*
Kinematic Viscosity [cSt]					
at 25 °C	3.27	n.m.	n.m.	99.3	n.m.
at 40 °C	2.70	n.m.	72.7	35.4	67.1
at 50 °C	2.26	n.m.	31.9	20.5	38.7
at 60 °C	1.92	n.m.	19.1	12.8	24.0
at 70 °C	n.m.	n.m.	12.1	8.6	15.7
at 80 °C	n.m.	n.m.	8.3	6.0	11.1
at 90 °C	n.m.	n.m.	5.9	4.5	8.4
Surface Tension [mN/m]					
at 25 °C	25.2	n.m.	n.m.	34.6	n.m.
at 40 °C	24.6	n.m.	n.m.	33.1	28.3
at 60 °C	n.m.	n.m.	n.m.	32.3	26.5
at 80 °C	n.m.	n.m.	n.m.	31.5	25.1

n.m. = not measured
*calculated from other known property data
†neglecting dissociation

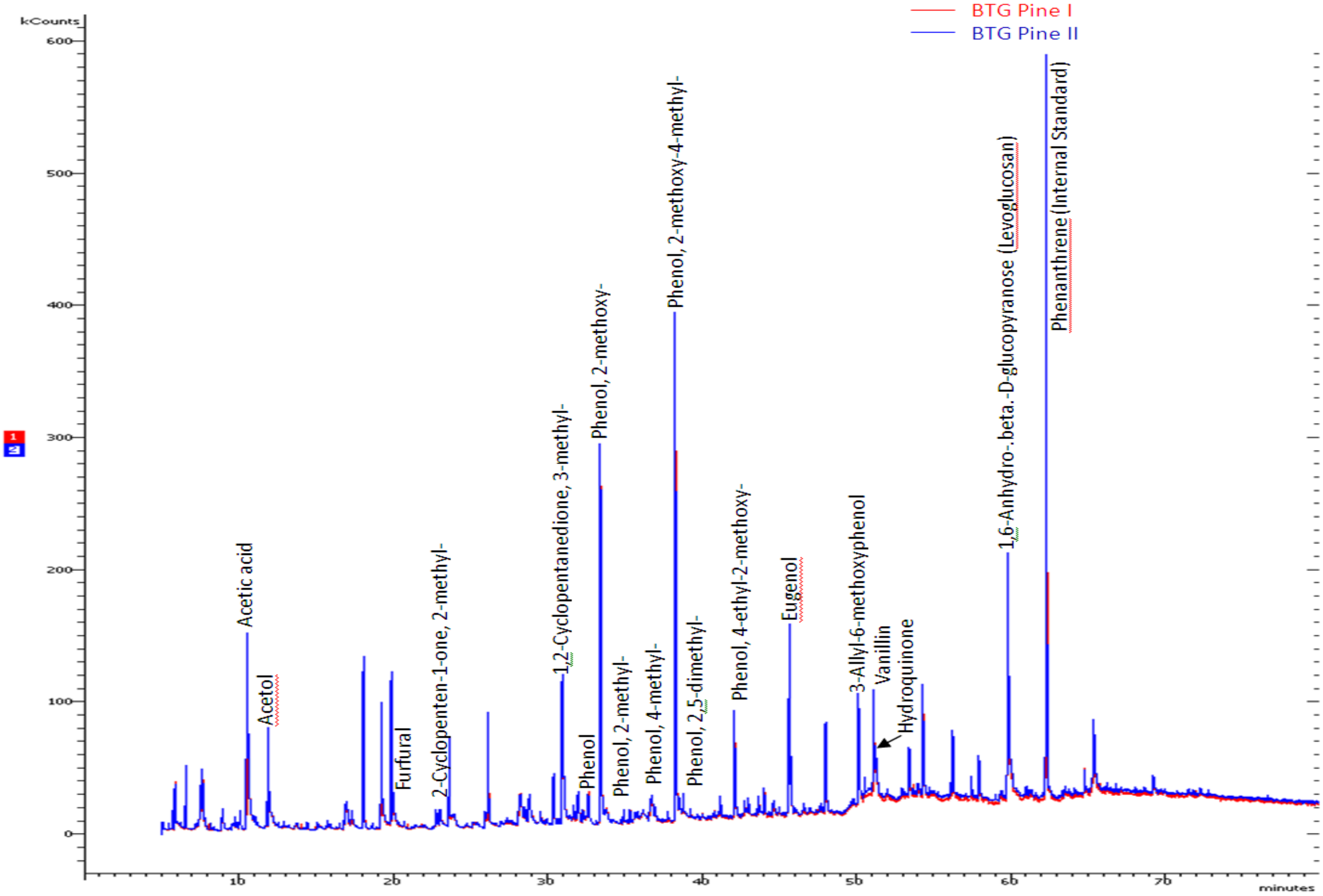

Figure 3.18 GC-MS retention time plots for Pine I and Pine II fuels.

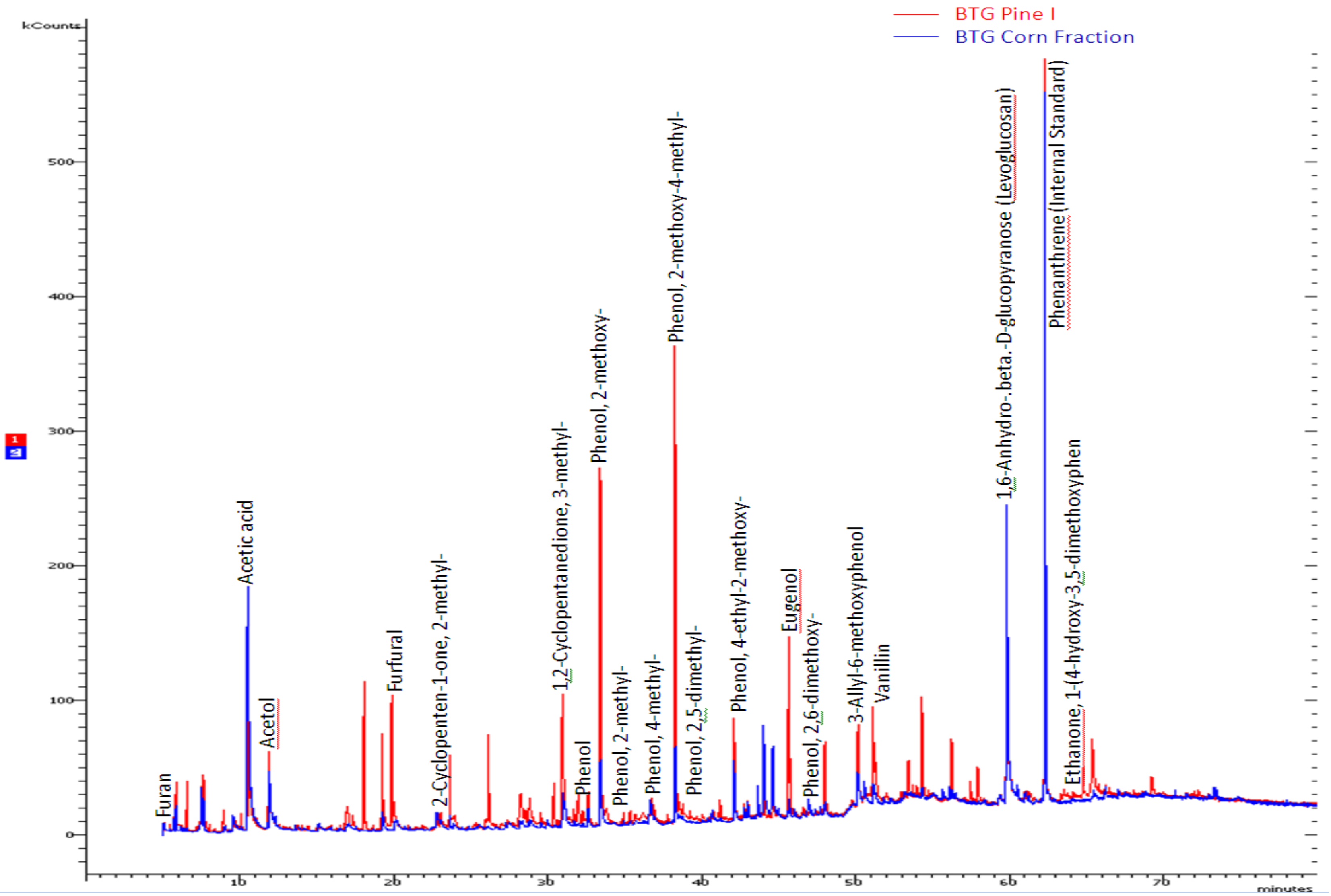

Figure 3.19 GC-MS retention time plots for Pine I and Corn fuels.

Dispersive energy X-ray analysis has been performed on the ash residues from pyrolysis oil samples remaining after the thermogravimetric testing, to provide an elemental composition of the inorganic species in the fuel samples. The results of this analysis for Pine I and Pine II fuel samples is shown in Figure 3.20. Both contain high amounts of aluminum, which is unexpected, since it is not a common soil compound or plant nutrient. This element also appears in high concentration in the Corn Fraction sample as will be shown in Figure 3.21. One possible explanation is that the aluminum has leached into the oil during the pyrolysis oil production process. Both the Pine I and Pine II oils contain sodium, potassium, and calcium, with slight variations in concentration between samples.

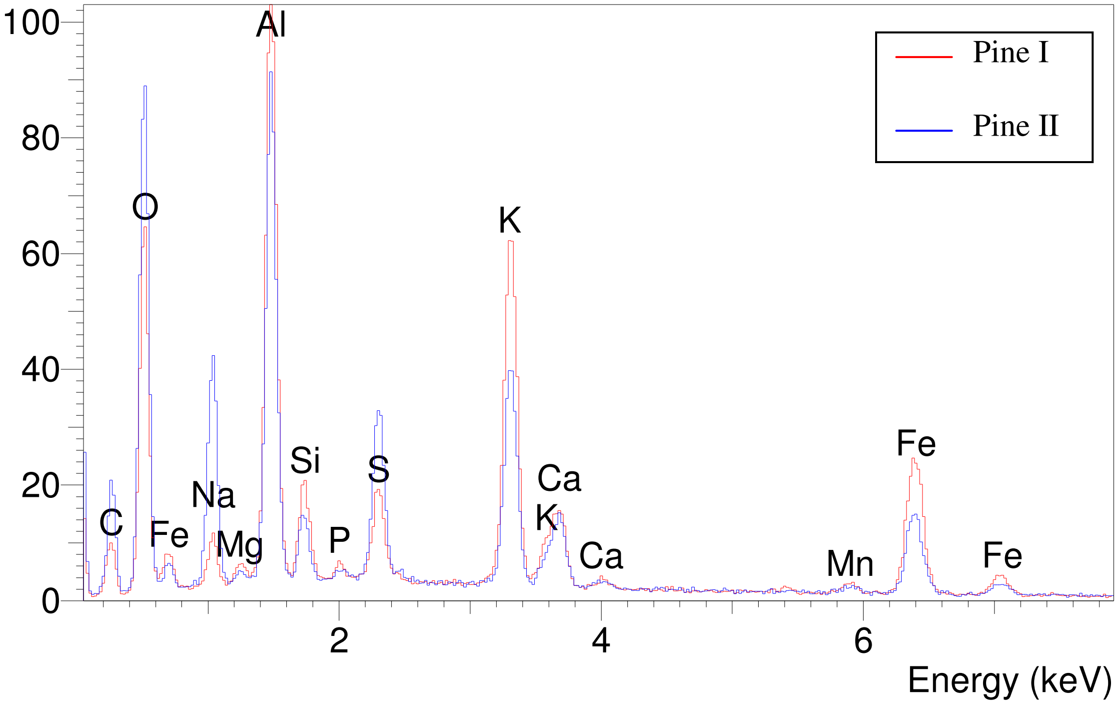

Figure 3.20 Elemental composition of Pine I and Pine II ash samples remaining after TGA analysis.

The results of the energy dispersive X-ray analysis for Pine I and Corn Fraction fuel samples is shown in Figure 3.21. The Corn Fraction sample shows reduced alkali concentration in comparison to the Pine I fuel. This reduction may be the result of a the wet milling process which is used to produce the corn fiber.

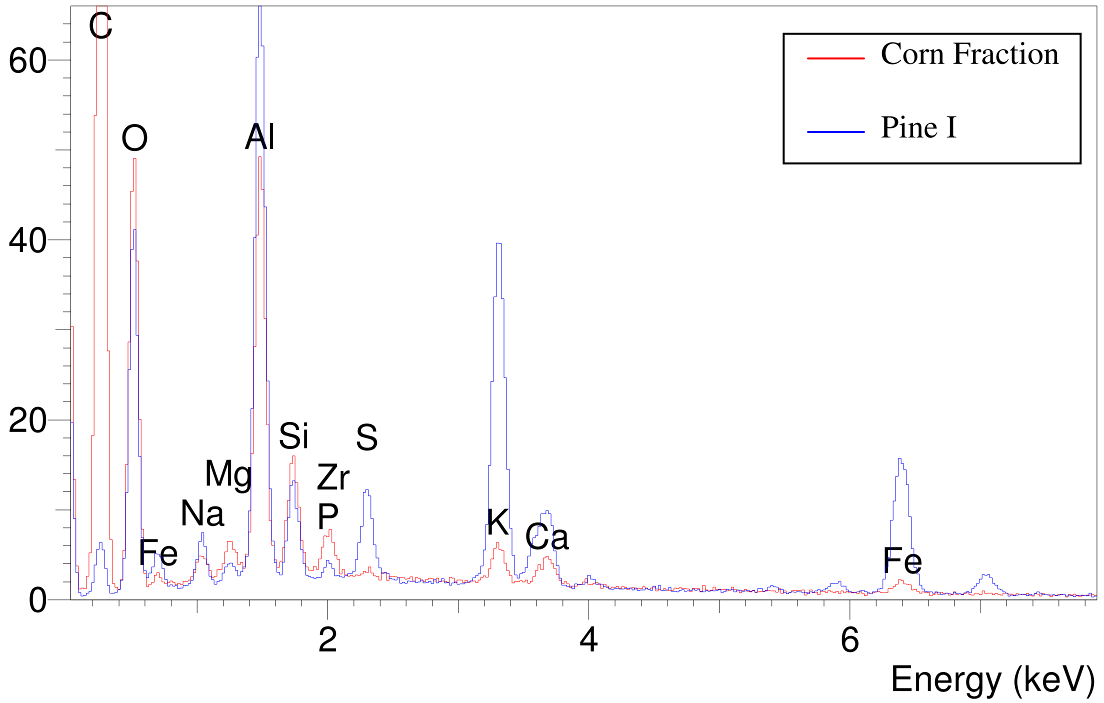

Figure 3.21 Elemental composition of Pine I and Corn Fraction ash samples remaining after TGA analysis.

3.3 Exhaust Emissions Measurements

Exhaust measurements of CO, HC, NOx, and PM have been made just past the orifice flowmeter in the exhaust line, as indicated by the “diagnostics section” in the process flow diagram in Figure 3.9. All values reported represent the average of a minimum of three measurements. All error bars reported on exhaust readings correspond to a 68% confidence interval.

3.3.1 Exhaust Particulate Measurement

An AVL 415S Variable Sampling Smoke Meter operating according to standard ISO 10054 was used to determine the concentration of particulate matter in the exhaust. This measurement draws a sample of exhaust through a filter paper, and the darkness of the filter paper is reported. This darkness, referred to as the filter smoke number (FSN), has been calibrated to PM concentration in units of mg/m^3 by the manufacturer to yield the following calibration correlation [72]

$$\mathrm{PM}_{mg/m^3} = (0.405)\,5.32\,\mathrm{FSN}\,e^{(0.3062\,\mathrm{FSN})} \tag{2.3}$$

The calibration is based on the particulate containing only black soot, specifically produced from combustion of No. 2 light fuel oil. Therefore, the validity of this calibration may be called into question for use in measurements of other fuels, such as pyrolysis oil. However, the PM concentration measurement in units of mg/m^3 has been reported throughout this research, as these units provide more meaningful context than the FSN. Further, because all measurements have been reported in this way, and No. 2 light fuel oil has been used for baseline comparisons, these units serve as a meaningful measure of comparison.

3.3.2 Exhaust Gas Composition Measurement

A Horiba MEXA-554J or a LumaSense ANDROS 6900 gas analyzer were used to measure CO and HC levels in the exhaust depending on the availability of the instrument. Carbon monoxide (CO) and HC levels were measured using Non-Dispersive InfraRed (NDIR) analysis. The unburned hydrocarbons (HC) represent either n-Hexane or Propane. Nitrogen oxide (NOx) could only be measured with the LumaSense ANDROS 6900, which utilizes a chemical sensor for detection.

3.4 Scanning Electron Microscopy

A JEOL 840A scanning electron microscope (SEM) was used to image samples of particulate captured in the filter paper from the exhaust particulate measurements. These images were used to examine the morphology of the particulate. Energy-dispersive X-ray Spectroscopy (EDS) was also used to analyze the samples to determine their elemental composition.

The filter paper used by the AVL 415S during exhaust measurements of particulate has a fibrous structure as can be seen in the representative SEM images shown in Figure 3.22. Although the filter paper did not provide an ideal surface for viewing the particulate, the morphology of the particulate could be clearly identified as is shown in the representative SEM images in Figure 3.23.

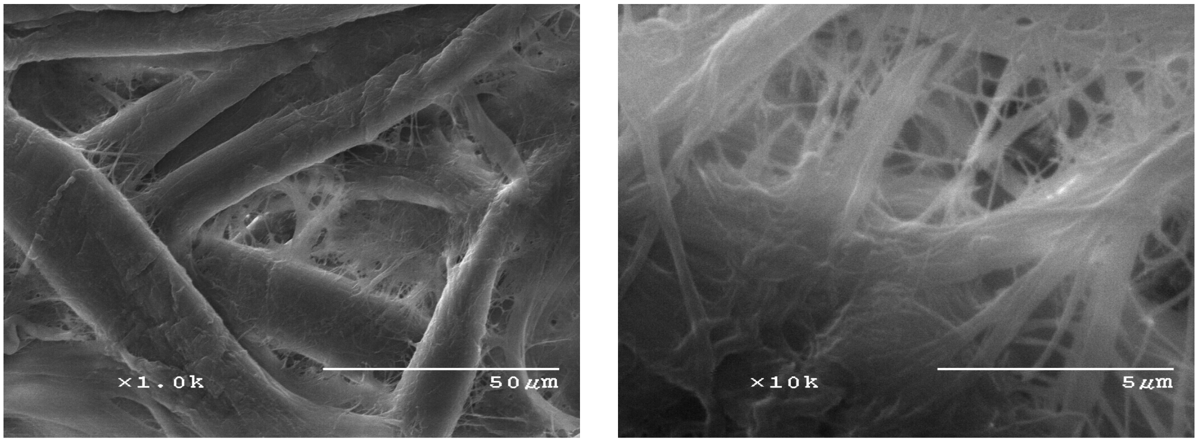

(a) (b)

Figure 3.22 Representative SEM images of blank filter paper at (a) 1000x and (b) 10000x magnification.

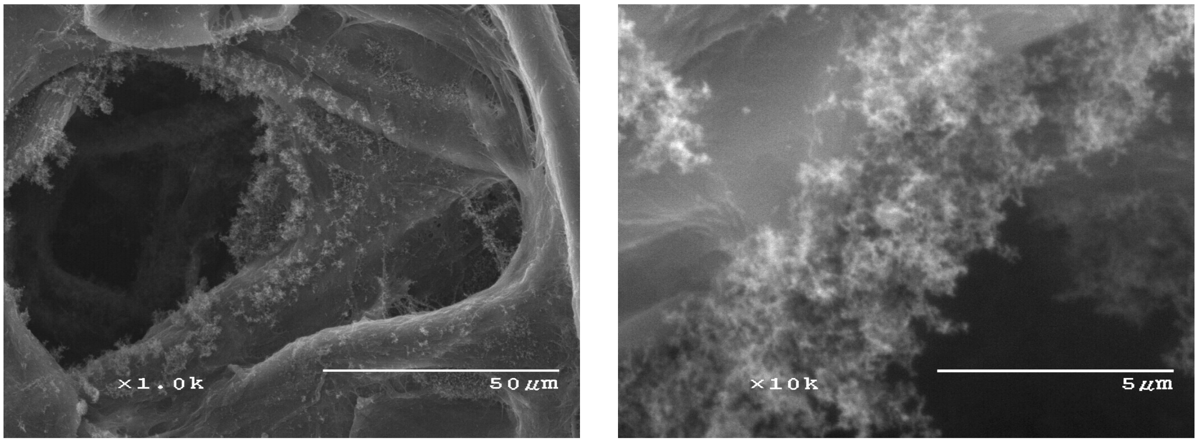

(a) (b)

Figure 3.23 Representative SEM images of particulate on filter paper at (a) 1000 and (b) 10000 magnification.

The particulate shown in Figure 3.23 was collected during the combustion of light fuel oil under rich conditions. Given the known high production of soot in fuel oil flames under rich conditions, the low ash content, and low tendency of light fuel oil to emit stack solids such as cenospheres, the structure of this particulate can be attributed to soot. Moreover, the morphology of the particulate structure is that of very small particles grouped together in large branch-like aggregates, which is the characteristic morphology of soot particles.

A limitation of the SEM images of the particulate is that for low particulate loadings in the filter paper (measurements below 5 mg/m^3), it is not possible to locate and identify particulate in the filter paper. However, visual inspection of the of the filter paper at these low reading conditions allows for the observation of the coloration of the filter paper, which has been shown to be useful in distinguishing between cenospheres and soot.

3.5 Optical Diagnostics

Several optical diagnostic techniques have been employed in this research. These techniques have allowed for the characterization of fuel sprays, flame species, and flow distributions.

3.5.1 Phase Doppler Anemometry

Phase Doppler particle analysis (PDPA) allows for point measurements of particle diameter and velocity distributions [73]. This method operates by crossing two laser beams to establish an interference pattern of known fringe spacing at the intersection point. When a particle passes through the fringe pattern, intermittent scattering from the particle is detected and the rate of this intermittency is correlated to droplet velocity. Because particles travelling through the fringe pattern in either direction will have the same scattering pattern, a slight difference in laser frequency is used to generate a moving fringe pattern. In this manner, particles that are moving with the fringe pattern have a lower frequency and particles moving against the fringe pattern have a higher frequency. The frequency offset is then removed in post processing. To measure particle diameter, two detectors are used, placed at different angles from one another. When a particle passes through the interference pattern, the signals at the two different detectors are phase shifted from one another according to the diameter of the particle. A TSI LDV/PDPA Model FSA 3500/4000 system has been used to perform the PDPA measurements.

3.5.2 Flame Spectroscopy

An Ocean Optics HR4000CG-UV-NIR spectrometer was used to analyze flame radiative emission. This allowed for comparison of both flame intensity as a function of wavelength and to identify prominent flame species such as sodium and potassium.

3.5.3 Flame Imaging

3.5.3.1 Color Camera Imaging

Simple color camera images of the flame have been taken, to provide a representation of the flame comparable to that which is seen by eye. The exposure time of these images is relatively long compared to the turbulent time scales of the flow, such that the flame structures appear blurred, just as they do by eye.

3.5.3.2 Single-Shot Imaging of Flame Luminosity

A Princeton Scientific Instruments (PI-MAX SB) Intensified-Charge-Coupled-Device (ICCD) camera with 1024 by 1024 pixels and gating as low as 5 ns has been used to capture single shot images of the flame. Exposure times of either 200 or 2000 ns were used, depending of the intensity of the flame. These short exposure times allowed for “freezing” the flow and obtaining good spatio-temporal resolution of the flame structures.

3.5.3.3 High Speed Imaging of Flame Luminosity

High speed imaging of flames has been carried out by using a Phantom v7.2 high speed camera. This allows for visualization of the development of luminous flame structures [74]. Averages of these image sets have also been employed in this research to construct an average image of the flame shape and size. Images were collected at a rate of 10,000 frames per second, and exposure times of 2 or 10 μs were used depending on the intensity of the flame.

3.5.4 Planar Laser Imaging Techniques

Several planer laser diagnostics have been employed to visualize a longitudinal cross-section of the flame. A cylindrical lens is used to spread a laser beam into a sheet which is passed through the narrow slit windows and into the combustor as shown in Figure 3.24. Because the initial laser beam has a Gaussian power profile in the radial direction, the energy across the laser sheet is not uniform. As such, the laser sheet is spread far beyond the viewing area to utilize the central, high energy plateau of the laser sheet to produce a relatively uniform energy distribution. The laser sheet illuminates a two-dimensional cross-section of the flame which is then imaged from the perpendicular direction through the large chamber windows. By varying the laser wavelength, camera timing, and spectral filtering, various chemical species and physical phases can be visualized individually in the flame.

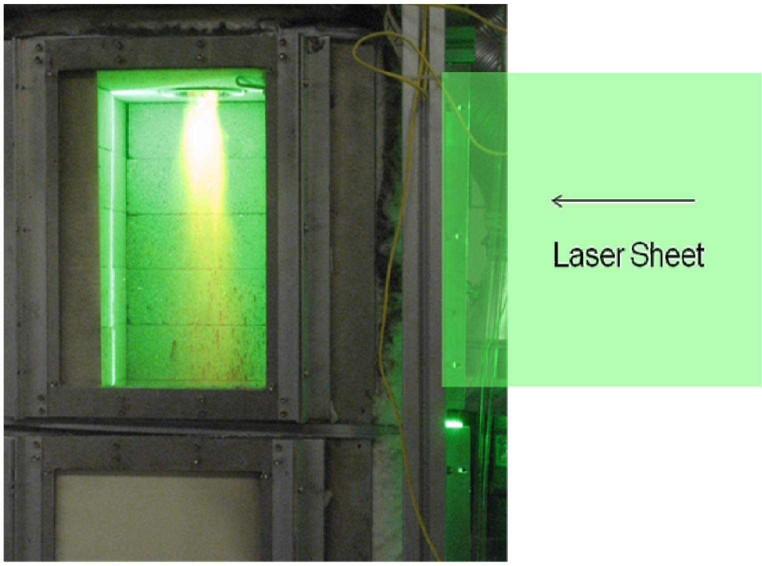

Figure 3.24 Planar laser imaging method.

A frequency-doubled Nd:YAG laser (Spectra-Physics PIV 400) has been used to generate laser pulses at 532 nm wavelength. The PIV 400 laser has two laser cavities which can be fired individually. One beam has been used at the 532 nm wavelength to generate high energy pulses (400-450 mJ/pulse) for Mie scattering and laser induced incandescence (LII) imaging techniques. In some of the studies both laser cavities were combined to generate a very high power 532-nm beam (700 mJ/pulse) for performing LII studies.

When not combined, one of the beams was used to pump a dye laser (Continuum ND6000). Rhodamine 590 dye (Exciton) was utilized to produce a narrow linewidth (~0.08 cm^{-1}) of visible radiation at 567.844 nm, which is then frequency doubled using Type I phase matching in a 10mm by 10mm by 20 mm BBO crystal to produce up to 20 mJ single-pulse energy in the UV. The wavelength of the laser can be tuned to different frequencies as needed for UV fuel fluorescence and hydroxyl radical fluorescence techniques.

For all of the planar laser imaging studies, Princeton Scientific Instruments (PI-MAX SB) Intensified-Charge-Coupled-Device (ICCD) cameras have been used. Two cameras were available during some of the studies such that any of the planar laser imaging measurements or single-shot flame measurements could be taken simultaneously. Because the cameras are intensified, this allows for fast time gating to minimize flame emission and the detection of low signal levels. A Uniblitz VMM-D1 mechanical shutter was used with each camera to reduce background stimulation of the ICCD intensifier between gate exposures.

3.5.4.1 Mie Scattering

Mie scattering is the simple scattering of light from changes in refractive index as present along a phase interface. Unlike Rayleigh scattering, Mie scattering behavior is the same for all wavelength to particle diameter ratios [75]. In Mie scattering, the wavelength of the scattered light is the same as the incident radiation. Because Mie scattering is a surface area phenomena, the signal strength of the scattered light is approximately proportional to the square of the particle diameter.

When a laser sheet is passed into the flame, any non-gaseous materials such as fuel droplets or soot will scatter light in all directions. This scattered signal can be imaged in the perpendicular direction to provide a visualization of the distribution of all non-gaseous materials in the flame. To see only the light scattered from the laser and discriminate against PLIF or LII, temporal and spectral filtering methods are employed.

Mie scattering occurs very rapidly, such that very little time delay is required between the 532 laser pulse and the camera shutter gate. A 20 ns camera gate width was centered over the time of the laser pulse as shown in Figure 3.25. This allows for the camera to always detect the laser signal, despite any slight jitter in the laser pulse timing.

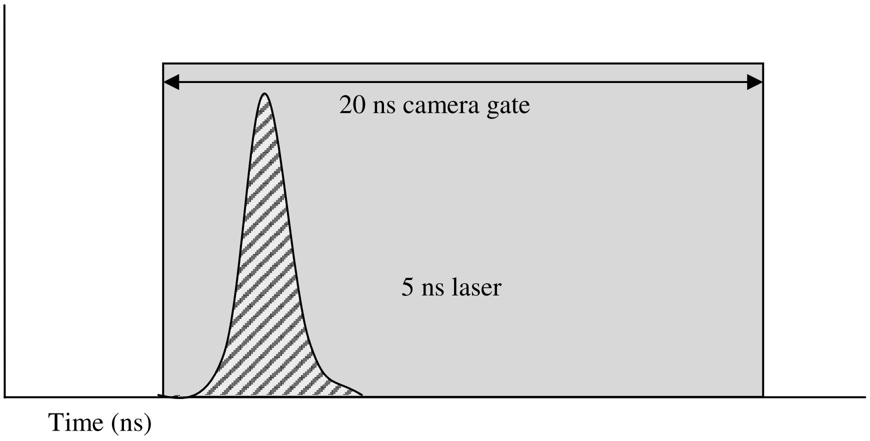

Figure 3.25 Timing diagram for Mie scattering.

The short exposure time for the camera gate can be utilized to capture the short, ~5-ns laser pulse. Further, with this short gate width, the intensity of the flame emission is not significant enough to appear strongly in the images, as a minimum of a 200 ns gate width was used for flame detection in the single shot flame images.

The flame emission is further eliminated through the use of spectral filtering. A 1-mm laser-line filter centered at 532 nm with a FWHM transmission of 0.1 nm was used to spectrally filter all wavelengths other than 532 nm, as shown in Figure 3.26. For some studies, the Mie scatter signal was so intense that a neutral density (ND) filter was used to reduce signal intensity (a ND filter attenuates light uniformly across a specified wavelength range).

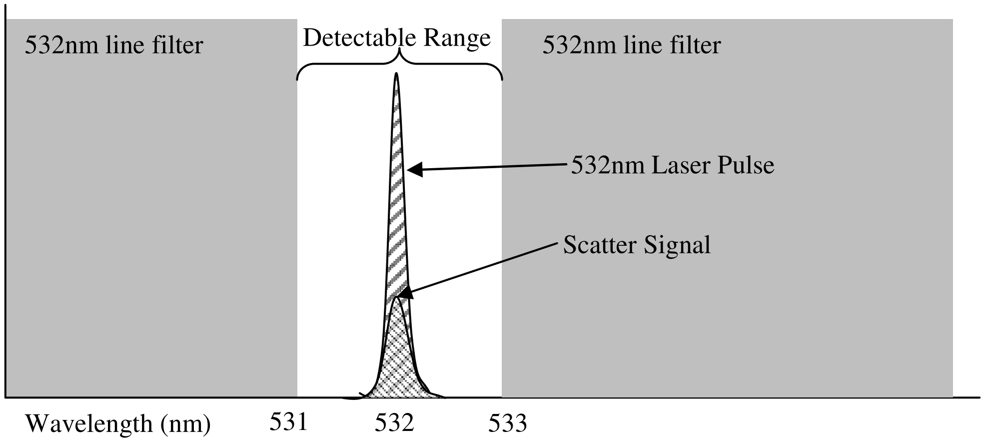

Figure 3.26 Spectral filtering diagram for Mie scattering.

The temporal and spectral filtering methods were very effective in allowing separation of flame emission from Mie scattering. However, after each measurement, a set of images was collected with the same camera settings, but at a time far delayed from the laser pulse such that the Mie scatter was no longer present. These background images serve to identify any flame emission signal which may be collected as well as any dark-current background noise in the camera.

A summary of the equipment, timing, and spectral filtering used in the Mie scattering measurements is provided in Table 3.7

Table 3.7 Equipment and settings used in Mie scattering measurements.

Variable	Value
Laser Wavelength	532 nm
Laser Power	400 – 450 mJ
Laser Sheet Size	0.5 – 1.5 m
Filters	532 line (1mm) ND (1 mm)
Lens f-stop	4.5 - 32
Gate Width	20 ns
Gate Delay	0 ns
Intensifier Gain	10 - 20

3.5.4.2 Laser-Induced Incandescence (LII)

Laser-induced incandescence (LII) utilizes a high power laser source to heat particles to a very high temperature (~3000 K), causing them to radiate as blackbodies [26, 76]. The blackbody radiation has a long signal decay time on the order of tens to hundreds of nanoseconds depending on the particle size and degree of heating. The intensity of the emitted LII signal is approximately proportional to the cube of the particle diameter, provided that it has been heated sufficiently. However, for very large particles, insufficient heating may occur such that the emitted signal strength is reduced.

Laser-induced incandescence is a useful technique for flame analysis because it can show the location of soot in flames. Soot typically has small primary particle sizes (~ 10-100 nm) such that it can be sufficiently heated by a high intensity laser beam, allowing it to strongly radiate as a blackbody more strongly than nascent soot emission. Because the individual soot particles are small, the signal emitted from a single particle is low. However, in non-premixed flames the concentration of soot particles in fuel-rich regions is generally very high, such that emission is detected from a large number of particles, generating a strong LII signal that is approximately proportional to the local soot volume fraction.

The LII signal is significantly lower in intensity than the Mie scatter signal; however, it has a long signal decay time. Therefore, the camera gate is opened after the laser pulse (~50 ns delay to avoid Mie scattering) with a long gate width (~100 ns) as shown in Figure 3.27.

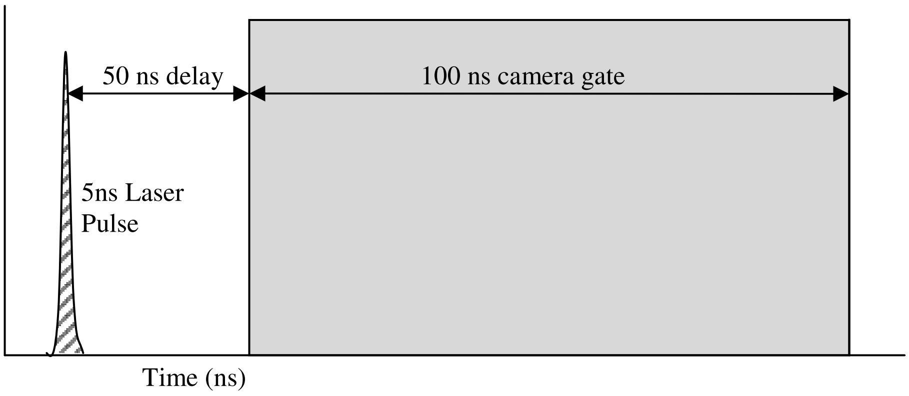

Figure 3.27 Timing diagram for LII.

Under some test conditions the flame signal intensity can be intense enough to be detected slightly with the 100 ns gate width. Therefore, spectral filtering was also employed to eliminate any flame emission. The radiation emitted from the LII signal is shifted towards the UV relative to the flame, because the blackbodies emitting the LII signal are heated to temperatures well above the flame temperature. Therefore, by allowing detection of signal occurring at wavelengths below 450 nm, the flame emission can be greatly reduced relative to the LII emission as shown in Figure 3.28. This was achieved by utilizing a 2 mm CG400 high-pass filter to block emission below 400 nm and a 2 mm band-pass filter to pass emission between 370 and 450 nm.

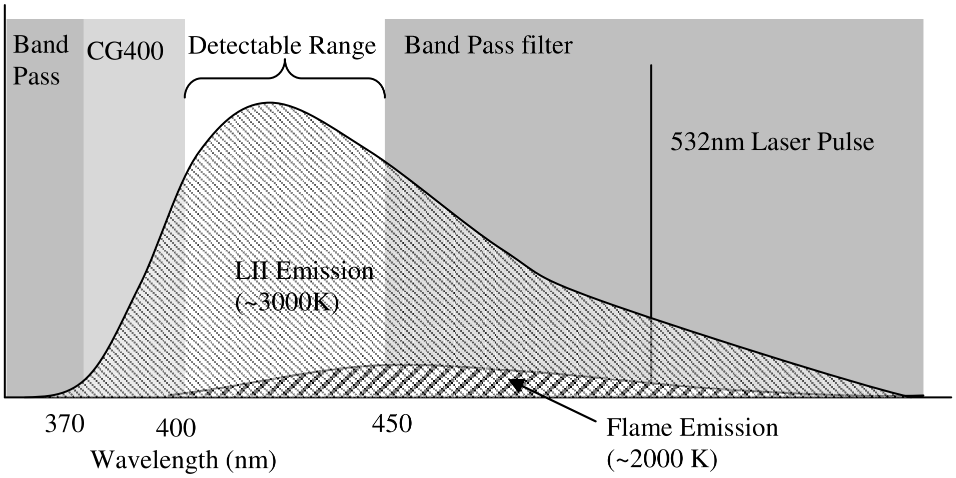

Figure 3.28 Spectral filtering diagram for LII.

The temporal and spectral filtering methods greatly limited the flame emission detected; however, images of the background flame emission for background correction were taken after each LII measurement by delaying the camera shutter far from the laser pulse.

A summary of the equipment, timing, and filtering used in the LII measurements is provided in Table 3.8.

Table 3.8 Equipment and settings used in LII measurements.

Variable	Value
Laser Wavelength	532 nm
Laser Power	400 – 900 mJ
Laser Sheet Size	0.5 m
Filters	CG400 high-pass (2 mm) Band-pass (2 mm)
Lens f-stop	1.4 – 4.5
Gate Width	100 - 200 ns
Gate Delay	50 ns
Intensifier Gain	100 - 250

3.5.4.3 UV Fuel Planar Laser-Induced Fluorescence (Fuel-PLIF)

In the UV fuel fluorescence technique, a UV laser beam is used to generate fluorescence of the fuel in both the liquid and vapor states [75]. Fluorescence is spontaneous emission of photons from higher to lower energy states after resonant absorption from a light source, in this case a UV laser. Because fuels are composed of several large, complex hydrocarbons, there are a very large number of photon generation pathways such that they have broad ranges of UV absorption and fluorescence. The signal strength of Fuel-PLIF is proportional to the fuel concentration.

The absorption spectrum for the fuels studied in the research was measured using an Agilent 8453 UV-Vis Spectrophotometer with the results shown in Figure 3.29. All of the fuels were diluted in methanol at a ratio of 1000000:1 to aid in optical transmission. The spectral absorption results are shown in Figure 3.29. As can be seen, all of the fuels absorb well in the UV.

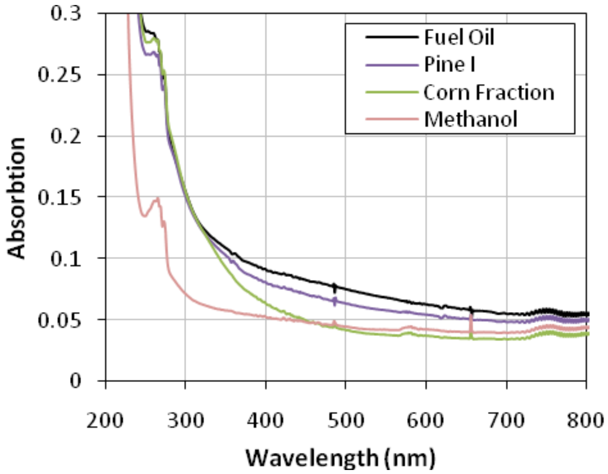

Figure 3.29 Absorption spectrum of the fuels studied.

The fluorescence emission of the fuels was measured with an Ocean Optics HR4000CG-UV-NIR spectrometer by stimulating the fuels with the same 283 nm wavelength laser that was used to perform the Fuel-PLIF studies. Once again, the pyrolysis oils were diluted with methanol to allow sufficient laser transmission through the sample cell. As shown in Figure 3.3, the methanol does not affect the fluorescence spectra of the pyrolysis oils. The fluorescence emission spectra for the fuels used in this study are shown in Figure 3.30. The emission of all of the fuels is shifted towards the visible spectrum. The corn fiber and pine derived pyrolysis oils have very similar fluorescence spectra with emission between 450 and 700 nm. The fuel oil fluoresces over a broader range and at lower wavelengths, between 300 and 650 nm.

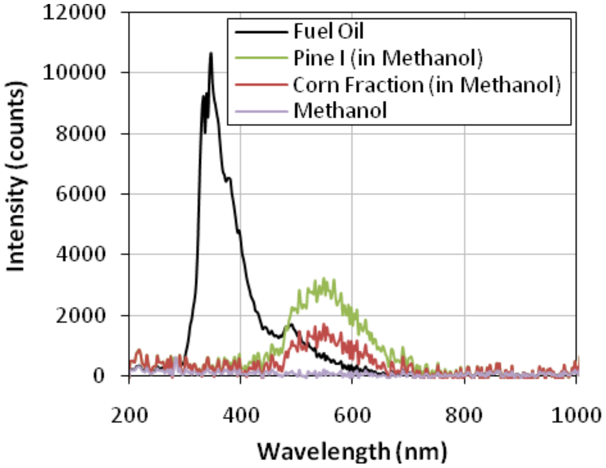

Figure 3.30 UV fuel fluorescence emission spectrum of the fuel.

Fuel fluorescence occurs in a very short time span (~10's of ns) such that the camera shutter is opened during the laser pulse as shown in Figure 3.31. A 20 ns gate width is used to limit the collection of flame radiation while ensuring that the Fuel-PLIF signal is detected regardless of slight jitter in the laser timing.

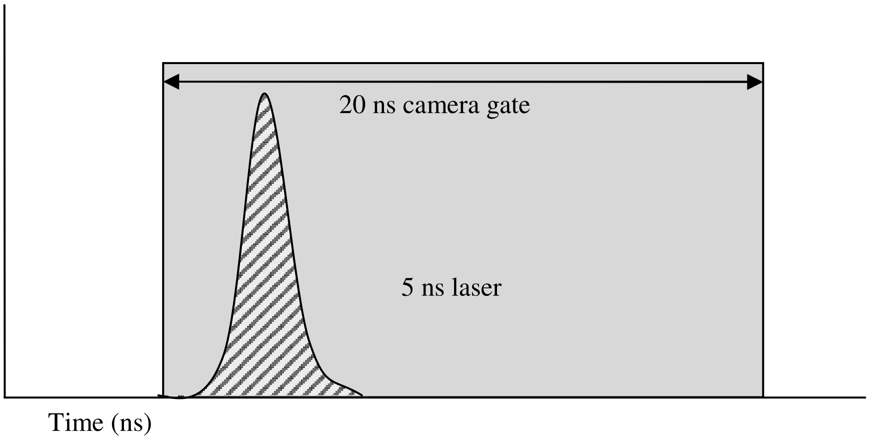

Figure 3.31 Timing diagram for UV-FF.

A laser wavelength of 283.794 nm is used to stimulate the fuel fluorescence, and is set precisely to avoid excitation of the hydroxyl radical. Because the camera gate is open during the laser pulse, Mie scatter at 283.794 nm must be spectrally filtered. Two 1-mm WG295 Schott Glass filters along with a 2-mm WG305 Schott Glass filter are used to block the Mie scatter as shown in Figure 3.32.

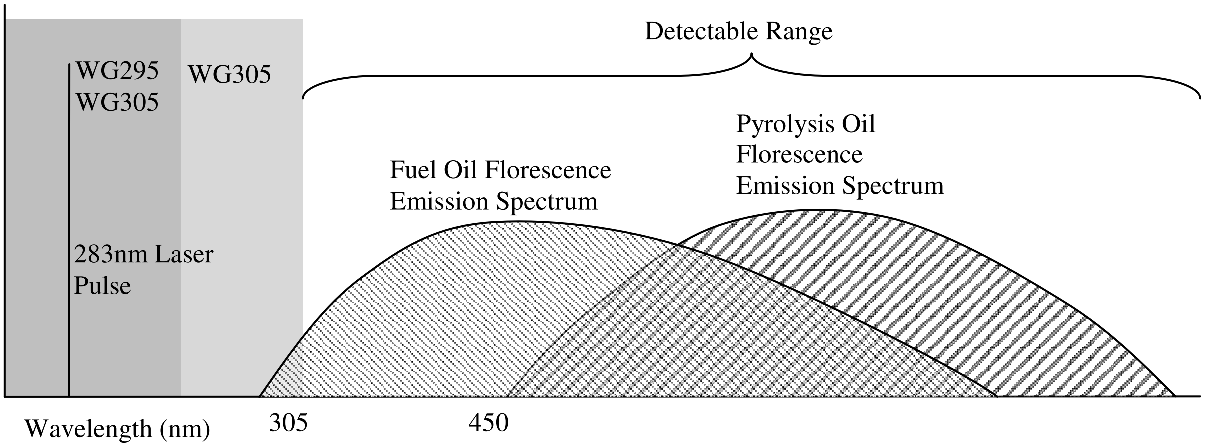

Figure 3.32 Spectral filtering diagram for Fuel-PLIF.

Although the camera gate was very short (20 ns), under certain test conditions, the flame emission was intense enough to be seen in the fuel fluorescence images. This is due to the fact that the fuel fluorescence signal was much weaker than Mie scattering. After each Fuel-PLIF measurement, a set of images of the background flame emission was taken by timing the camera shutter far from the laser pulse.

A summary of the equipment, timing, and filtering used in the Fuel-PLIF measurements is provided in Table 3.9.

Table 3.9 Equipment and settings used in Fuel-PLIF measurements.

Variable	Value
Laser Wavelength	283.794 nm
Laser Power	7 - 15 mJ
Laser Sheet Size	0.5 m
Filters	WG295 (1 mm) x2 WG305 (2 mm)
Lens f-stop	4.5
Gate Width	5 - 20 ns
Gate Delay	0 ns
Intensifier Gain	100 - 200

3.5.4.4 Hydroxyl Radical Planar Induced Fluorescence (OH-PLIF)

The OH-PLIF technique is very similar to Fuel-PLIF; however, rather than simulating fluorescence of fuel, the hydroxyl radical (OH) is stimulated at a specific transition wavelength [75]. The OH molecule is of interest in combustion studies because it is a flame intermediate species which is only stable at elevated temperatures. Therefore OH serves as a useful maker for identifying the reaction zone in the flame.

Because OH is a simple molecule, the absorption peaks are well defined. This allows for the OH-PLIF signal to be activated or deactivated by tuning the laser on or off the absorption peaks. The $Q_1(9)$ transition has been chosen (283.922 nm) because of its small variation in the ground-state rotational population with a variation of only 2.5% over the range of temperatures expected in the flame zone. Because of this temperature insensitivity, the OH-PLIF signal remains independent of the local flame temperature. Therefore, the OH-PLIF signal is directly proportional to the local OH concentration and laser energy.

The fluorescence event occurs in a very short time span (~2-3 ns) such that the camera shutter is opened during the ~5-ns laser pulse as shown in Figure 3.33. A 20 ns gate width is used to ensure that the OH-PLIF signal is detected regardless of slight drifting in the laser timing.

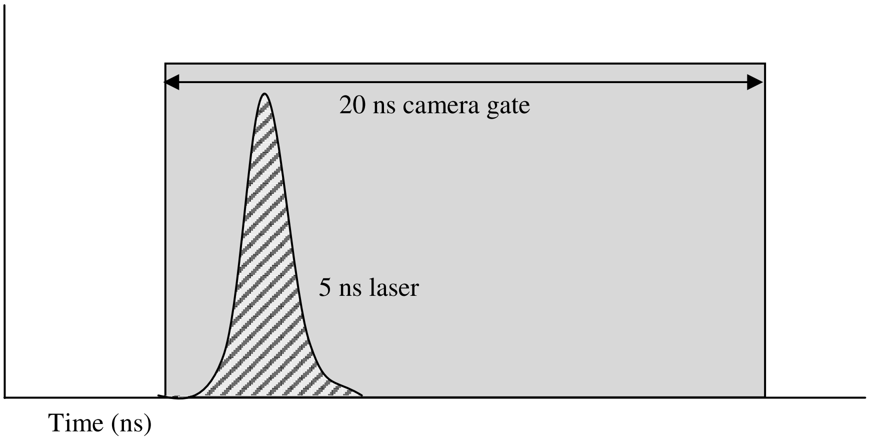

Figure 3.33 Timing diagram for OH-PLIF.

Because the camera gate is open during the laser pulse, Mie scatter at 283.922 nm must be spectrally filtered. Two 1-mm WG295 Schott Glass filters along with a 2-mm WG305 Schott Glass filter are used to block the Mie scatter as shown in Figure 3.34. Further, because 283.922 nm is sufficient to stimulate fluorescence of the fuel, two 2-mm UG11 Schott Color Glass filters were used to reduce fuel fluorescence above 400 nm.

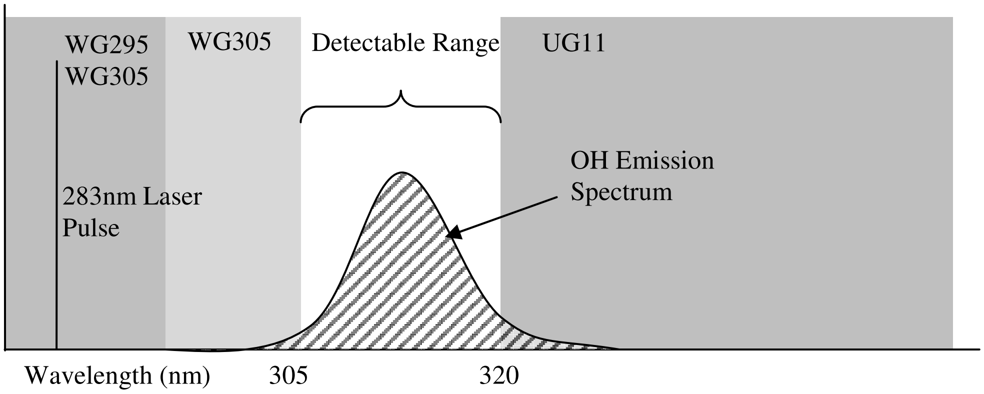

Figure 3.34 Spectral filtering diagram for OH-PLIF.

In addition to blocking the Fuel-PLIF signal, the UG11 filters served to further reduce the signal from flame emission. Although flame emission in the OH-PLIF images is very low, background flame emission images were taken after every OH-PLIF test by timing the camera shutter far from the laser pulse.

A summary of the equipment, timing, and filtering used in the OH-PLIF measurements is provided in Figure 3.10.

Table 3.10 Equipment and settings used in OH-PLIF measurements.

Variable	Value
Laser Wavelength	283.922 nm
Laser Power	7 - 15 mJ
Laser Sheet Size	0.5 m
Filters	WG295 (1 mm) x2 WG305 (2 mm) UG11 (2 mm) x2
Lens f-stop	4.5
Gate Width	5 - 20 ns
Gate Delay	0 ns
Intensifier Gain	200 - 250

3.5.5 Image Collection and Processing

For several of the visualization techniques including, single-shot flame imaging, Mie scattering, LII, Fuel-PLIF, and OH-PLIF, simultaneous measurements have been made so that direct comparisons can be made between the images. Two Princeton Scientific Instruments PI-MAX SB cameras were used to capture the simultaneous images. The cameras were spatially aligned with each other to within 1 pixel (~650 µm). Additionally, the UV and 532 nm laser sheets were overlapped with each other.

To perform simultaneous measurements which utilize different laser sheets for illumination, the measurements were taken at slightly different times to prevent the signals from interfering with one another. A time spacing of 1 µs between the laser pulses and corresponding camera gates was used. This time spacing is short enough to “freeze” the flow, with the flame moving far less than a pixel over that time period.

For all measurements with the PI-MAX SB cameras, a minimum of 50 images were collected at a rate of 2 Hz. Additionally, a minimum of 50 background images were taken after each measurement to capture the background emission from the flame.

Analysis of the images has been carried out by direct comparison of the images or by performing either a simple (ensemble) or threshold average of the set of images. For both of the averaging methods, a simple average has been performed on the background image set, and that background average has been subtracted from each image during image processing. The simple average provides a good indication of the location of the signal in the flame as well as its intensity at a particular location. However, the simple average fails to capture structures which appear intermittently in varying locations throughout the combustion chamber. Further, the simple average fails to give an accurate representation of average signal intensity in regions where the signal is not continuously present. Both of these issues can be resolved by performing a threshold average on the data set. In the threshold average, only pixels which have a value above the threshold are averaged together.

Because the choice of the threshold limit can significantly affect the outcome of the threshold average, it is necessary to develop a standard methodology for choosing this value. This is has been done by examining a log-log histogram of pixel intensity values for each set of images such. An example of one such plot for Mie Scattering data is shown in Figure 3.35. Each line in the histogram represents a different image in the image set. The trends in the histogram for a particular imaging technique have a characteristic shape. For example, the histograms for all of the Mie scattering data collected are marked by 4 trends in the curve as shown in Figure 3.35. Each region in the histogram plot with a different slope can be considered to represent a different phenomenon in the data set, with lower intensities representing background noise or other consistent interferences [77].

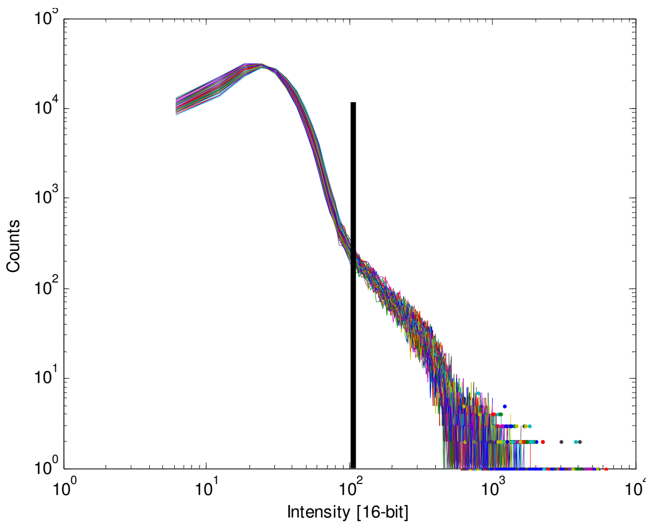

Figure 3.35 Typical pixel intensity histogram for a Mie scattering image set.

Given the repeated trends which appear in the histograms for each diagnostic technique, the threshold has been chosen by selecting a particular change in slope on the data sets, rather than by choosing an arbitrary threshold value. Moreover, under different flame conditions, the intensity at which the change in slope occurs in the histogram can vary slightly such that it is a poor choice to simply use the same threshold value across all sets of images. The characteristic change in slope which was used to determine the threshold value for the Mie scattering data is shown in Figure 3.35.

CHAPTER 4. RESULTS

4.1 Comparison of Nozzle Technologies

The flame structure and characteristics of pyrolysis oil in spray flames generated by pressure atomization differ significantly from those generated from air atomization, as shown in the color flame images in Figure 4.1 for operation at approximately 0.95 equivalence ratio and a thermal load of approximately 19 kW. The pressure-atomized flame is loosely stabilized with an outward recirculation. This recirculation is thought to be induced both by the cyclonic flow pattern induced by the air swirler and by buoyancy lifting the hot combustion gasses. In the air atomization flame, the flame is very tightly stabilized in a traditionally swirl-stabilized fashion. Given the significant differences between these flames, they have been studied in detail, independently of each other. This section will highlight some of the key differences between the flames with the discussion focused on the practical implications of the flames.

The pressure-atomized flame has a traditionally yellow flame color, indicating blackbody emission from soot produced in the flame zone. The air-atomized flame does not show this and has a much lower luminosity than the pressure-atomized flame. This is made very evident by spectrometer measurements of the flame as shown in Figure 4.2. Although the fuel flowrate (i.e. heat rate) and equivalence ratio are nearly identical for both data sets, the pressure-atomized flame shows a much greater blackbody radiation signal. The increased radiation in the pressure-atomized makes this a better candidate for radiative boiler operation, where high radiative heat transfer rates are needed. The air atomization flame, on the other hand, may make for a better candidate for use in non-radiative boilers or in a gas turbine combustor where radiative heat transfer rates can lead to losses in efficiency.

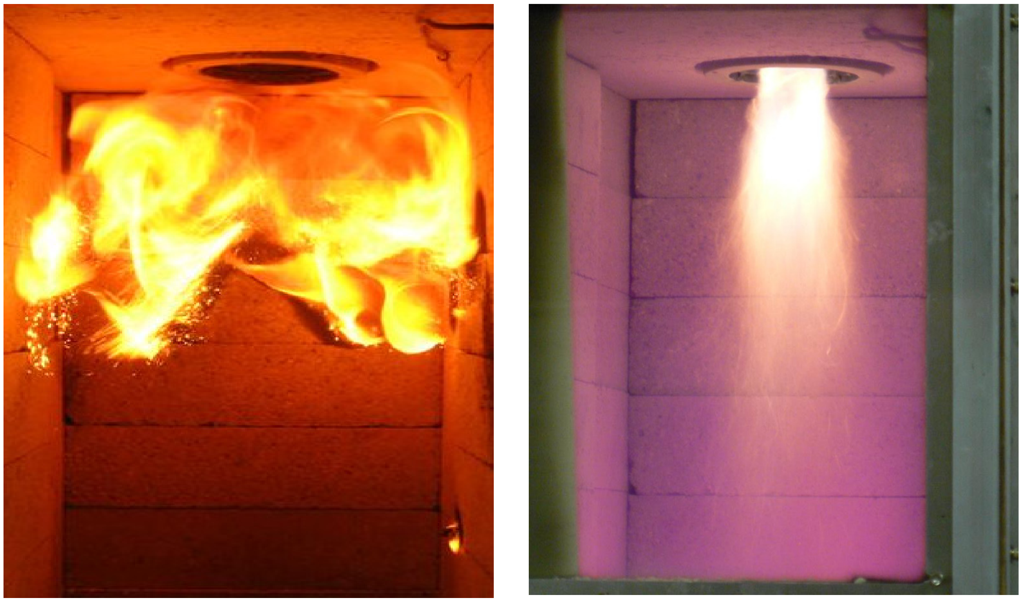
(a) **(b)**

Figure 4.1 Pine-derived pyrolysis oil spray flames generated by (a) pressure atomization and (b) air atomization at 0.75 gph.

The flame pictures in Figure 4.1 also reveal a strong purple-red color in the air atomization flame. This color is caused by the chemiluminescence of potassium in the flame at wavelengths of 766 and 769 nm ,as confirmed in the spectrometer data in Figure 4.3. It is interesting to note that both the pressure and air-atomized flames have strong potassium emission; however, for the pressure-atomized flame, this signal is much weaker than the blackbody emission such that it is not easily distinguished by eye. The spectrometer results in Figure 4.3 show two other distinct peaks. One of these is at 532 nm, corresponding to the laser light passing into the combustion chamber. The other peak at 589 nm corresponds to the chemiluminescence of sodium in the flame.

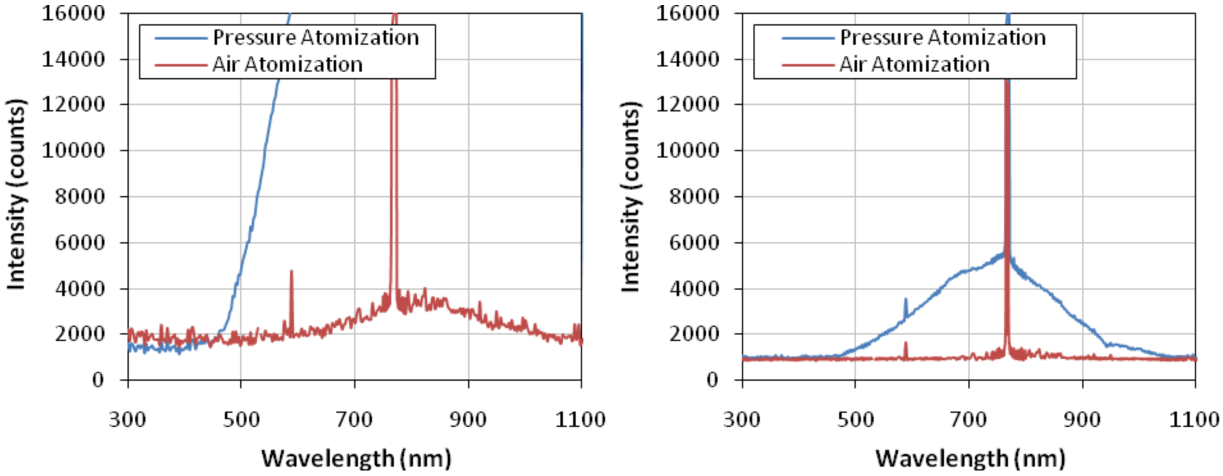

(a) **(b)**

Figure 4.2 Pine I spectrometer results for pressure and air atomization flames with data collected at 5 s (a) and 1 s (b) integration times.

With the spectrometer data, it is clear that significant amounts of alkali are released during combustion. After combustion of pyrolysis oil, the combustion chamber walls were observed to be covered with a white powder, presumably ash deposited from the oil. This phenomenon was not observed for fuel oil. These ash deposits would constitute a significant challenge for combustion in boilers and turbines because it would likely lead to slagging and corrosion problems.

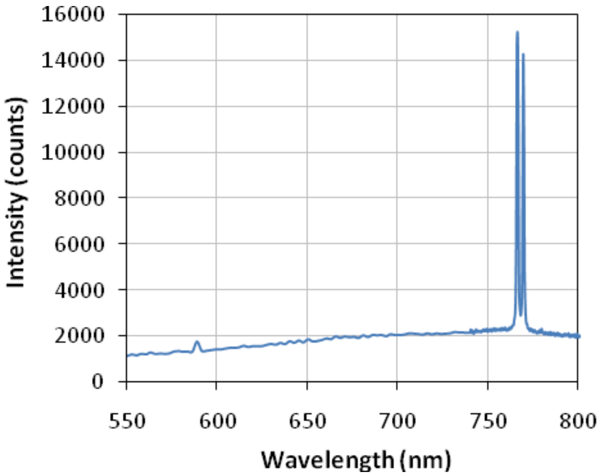

Figure 4.3 Pine I flame spectrometer measurement results with 500 ms integration time for pressure atomization.

The particulate emissions of the air-atomized flame were found to be greatly reduced in comparison to those in the pressure-atomized flame as shown in Figure 4.4. The reduction in emissions for pyrolysis oil is much more significant for pyrolysis oil than fuel oil, with the air-atomized pyrolysis oil flame having comparable emissions to the standard pressure-atomized flame of fuel oil. These characteristics will be discussed in greater detail later; however, it is relevant to note this reduction.

It is of interest to note how low the air atomization particulate emissions are in an absolute sense. The lowest particulate emissions found in the literature for pyrolysis utilization in boilers or turbines was reported by Van de Kamp et al. as a Bachrach smoke number of 2 [29, 55]. This corresponds to a value of 7 mg/m^3 when using the calibration equations for the AVL 415S smoke meter. With the air atomization studies, the particulate emissions have been reduced below this, with some conditions being zero within the measurement uncertainty. This is a marked reduction in emissions; however, it should be noted that the combustor used in this research does not quench the flame intentionally as is done in boilers and/or turbines by heat or work transfer from the combustor. The energy extraction which is present in these applications may be a factor in increasing particulate emissions.

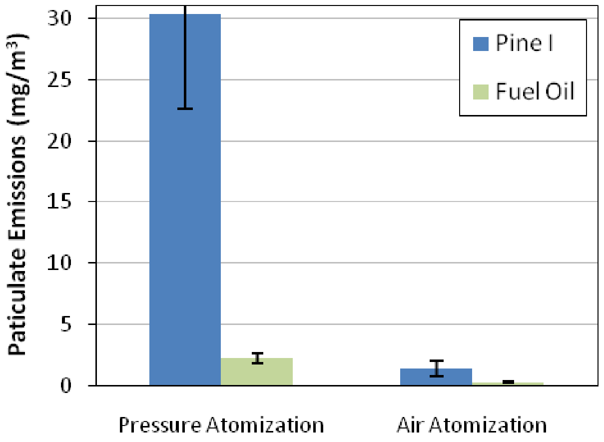

Figure 4.4 Particulate emissions of Pine I and Fuel oil from pressure and air atomization flames operating at 18 kW and 0.95 equivalence ratio.

Aside from particulate measured in the exhaust, unburned fuel residues were found to collect on the walls and bottom of the combustion chamber for pyrolysis oil combustion. This phenomenon was found to be much more significant for the pressure-atomized case than the air-atomized case. The image of the pressure-atomized flame in Figure 4.1 shows such a collection of fuel residue along the lower right section of the combustion chamber wall. These fuel residues would eventually burn out along the wall or chamber bottom. The level of fuel residue collection on burner surfaces found in the pressure-atomized case may be problematic for operation of boilers or turbines.

The flame stabilization limits for flames with both nozzle types were found to be quite narrow in comparison to the flammability limits for light fuel oil. Ignition was very challenging for both nozzle types and all pyrolysis oils tested. To achieve stable ignition, strong swirl, high combustion air temperature preheat, and high fuel temperature preheat were required.

Nozzle and filter clogging were a constant challenge for both nozzle types. For pressure atomization, 40 micron filters were used to filter the fuel prior to reaching the nozzle; however, these filters would clog within a few hours. Attempts at operating the pressure atomization nozzles with coarse filtration caused clogging/coking of the nozzles within an even shorter time period. Pyrolysis oil was only coarsely filtered (140 micron) for air atomization tests, since the fuel passages were larger. However, clogging/coking was still a challenge for these nozzles as well.

4.2 Pressure Atomization Studies

A limited number of studies were performed with the pressure-atomized flames given the poor quality of the flame stabilization. Three different fuels (Fuel Oil, Emulsion, and Pine I) were studied at an equivalence ratio of 0.95. The Pine I oil was also studied at an equivalence ratio of 0.70. For this set of data two PI-MAX SB cameras were available such that simultaneous flame visualization measurements could be made.

4.2.1 Comparative Fuel Studies

Three different fuels (Fuel Oil, Emulsion, and Pine I) were studied at an equivalence ratio of 0.95. A Delevan Type A 0.75 gph nozzle was used and operated at the standard 100 psi delivery pressure for all three fuels. The goal of this particular study was to determine how pyrolysis oil would behave under nozzle conditions which were as similar to the original burner operating parameters as possible. However, the modified air swirler was used, and fuel and combustion air preheating were employed for the Pine I fuel.

Neither the fuel oil nor the emulsion were intentionally heated prior to reaching the nozzle; however, heat transfer from the chamber increased the fuel temperature to 50 °C for both fuels. Similarly, the combustion air was not intentionally preheated for the fuel oil and emulsion studies; however, heat transfer from the chamber increased the incoming combustion air temperature to 130 °C. For the Pine I oil, the fuel was preheated to 85 °C to decrease the fuel viscosity as much as possible, and the combustion air was preheated to 300 °C, making the adiabatic flame temperature very comparable to that of the fuel oil and, thereby, improving flame stability. With the Pine I oil viscosity substantially reduced through the preheating of the fuel, the fuel flowrate was very close to the design flowrate of the nozzle. All three fuels operated within 0.02 gph of the 0.75 gph nozzle design fuel flowrate.

Images of the Pine I, Emulsion, and Fuel Oil pressure-atomized flames are shown in Figure 4.5. The Pine I flame is not stabilized by the air swirler alone as has been discussed. However, the Emulsion and Fuel Oil flames are both swirl stabilized. All flames have strong yellow color, indicative of blackbody radiation of soot in the flame.

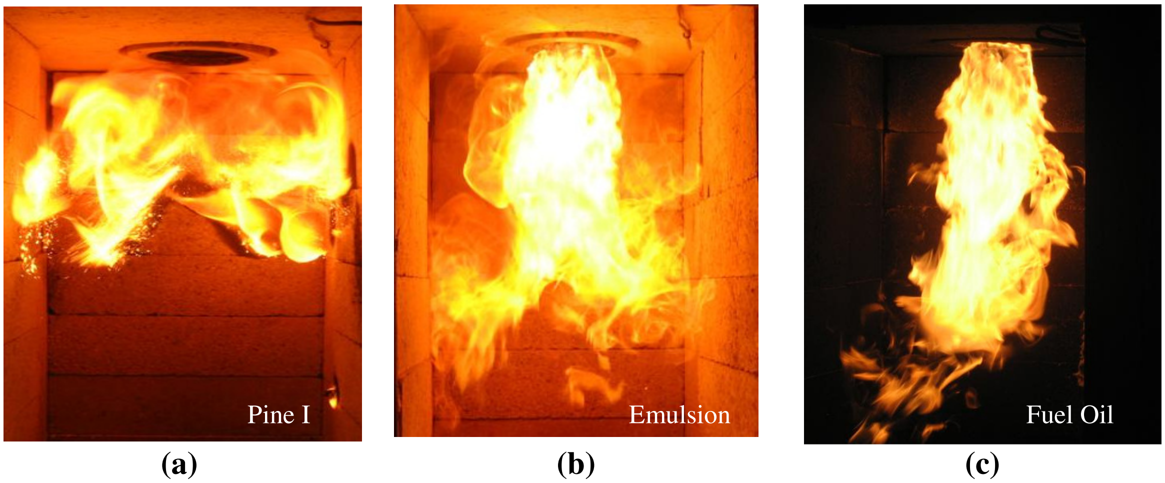

Figure 4.5 Pressure atomized flames at 0.95 equivalence ratio for Pine I (a), Emulsion (b), and Fuel Oil (c) fuels.

The intensity of the radiative flame emission increases dramatically from Pine I oil to Fuel Oil as shown in the spectrometer data in Figure 4.6. The radiative emission from the Fuel Oil flame is so intense that the detector is saturated for an integration time of 500 ms. The difference between the two fuels is partially the result of a difference in energy output, since the fuel oil has nearly twice the volumetric energy as the pyrolysis oil and both are operated at the same volumetric flowrate. However, the difference in energy content alone likely does not account for this significant difference, and is likely somewhat an indication of the characteristics of pyrolysis oil relative to fuel oil. The low radiative emission of the pyrolysis oil in comparison to fuel oil may reduce its usefulness as a fuel for radiative boilers.

The particulate emissions from the pressure-atomized flames are shown in Figure 4.7. A fairly significant reduction of PM is found in transitioning from pure Pine I oil to pure Fuel oil. This trend agrees with most of the trends in the literature which show PM emissions of pyrolysis oil to be higher than those of fuel oil.

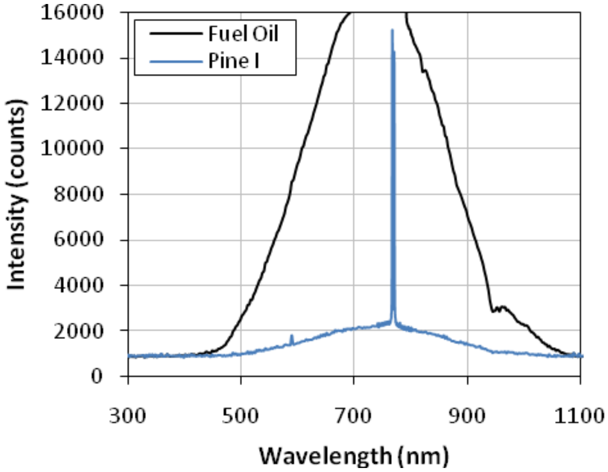

Figure 4.6 Spectrometer results of flame emission for pressure-atomized flames of Pine I oil and Fuel Oil with 500 ms integration time used during collection.

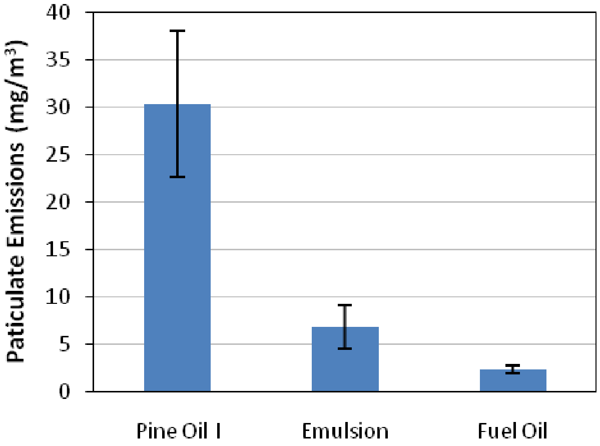

Figure 4.7 Particulate emissions from pressure-atomized flames at 0.95 equivalence ratio for Pine I, Emulsion, and Fuel Oil.

To date, no research has been performed which explains the observed increase in particulate emissions in pyrolysis oils. Scanning electron microscope images of the particulate samples have been examined to reveal the structure and composition of the particulate. Representative SEM images of PM collected from Pine I and Emulsion pressure atomization tests are shown in Figure 4.8. Both the Pine I and Emulsion particulate images show branched structures typical of soot (as discussed in Section 3.4). In the Pine I image several large structures are evident, which appear as agglomerates of much larger particles. These structures are not characteristic of soot and are likely either fuel residues or ash.

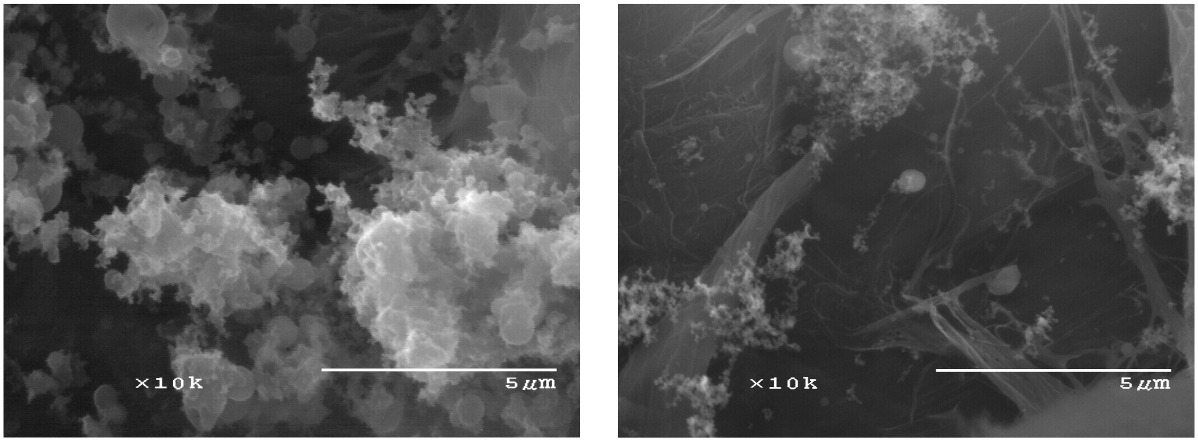

(a) **(b)**

Figure 4.8 SEM images of particulate collected for (a) Pine I Oil and (b) Emulsion.

Dispersive energy X-ray analysis of the larger structures in the Pine I PM sample has been performed to determine their elemental composition. These results are shown in Figure 4.9. The gold appearing in the sample is from the sputter coating used on the samples to improve the resolution in the SEM measurements. A small amount of aluminum is found in residues, which is likely the remains of the relatively high aluminum content found in the parent fuel. The remaining composition of the samples appears to be largely organic, indicating that these structures are fuel remains, and not ash deposits.

With it proven that these structures are fuel remains, it is of interest to know whether they are the remains of solid char present in the oil or cenospheres as found in the droplet combustion studies. Solid char produced in the production of fast pyrolysis oil typically appears as a porous structure, similar in shape to the original biomass particles [78]. As such, given that morphology of these fuel residues closely resembles that of cenospheres, not pyrolysis char, these structures are likely to be cenospheres and will be referred to as such throughout this work. However, detailed analysis of the internal structure of these fuel residues would help to verify this conclusion.

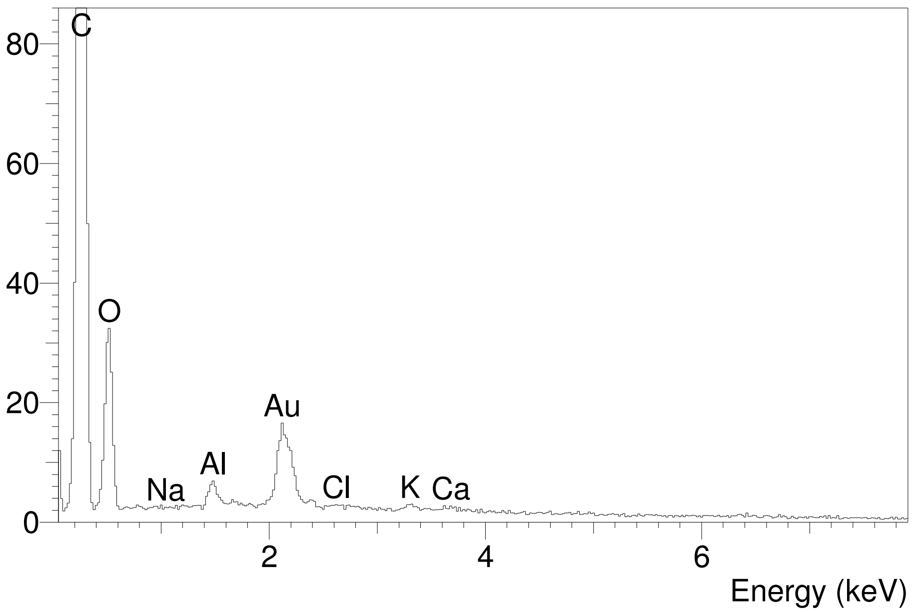

Figure 4.9 Dispersive energy X-ray analysis of PM from Pine I oil combustion.

It is important to note that although these structures are much larger than soot particles, many of the censopheres are smaller than 2.5 microns. As such, emission of these particulate would still be subject to strict regulatory guidelines.

The SEM image of the emulsion particulate shows significantly less PM than the Pine I oil sample as would be expected given the particulate readings (although this may be coincidental given that these are both very small regions of the filter paper sample). The emulsion PM is predominately soot; however, some cenospheres can be seen. The reduction of cenospheres seems likely because of the 30:70 mixture of Pine I and fuel oil; however, it is noteworthy that cenospheres are still produced and emitted from the emulsified flame. This may suggest that the chemical composition of the pyrolysis oil may still have an effect at lower concentrations or that the emulsion is poor such that strong mixing of the fuels was not achieved at the molecular scale.

It was not possible to acquire SEM images of the fuel oil particulate for conditions at or below stoichiometric because its soot reading was below 5 mg/m^3 (discussed in Section 3.4). As such, its structure cannot be determined from SEM images. However, given the low ash content in fuel oil and the lack of tendency for light fuel oil to emit stack solids, the particulate produced in the fuel oil flame is very likely soot rather than fuel residues.

Another indicator which can be used for determining whether the particulate is predominately soot or cenospheres is the color of the filter paper sample. Representative filter paper samples which have predominately soot or censopheres are shown in Figure 4.10. Samples which contain mostly soot have a grayish/black color while those with cenospheres have a brownish color. This trend in color versus particulate type has been consistent for every sample in which SEM measurements were taken. Therefore, the color of the filter paper has also been used as a method for discerning the type of PM present in the filter paper.

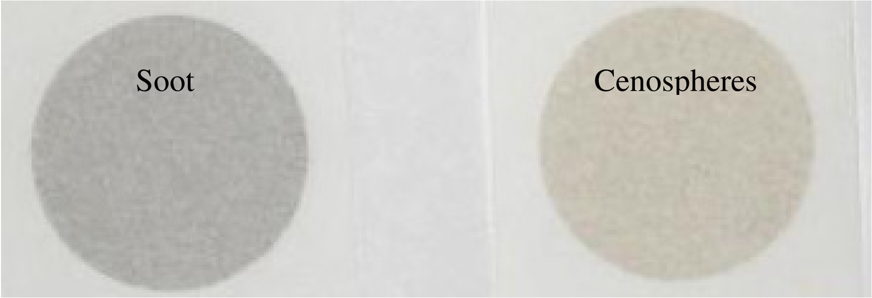

Figure 4.10 Representative filter paper samples of showing the gray/black color of soot dominated samples versus the brown color of cenosphere samples.

Although the particulate loading in the Fuel Oil PM sample was too low to allow it to be analyzed through SEM, the color of the filter paper appeared to be a faint gray color, indicating the particulate as soot. With this, it appears that the trend in reduction of particulate from Pine I to Emulsion to Fuel Oil appears to be a reduction of cenosphere emissions, not soot. Therefore, the cause of elevated PM emissions in pyrolysis oil in comparison to fuel oil is a result of emission of unburned fuel residues, not traditional soot. With this characteristic identified, it is possible to begin developing technologies which reduce these emissions.

4.2.1.1 Structure of Fuel Oil Flame with Pressure Atomization

To better understand the causes of particulate emissions, several visualization techniques including Mie Scattering, Fuel-PLIF, OH-PLIF, and flame luminosity imaging were employed, allowing for a greater understanding of the flame structure. The pressure-atomized flame will be discussed first to provide a depiction of a typical hydrocarbon flame. This will be followed by the Pine I pressure-atomized flame to highlight the many unique characteristics of the pyrolysis oil flame.

Simultaneous Mie scattering and LII images of the pressure-atomized fuel oil flame at 0.95 equivalence ratio are shown in Figure 4.11. These images are presented in false color to show the contrast between high and low intensity regions. Corresponding images of the flame background have been displayed in Figure 4.11, to show that the images have been scaled such that no background flame emission is visible in the Mie scattering or LII images. The Mie scattering image shows only solid or liquid phase objects (e.g. droplets, soot) while the LII image shows only blackbodies which are capable of being heated sufficiently by the laser (e.g., soot). For all of the laser diagnostic techniques, the signal on the right side of each image will typically be stronger than that on the left side of the image due to laser attenuation as it passes through the flame zone. The high intensity outline along the top and sides of the Mie scattering images are the result of laser scattering off the swirler plate and combustor walls.

The simultaneous Mie scattering and LII images displayed in Figure 4.11 show very good overlap in the lower and outer regions of the flame. The LII method is tailored to detect soot in the flame, while the scatter detects any solid or liquid particles. Therefore, the overlap in these regions corresponds to soot in the flame.

The remaining Mie scattering signal found in the top-center part of the flame is most likely the result of scatter off of the dense fuel spray. The droplets do not appear in the LII image because they do not behave as a black body.

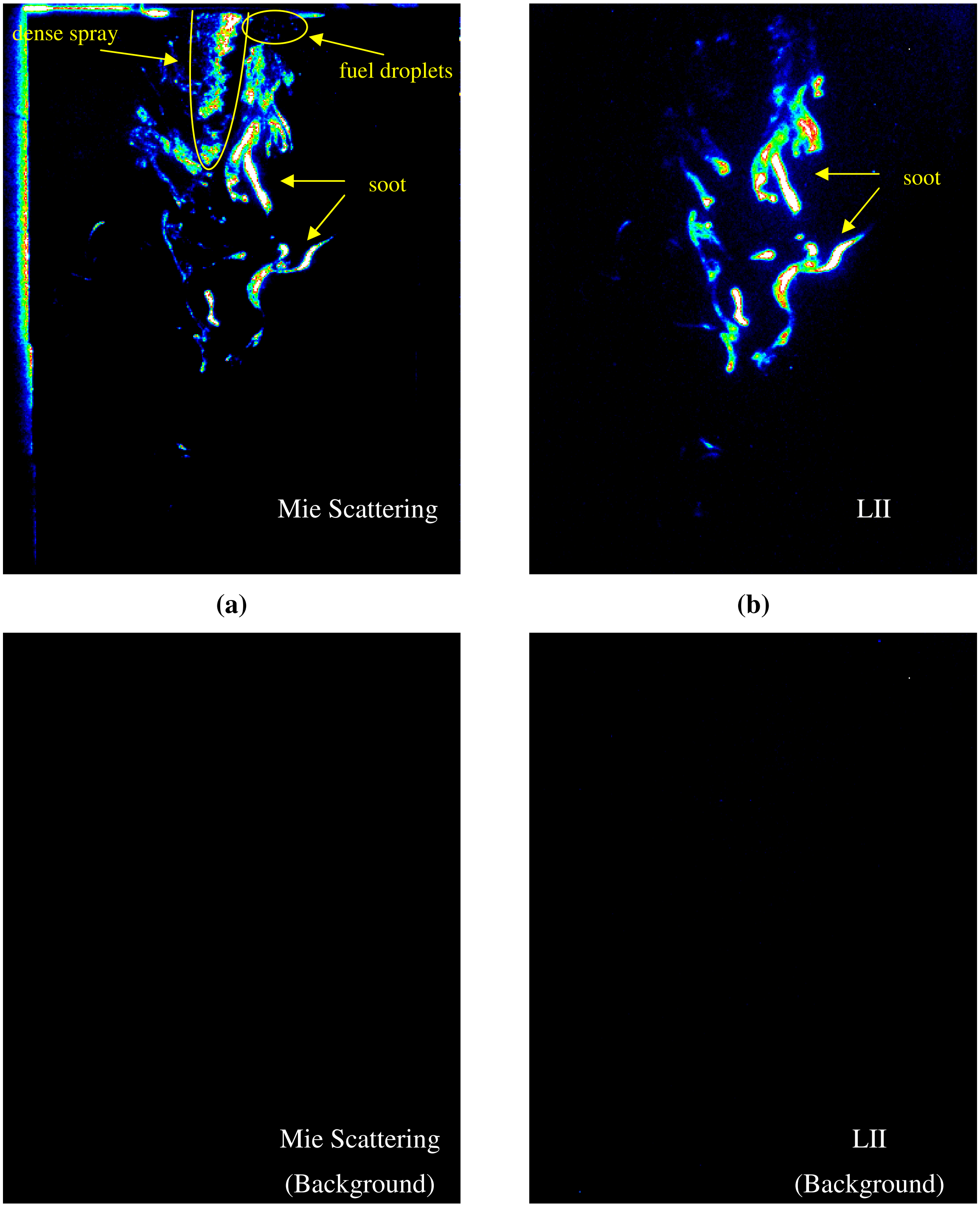

(a) **(b)**

(c) **(d)**

Figure 4.11 Simultaneous Mie scattering (a) and LII (b) images with corresponding Mie scattering background (c) and LII background (d) images of fuel oil combustion with pressure atomization at 0.95 equivalence ratio.

The Mie scattering image also reveals some larger, single, high intensity structures at the top of the chamber. These have very low signal, and exist only in the region very close to the burner exit. Given these characteristics, these are most likely large fuel droplets on the outer edge of the spray.

With regard to the Mie scattering signal in the center of the flame, further evidence that this is indeed fuel spray can be found by comparing simultaneous Mie Scattering and Fuel-PLIF images as shown in Figure 4.12. Because the UV laser energy was only 6 mJ for these Fuel-PLIF measurements, the Fuel-PLIF signal is very low such that it is difficult to scale the images so that the background flame emission cannot be seen. However, some high intensity regions in the Fuel-PLIF data can be discerned, and these correlate very well with structures in the Mie scattering image. The only regions visible in the Fuel-PLIF image are those in the dense spray region. Unfortunately, fuel vapor regions and/or single large fuel droplets cannot be detected in the Fuel-PLIF image. However, given the structure, signal intensity, and spatial distribution of the individual intensity regions in the Mie scattering image, these are very likely large fuel droplets as has been discussed above.

The dark regions between the dense fuel spray and soot regions found in the Mie scattering images are most likely fuel vapor rich regions. Soot is formed in nonpremixed flames in fuel vapor rich regions at elevated temperatures. Directly adjacent to the dense fuel spray, the fuel vapor mixture is likely still cool, having just evaporated. However, further from the spray core, temperatures increase to the point at which soot formation occurs.

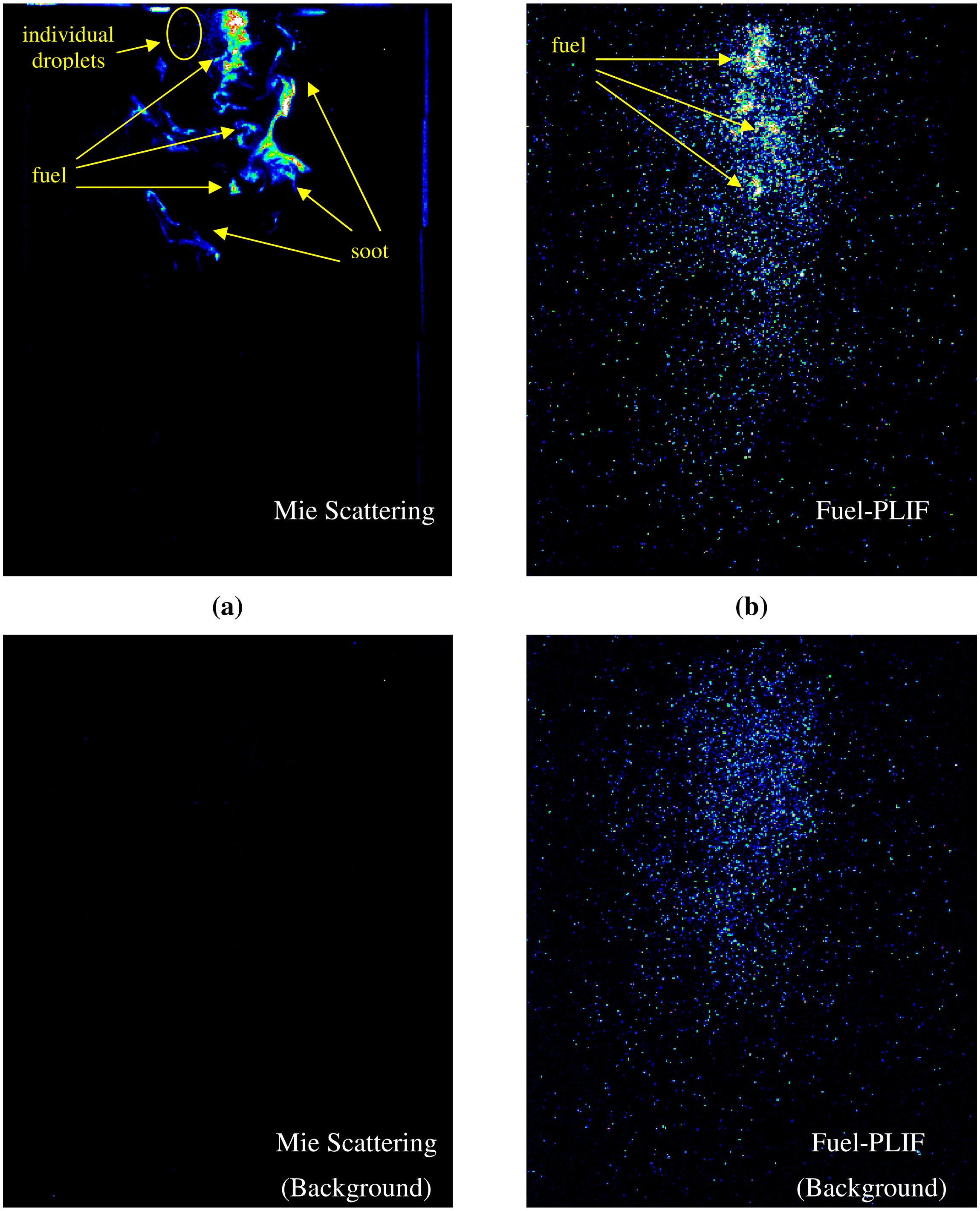

(a) **(b)**

(c) **(d)**

Figure 4.12 Simultaneous Mie scattering (a) and Fuel-PLIF (b) images with corresponding Mie scattering background (c) and Fuel PLIF background (d) images of fuel oil combustion with pressure atomization at 0.95 equivalence ratio.

As has been discussed above, soot radiation in the flame is what accounts for the most significant portion of the flame luminosity in all of the pressure-atomized flames studied. By comparing Mie scattering and flame luminosity images, a correlation can be seen between the images in regard to the visible flame front as shown in Figure 4.13. Thus, with the Mie scattering image, the fuel spray, soot, and visible flame edge can be discerned.

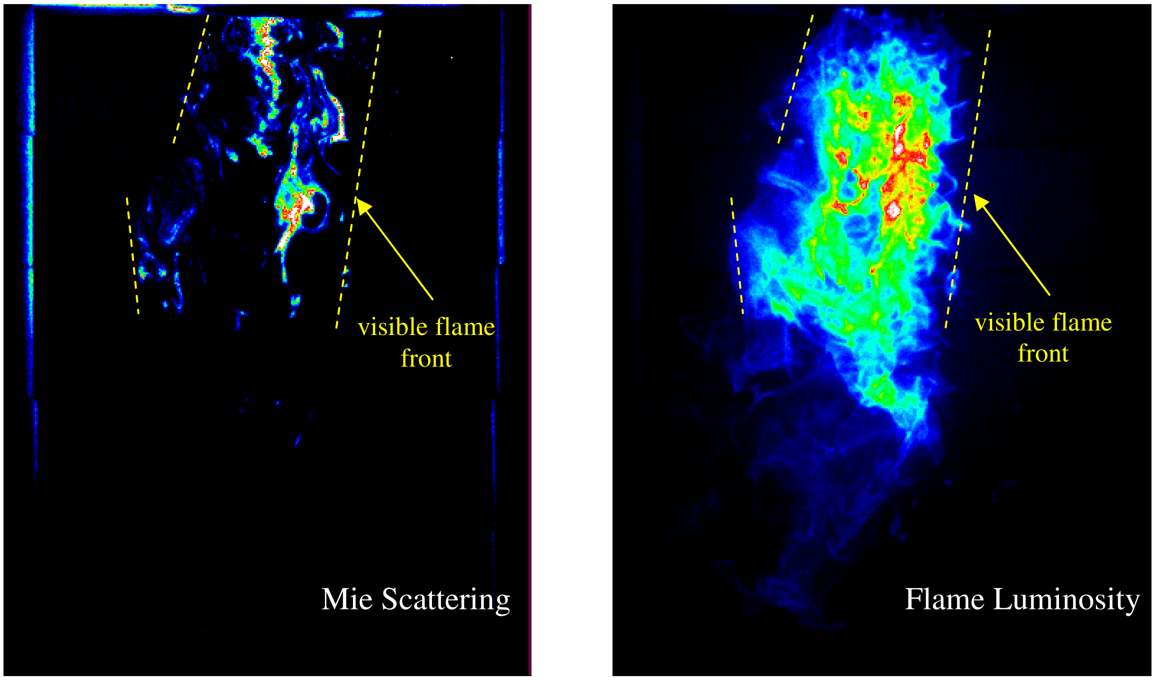

(a) **(b)**

Figure 4.13 Simultaneous Mie scattering (a) and Flame Luminosity (b) images of fuel oil combustion with pressure atomization at 0.95 equivalence ratio.

The hydroxyl radical serves as a chemical marker of the flame zone because it is a combustion reaction intermediate that only exists at temperatures high enough to support combustion reactions. Because the UV laser power was only 6 mJ for these tests, the OH signal detected was very low, such that it cannot be detected beyond the flame background in a single image. This was further compounded by the fact that the flame radiation was very strong in the pressure-atomized fuel oil flame. Because of this, an image which represents the simple average of the OH-PLIF data has been produced as shown in Figure 4.14. An average of the flame background has been subtracted from the average image, such that no flame emission is present in the averaged signal.

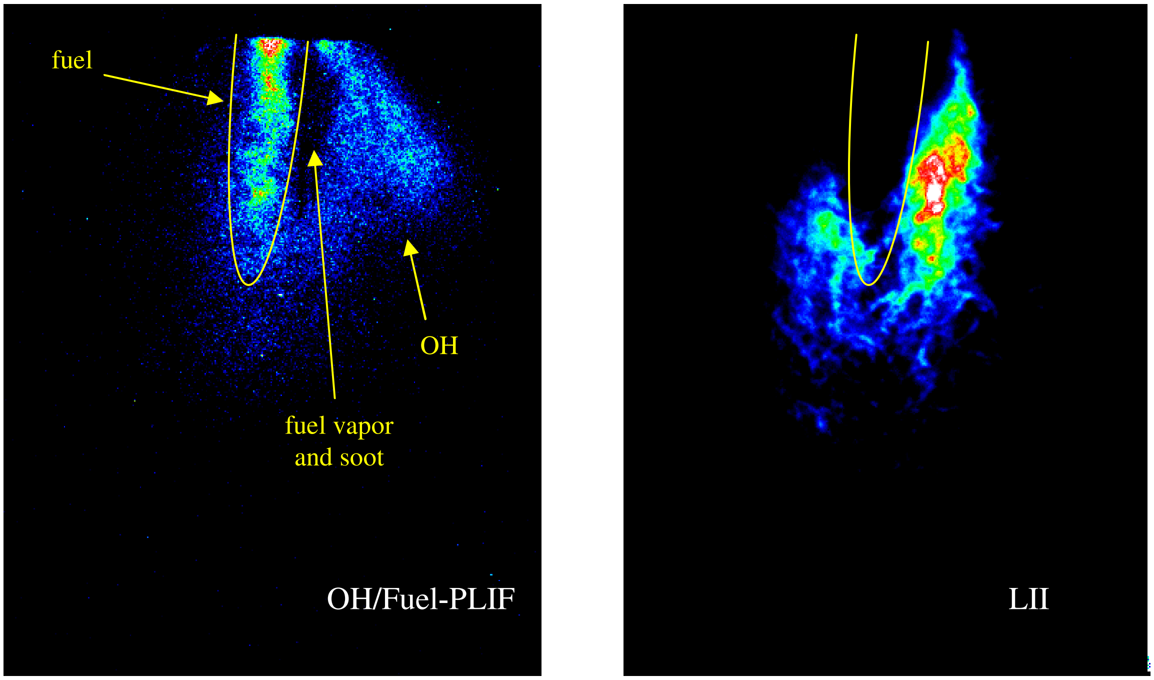

(a) **(b)**

Figure 4.14 Simple average of OH-PLIF (a) and LII (b) images of fuel oil combustion with pressure atomization at 0.95 equivalence ratio.

The OH-PLIF technique also captures some fuel fluorescence for the fuel oil measurements, because fuel oil fluoresces over the range of OH detection as shown in Figure 3.30, Figure 3.32, and Figure 3.34. Given this, the fuel fluorescence cannot be spectrally filtered to allow for differentiation between the OH and fuel fluorescence. Therefore, the OH-PLIF image is actually showing both OH and fuel such that it is referred to as OH/Fuel-PLIF. Given the location of fuel fluorescence in the center of the flame as shown in Figure

4.12, the only region of the OH/Fuel-PLIF which can be uniquely attributed to be OH is that towards the outer edges of the flame.

The dark region which appears in the OH/Fuel-PLIF image likely contains fuel vapor and soot. This is highlighted by comparing the OH/Fuel-PLIF simple average image to a simple average image of the LII as shown in Figure 4.14. The LII image shows that soot exists beyond the spray region, partially overlapping the fuel vapor region on average. On average, the OH exists throughout the soot region and beyond it. At a single instant in time, the OH and soot do not likely overlap; however, because the flame is highly turbulent, an averaging of the soot and OH images reveals some overlap in their regions [76].

The simple average images of the OH and LII show that the main flame reaction zone is far away from the dense fuel spray and is marked by high soot levels. Further, the overlap in the OH and soot regions, and the fact that the OH region reaches beyond the soot region, reveals that there is ample OH present in the flame to oxidize the soot. This availability of OH is what allows for the very low soot measurements in the exhaust, despite the high soot concentrations in the flame.

4.2.1.2 Structure of Pine I Flame with Pressure Atomization

The Pine I oil pressure-atomized flame looks far different than the fuel oil flame as shown in Figure 4.5. In addition to the air swirl, the flame appears to be stabilized through an outward recirculation caused by buoyancy.

The difference between the Fuel Oil and Pine I flames is made even more apparent by examining simultaneous images of Mie scattering and Fuel-PLIF as shown in Figure 4.15.

Because the flame emission signal is much lower than for the fuel oil flame, it does not interfere with the Fuel-PLIF signal and does not appear in the image of Figure 4.15(b).

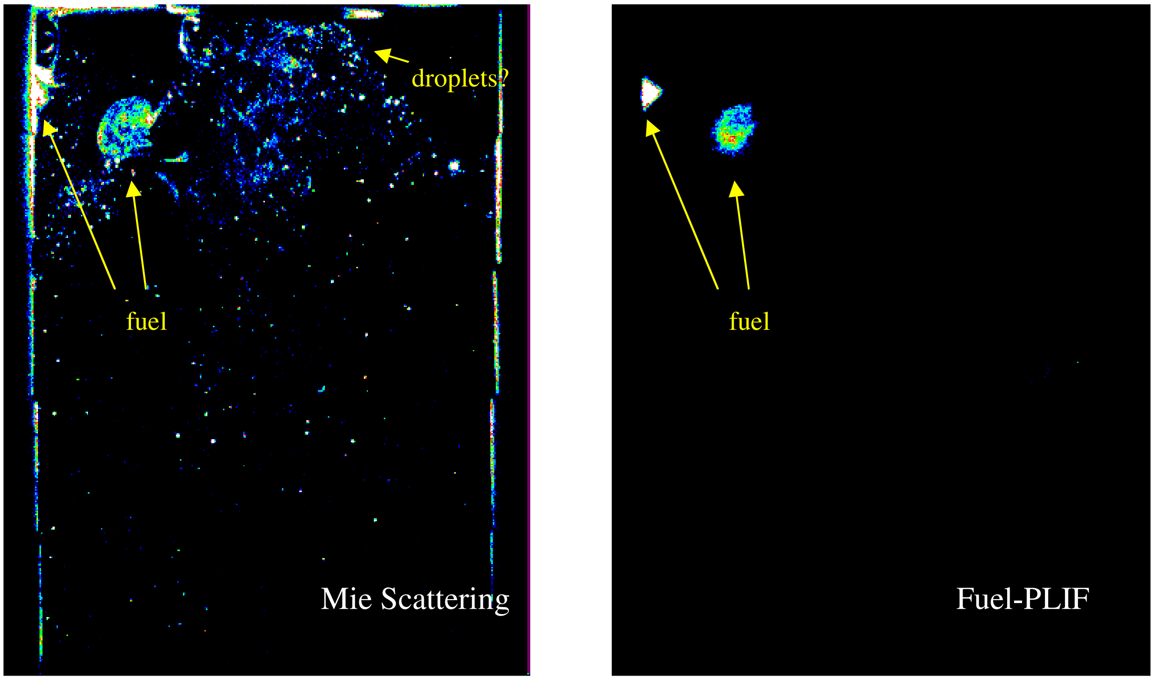

(a) **(b)**

Figure 4.15 Simultaneous Mie Scattering (a) and Fuel-PLIF (b) images with Pine I fuel combustion with pressure atomization at 0.95 equivalence ratio.

The Pine I oil flame does not show a dense spray core as seen in the Fuel Oil flame, either in the Mie Scattering or Fuel-PLIF data. The only regions of fuel which can be identified in the Fuel-PLIF image occur on the upper, outer edge of the flame. The scatter shows significant signal levels throughout a wide region at the top of the chamber. It appears that this may be scattering from the fuel spray; however, this is not corroborated in the Fuel-PLIF data.

The scatter also shows several individual high intensity signals at the top of the chamber, on what would appear to be the outer edge of the spray. Some droplets were observed in this region in the fuel oil flame; however, there are significantly more of these particles observed in the pyrolysis oil flame. Further, some of these structures are very large, illuminating several pixels, such that it seems very unlikely that the spray would produce fuel droplets which are that large. Additionally, in comparison to the fuel oil flame, these particles do not disappear towards the end of the spray (i.e. they vaporize).

Given this evidence, it seems possible that these particles may not be simply fuel droplets alone, but rather, they may consist of cenospheres as well. Research performed in droplet studies of pyrolysis oils have shown that the cenospheres have longer burning rates, such that they would have a longer residence time in the combustion chamber [63-67]. Further, these studies have shown that the cenospheres can double in size in comparison to the original droplet diameter. The discussion of the possibility of these objects being cenospheres will be taken up in greater detail after discussing soot in the flame.

An examination of simultaneous Mie Scattering and LII images reveals the location of soot structures in the flame as shown in Figure 4.16. Once again, the flame background is very low such that it is not shown in the images in Figure 4.16. Soot structures are evident both in the LII and Mie Scattering images. The soot seems to appear in lower regions of the flame. There are some other large scattering regions in the Mie Scattering image towards the top of the chamber which have similar location and structure as the fuel seen in the Fuel-PLIF images. As such, these are most likely regions of fuel droplets.

In addition to the fuel droplets and soot, several individual high intensity points are observed in the Mie Scattering images, which are not seen in either the LII or Fuel-PLIF images. These points are not seen in the fuel oil flame, such that they are unique to pyrolysis oil. These points could be scattering from fuel droplets; however, some of the signals appear to be far too large to simply be fuel droplets. Further, it seems very unlikely that a liquid fuel droplet could survive the high flame temperatures for long enough to exist near the bottom of the combustion chamber.

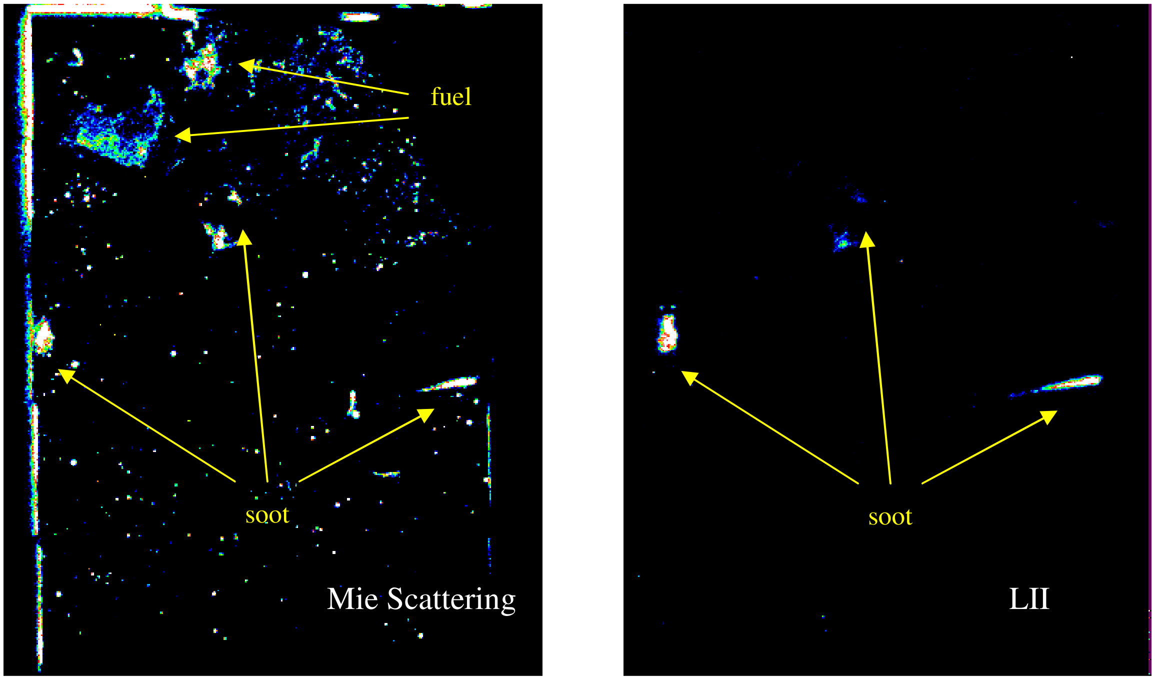

(a) **(b)**

Figure 4.16 Simultaneous Mie Scattering (a) and LII (b) images with Pine I fuel combustion with pressure atomization at 0.95 equivalence ratio.

To further investigate whether these particles are fuel droplets, Mie Scattering images of a cold fuel spray have been collected for both Pine I and Fuel Oil as shown in Figure 4.17. In both images the chamber is filled with fuel mist. The spray distribution of the Pine I fuel is widely distributed, without a strong central core, which agrees with the observations seen in the Pine I fuel flame.

Neither of the cold spray images in Figure 4.17 shows individual high intensity points. Instead, the images show a distributed *cloud* of fuel droplets which are much smaller than the pixel size. The big droplets near the core of the spray may be obscured by the intense signal and diffuse light scattering near the core. However, near the bottom of the chamber, the signal from the fine fuel mist is much lower such that if there were individual high intensity signals, they would certainly be detectable. As such, it appears that the large individual particles observed in the Pine I oil flame are formed during combustion and are not simply fuel droplets. This provides further evidence suggesting that these particles are cenospheres.

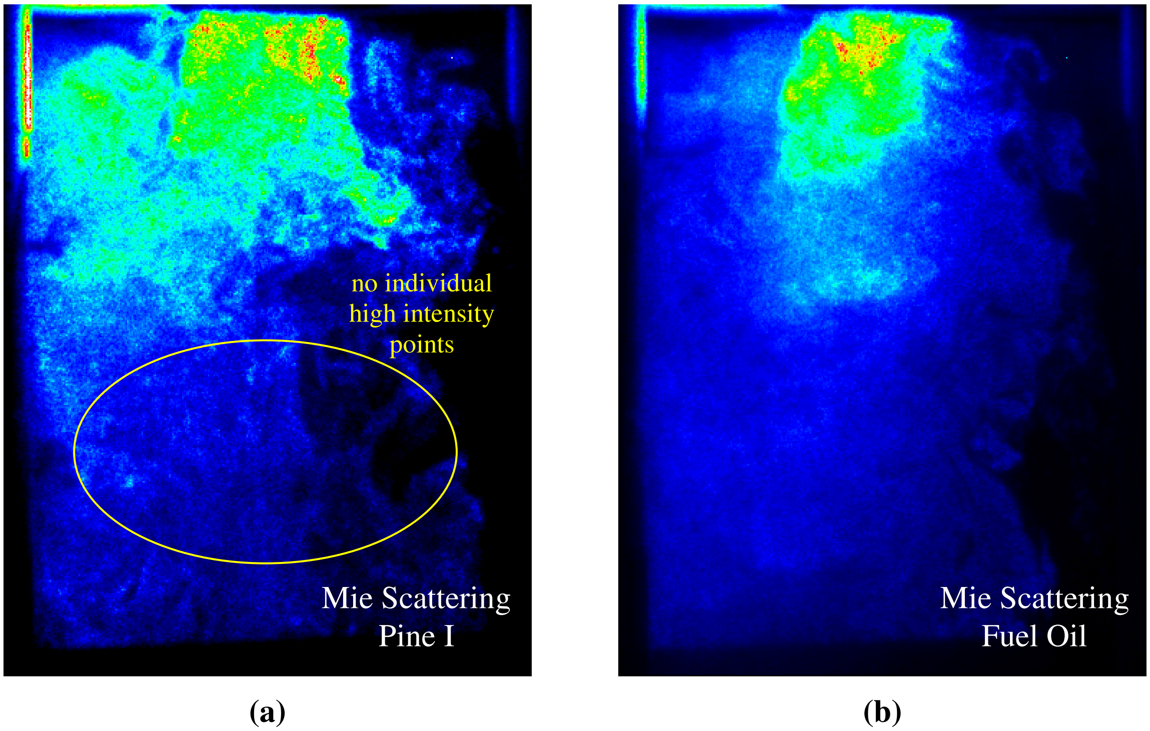

Figure 4.17 Mie Scattering images of cold pressure atomization sprays of Pine I fuel (a) and Fuel Oil (b).

Another possible explanation for the particles seen in the Mie Scattering images is that these particles are ash or solids from the parent fuel. However, there is a very high concentration of these particles in the Mie Scattering images, such that there is far too much material present given the small concentration of ash and solids in the Pine I oil.

Therefore, the most likely explanation of the particles observed in the Mie Scattering images is that they are indeed cenospheres given the following evidence.

1) All of the literature in single droplet combustion studies of pyrolysis oil have shown that cenospheres form during the combustion process.
2) The SEM images of pyrolysis oil particulate in this research reveal cenosphere-like structures with organic composition.
3) The literature has shown that the cenospheres can grown larger than the original droplet size, especially for smaller droplet sizes, agreeing with the observations of large particle sizes in the Mie Scattering images.
4) The literature has shown that censopheres have a longer burnout time in comparison to the volatile phase of combustion, agreeing with the observation of particles near the bottom of the combustion chamber in the Mie Scattering images.
5) The particles observed in the Mie Scattering images do not corroborate well with the LII or Fuel-PLIF images such that these particles are not likely to be simply soot or fuel.
6) Mie Scattering images of the cold spray do not show these particles, such that they must be formed during combustion (as are cenospheres).

With this evidence, and the lack of a reasonable alternative explanation, the particles observed in the Mie Scattering data are inferred to be censopheres. With this conclusion, and the conclusion that particulate emissions from the Pine I flame are dominated by cenospheres, the focus of this research is strongly directed towards understanding the role of cenospheres in pyrolysis oil combustion.

To begin the discussion of cenospheres, it is important to first note the size difference between the cenospheres collected on the filter paper and those seen in the scattering images. To be collected on the filter paper in the PM measurement method, the particles must be small enough to be entrained in the flow so that they are carried through the sampling line to the filter paper. If they are large, aerodynamic drag forces will be insufficient to entrain the particles such that they will not be collected on the filter paper. Indeed, the largest particle observed in any of the SEM images in this research was approximately 10 µm in diameter.

The cenospheres observed in the Mie scattering data appear to be much larger, with signal intensities which can fill several pixels (~650 µm /pixel). Cenospheres which are this large would certainly not be entrained in the flow sufficiently to be collected in the filter paper of the PM measurements. However, in the Mie Scattering data the cenospheres show a wide range of size distributions, with many signals which are only one pixel in size. These particles may be smaller than 650 µm; however, as the size gets smaller, the Mie scattering signal intensity decreases by the square of the diameter. As such, it is unlikely that very small cenospheres can be detected in the Mie Scattering data. However, it also seems likely that if large cenospheres are observed in the Mie Scattering images, then small censopheres are likely present as well.

The SEM images of the Pine I particulate show that there are agglomerates of several smaller cenospheres. These primary cenospheres are typically in the range of 1 μm. Although it is possible that these small cenopsheres may be the remaining shell of a droplet, they are very small, likely smaller than the smallest droplet sizes in the fuel spray. Another possible explanation of these cenospheres is that they are the remains of fuel fragments generated from microexplosions during the combustion event.

The large cenospheres observed in the Mie Scattering data, may be caused by the swelling of individual droplets; however, this seems unlikely for particles which are several pixels in diameter. Another possibility is that these large particles are large agglomerations of several smaller cenospheres. The SEM image of the pressure-atomized particulate shows that indeed several cenopsheres are bound together in a large agglomerate. Further, the literature in single droplet combustion studies of pyrolysis oil has shown that agglomeration of fuel residues occurs after the microexplosion. It seems even more likely that agglomeration would occur in the dense fuel spray generated by the pressure-atomized nozzle.

Large amounts of fuel residues have been found to collect and burn on the combustor walls and bottom refractory plate in the Pine I oil pressure atomization studies. These fuel residues are likely cenospheres which are failing to burn in the flame. Some small cenospheres also apparently fail to burn, as they are collected in the particulate measurements. In either case, some of the cenospheres are failing to burn in the flame.

An examination of the flame luminosity and Mie Scatting as displayed in Figure 4.18 shows the location of the cenospheres in relation to the flame. The flame shows that some individual combustion of cenospheres occurs near the extremities of the visible flame.

However, far away from the flame, there is very little indication of cenosphere combustion. This suggests that as cenospheres pass beyond the hot flame zone, they are cooled such that they are unable to burn with a high luminoisty. An exception to this can be seen in the lower, right portion of the flame image, which shows a small flame along the combustor wall. The chamber walls are very hot such that are able to ignite pyrolysis oil residues after having sufficient time to heat up while sitting on the chamber walls.

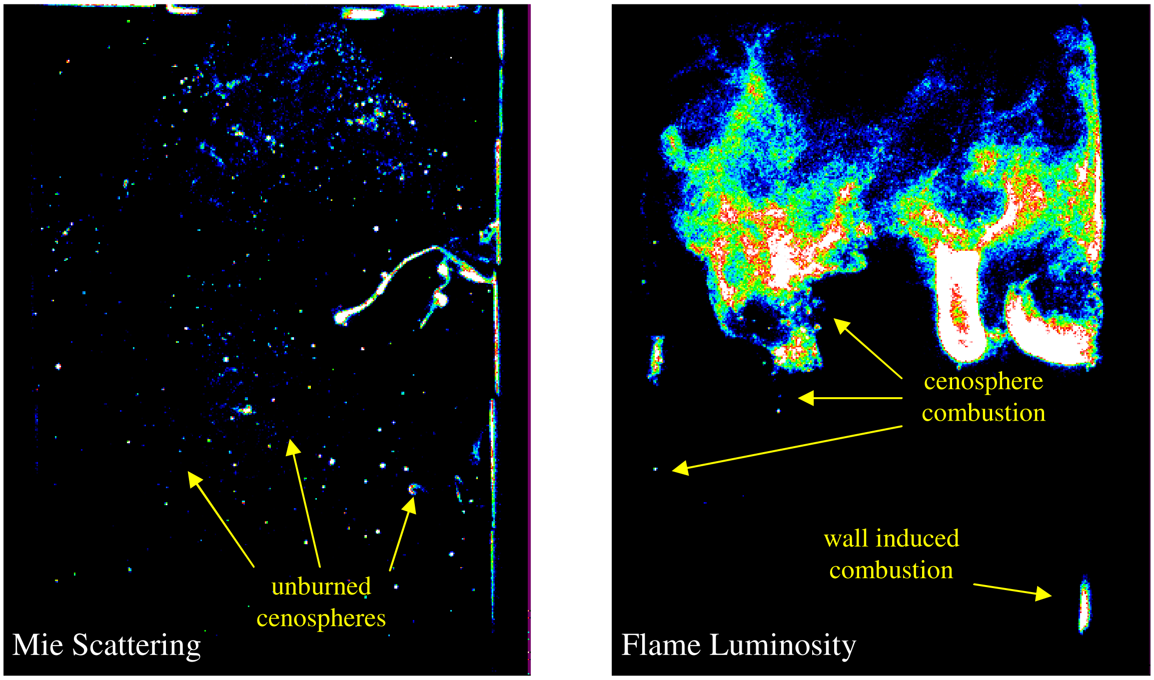

(a) (b)

Figure 4.18 Simultaneous Mie Scattering (a) and flame (b) images of Pine I fuel combustion with pressure atomization at 0.95 equivalence ratio.

In addition to the flame luminosity, it is relevant to examine the region of OH concentration in the combustion chamber. Once again, the OH signal was very low during these tests, such that single images do not reveal a good depiction of the OH in the flame. As such, a simple average of the OH signal has been produced, with the flame background subtracted as shown in Figure 4.19. Because the Pine I oil does not fluoresce over the range of OH detection, the average OH-PLIF image in Figure 4.19 shows only the distribution of OH and not a combined distribution of OH and fuel as was the case in the Fuel Oil images. The OH concentration appears to be highest in the upper half of the visible flame region. Thus, many cenospheres exist beyond the flame zone and fail to burn.

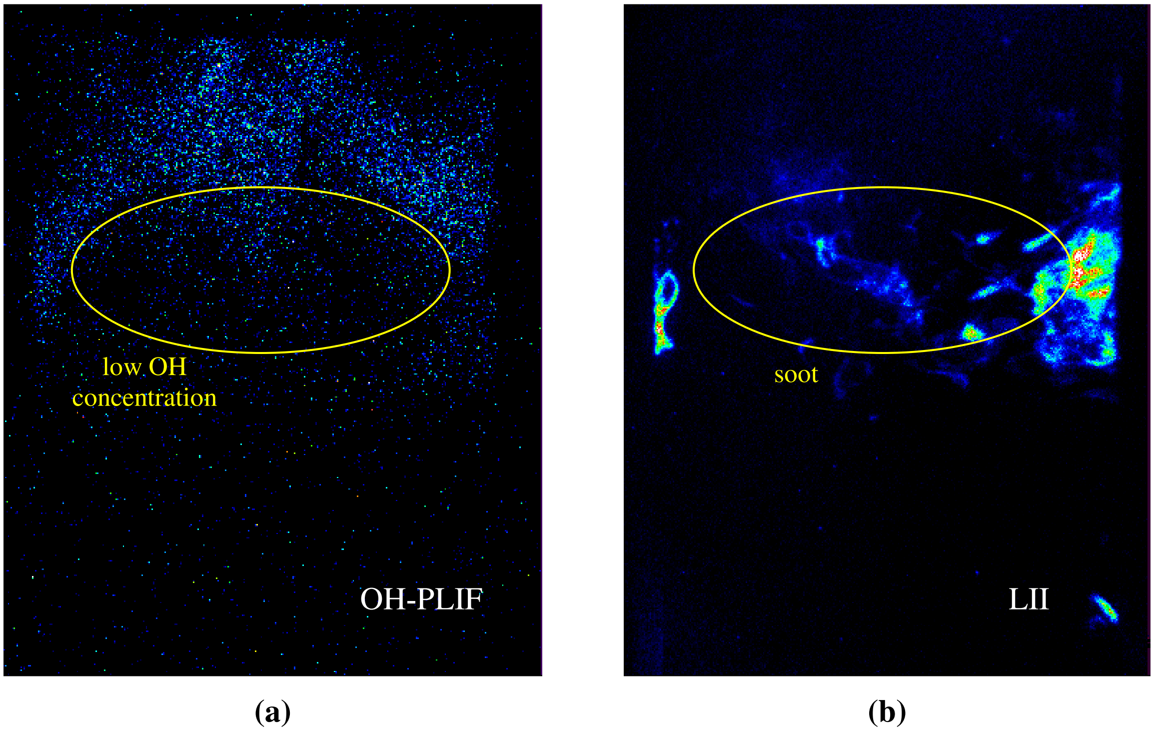

Figure 4.19 Simple average of OH-PLIF (a) and LII (b) images of Pine I combustion with pressure atomization at 0.95 equivalence ratio.

A background-subtracted simple average of the LII is displayed in Figure 4.19 for comparison to the OH signal. The OH signal shows a low concentration in the bottom-middle portion of the visible flame zone. The LII shows that some soot exists in that region of the flame (which is what gives the flame its luminosity in that region). Therefore, on average, there is not much OH available to oxidize the soot in that region of the flame. Further, this soot region is near the edge of the flame and is likely headed away from the flame zone, towards regions which are cooler and lack sufficient OH concentration.

To be complete in this discussion, it should be noted that OH and LII do not overlap at an instant in time within the flame zone [76]. However, these regions are adjacent within the flame, and in a turbulent flame, the content at a particular location in a flame can switch between OH and soot. As such, an average of images of OH and LII in a turbulent flame will show some overlap in these regions even if they do not overlap at a given instant. This has been seen in the discussion of the pressure-atomized fuel oil flame in Section 4.2.1.2. Moreover, in the fuel oil flame, OH was found to be on the outside of the flame zone, with the soot moving towards OH rich regions. In the Pine I flame, there is not a strong overlap between the OH and soot, and further, the soot is moving out of the flame zone away from OH rich regions, not towards them. Thus, it seems that the soot which appears in the SEM images of the particulate is a result of soot quenching.

At this point, a complete picture of the Pine I oil pressure-atomized flame has been constructed. Stabilization is aided by the hot combustor walls and buoyancy forces. Dense regions of small fuel droplets are observed along the top-outer regions of the spray, while soot regions are found along the bottom and outer edges of the flame. The OH is concentrated largely along the top edge of the flame, and does not overlap the soot region entirely such that soot fails to fully oxidize in the flame.

Cenospheres are found throughout the flame zone, with high concentrations found along the outer edge of the spray cone. They are found both beyond the visible flame and OH regions, with some single cenosphere combustion observed at the edges of the visible flame zone. Some cenospheres are found to burn upon reaching the hot combustor walls lower in the chamber. The cenospheres have a very wide range in size, ranging from less than 1 μm to greater than 1 mm.

4.2.2 Effect of Equivalence Ratio

The Pine I oil was studied at an equivalence ration of 0.7 in addition to 0.95 to study the effect of this change on the exhaust emissions and flame structure. The particulate emissions of the pressure-atomized Pine I oil flame are shown in Figure 4.20. In decreasing the equivalence ratio from 0.95 to 0.7, the particulate emission decrease.

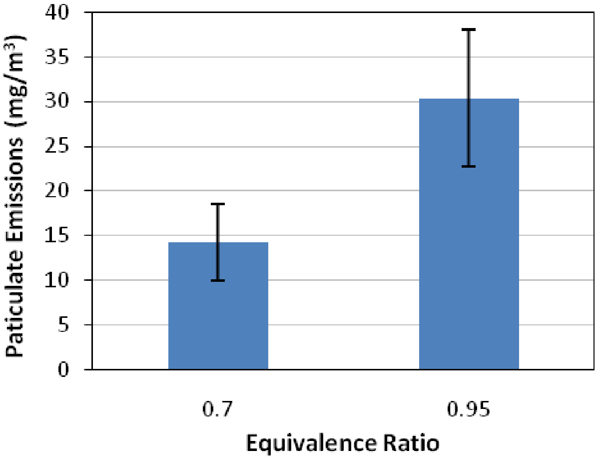

Figure 4.20 Particulate emissions of Pine I oil in a pressure-atomized flame.

Scanning electron microscope images of the particulate collected during these tests is shown in Figure 4.21 for both 1k and 10k magnifications. For both cases, cenosphere agglomerates can be seen in the particulate. The size of the primary particles and overall agglomerates appears to be similar for both cases. The main difference between these two cases is that there is soot in the 0.95 equivalence ratio image while there is not any soot in the 0.7 equivalence ratio image. Thus, the reduction of particulate emissions from the 0.95 to 0.7 equivalence ratio case appears to be due to a reduction of soot in the exhaust. This seems reasonable, given that at 0.95 equivalence ratio there is only slightly more than enough oxygen present overall in the flame, such that there are likely large fuel-rich regions and limited OH regions in the flame. To better understand this phenomenon, visualization studies have been performed.

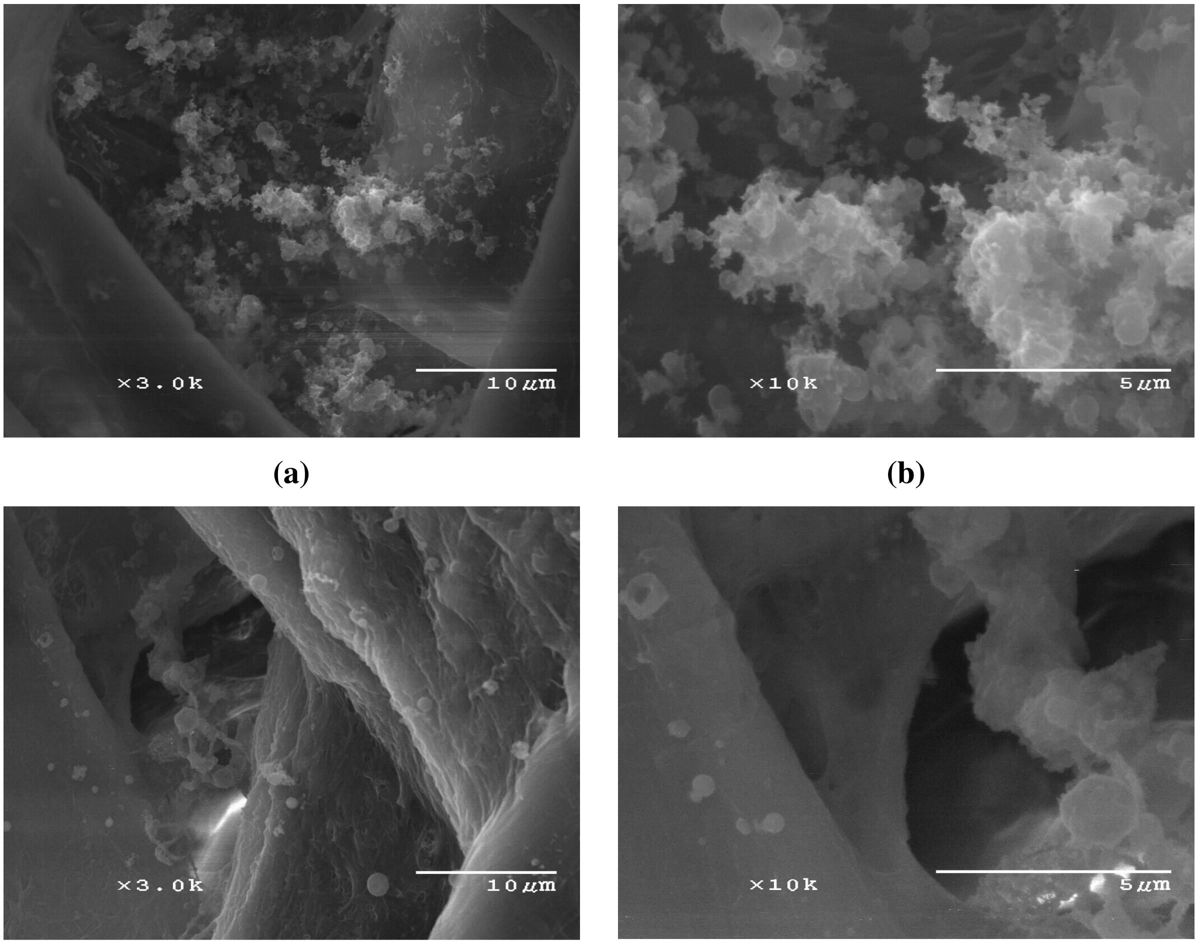

(a) **(b)**

(c) **(d)**

Figure 4.21 SEM images of particulate collected for Pine Oil I at 0.7 equivalence ratio with 10k (a) and 1k (b) magnification and particulate collected for Pine I Oil at 0.95 equivalence ratio with 10k (a) and 1k (b) magnification.

The structure of the 0.95 equivalence ratio pressure-atomized Pine I oil flame has been well documented in Section 4.2.1.2. The structure of the 0.77 equivalence ratio flame does not differ significantly, and therefore it will not be outlined in detail. Rather, the only images discussed are those which pertain to the change in soot observed in the exhaust emissions.

Simple averages of the OH-PLIF and LII images for the 0.7 and 0.95 equivalence ratio flames are shown in Figure 4.22. In the 0.95 case, there is a large region of soot in the lower-middle portion of the flame, in which the soot concentration is low. As was discussed in Section 4.2.1.2, this is likely the cause of soot emissions for that case. In the OH-PLIF and LII images of the 0.7 equivalence ratio flame, the regions of high soot concentration overlap well with regions of high OH concentration. As such, there is sufficient OH present to oxidize the soot in the 0.7 equivalence ratio case, and hence the lack of soot in the PM.

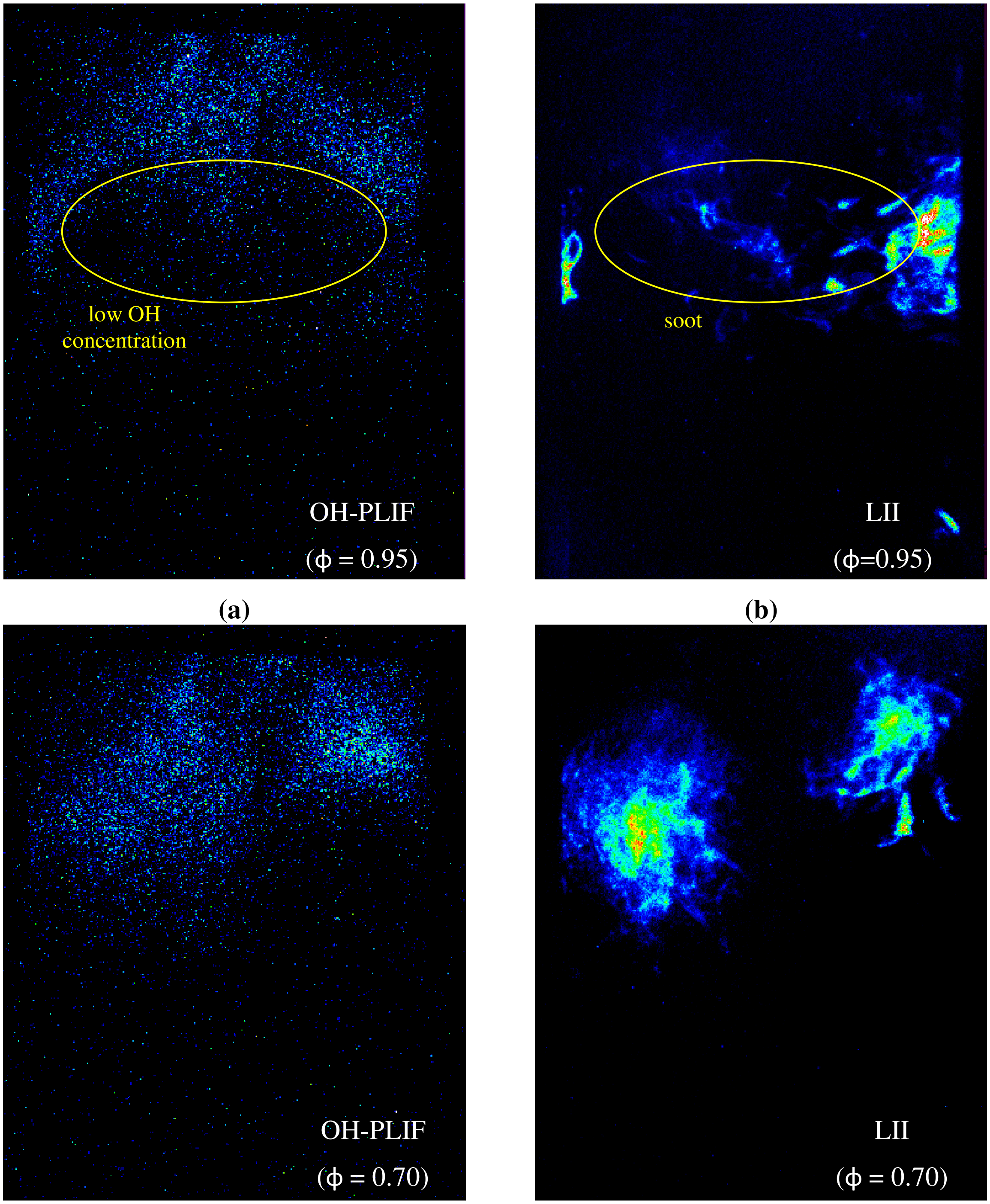

(a) (b)

(c) (d)

Figure 4.22 Simple average of OH-PLIF and LII images of Pine I combustion with pressure atomization at 0.95 (a,b) and 0.70 (c,d) equivalence ratio.

4.3 Air Atomization Studies

Several detailed studies of air-atomized pyrolysis oil flames have been studied. These studies can be divided into two groups, according to the availability of fuel samples and equipment during these tests.

The first set of tests discussed provides a comparison of Fuel Oil, Pine I, and Corn Fraction fuels at 18 kW and 0.95 equivalence ratio as detailed in Section 4.3.1 (Comparative Fuel Studies). Exhaust gas emissions were measured with the LumaSense ANDROS 6900 gas analyzer. Several visualization techniques were used to study the flames including Mie Scattering, Fuel-PLIF, OH-PLIF, and flame luminosity measurements.

The second set of tests provide a detailed study of the effects of equivalence ratio, atomization air flowrate, and water content in Pine II fuel combustion, as discussed in Sections 4.3.2 (Effect of Equivalence Ratio), 4.3.3 (Effect of Atomization Air Flowrate), and 4.3.4 (Effect of Water Content), respectively. Fuel Oil has been used as a baseline fuel for comparison. Carbon monoxide (CO) and HC emissions were measurement with the Horiba MEXA-554J gas analyzer. High power LII measurements were used to visualize soot in the flames and high speed flame luminosity images were captured to observe visible flame structures.

4.3.1 Comparative Fuel Studies

Three different fuels (Fuel Oil, Pine I, and Corn Fraction) have been studied at an equivalence ratio of 0.95 and a thermal load of 18 kW. This corresponds to fuel flowrates of 0.45, 0.77, and 0.85 gph for the Fuel Oil, Pine I, and Corn Fraction fuels respectively. Because there is such a large difference in fuel flowrates, it is not possible to use the same nozzle size for each fuel. A Delevan Siphon Air nozzle size -8 was used for the Pine I and Corn Fraction fuels, and size -5 was used for the Fuel Oil. An atomization air flowrate of 16 slpm was used for the fuel oil, while a flowrate of 24 slpm was used for the pyrolysis oils, such that the volumetric ratio of fuel flowrate to atomization air flowrate was comparable for all fuels studied. During the Fuel Oil tests neither the fuel nor the combustion air was intentionally heated; however, the fuel temperature was increased to 50 °C and the air temperature increased to 130 °C due to heat transfer from the chamber to the burner housing. The combustion air was preheated to 300 and 330 °C, for the Pine II and Corn Fraction fuels, respectively, such that the adiabatic flame temperature for all fuels was comparable. The Pine II fuel was preheated to 70 °C and the Corn Fraction fuel heated to 83 °C, so that both fuels would have comparable kinematic viscosities.

Exhaust gas emissions were measured with the LumaSense ANDROS 6900 gas analyzer. Several visualization techniques were used to gain a better understanding of the flame structure including Mie Scattering, Fuel-PLIF, OH-PLIF, and flame luminosity measurements.

The difference in flame structure between pyrolysis oil and fuel oil is not as significant with air atomization as it is with air atomization. All of the fuels were stabilized on the swirler head as shown in the flame luminosity images in Figure 4.23. The Pine I and

Corn Fraction flames have very similar appearances, with a wide luminous section in the top of the flame. Further, in both flames, individual high intensity points can be seen near the edges of the flame, which looks similar to the combustion of cenospheres as observed in the pressure-atomized flames. The Fuel Oil flame is narrower than the pyrolysis oil flames, with more variation in signal intensity across the flame.

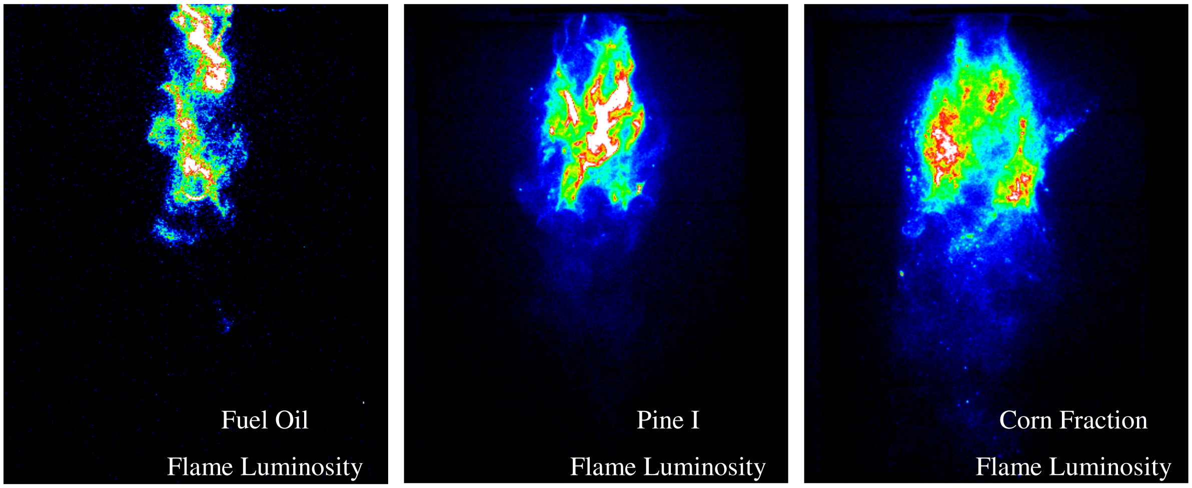

(a) **(b)** **(c)**

Figure 4.23 Flame luminosity images of Fuel Oil (a), Pine I (b), and Corn Fraction (c) in air-atomized flames at 18 kW and 0.95 equivalence ratio.

Spectrometer measurements of the flames are displayed in Figure 4.24. These results show that the luminosities of the flames are very comparable for all fuels, especially for the Pine I and Corn Fraction fuels. Fuel Oil is more luminous than either of the pyrolysis oils; however, this difference in luminosity is not nearly as significant as the difference observed in the pressure-atomized flame as shown in Figure 4.6. Once again, the reduced luminosity of pyrolysis oils may detract from its potential use as a fuel in radiative boilers; however, this could prove to be a benefit for use in turbine applications.

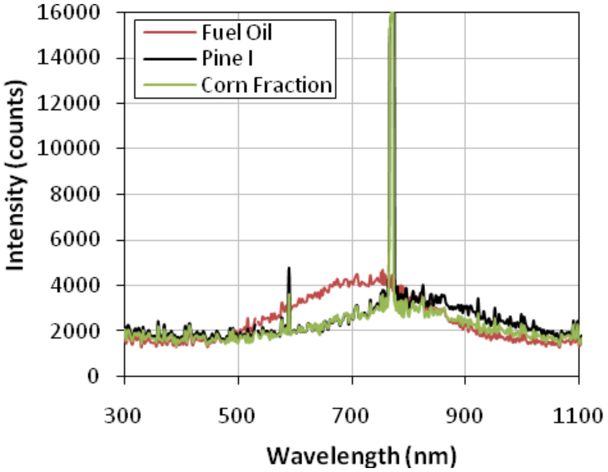

Figure 4.24 Spectrometer measurements of Corn Fraction, Pine I, and Fuel Oil air-atomized flame emission with 5 s integration time.

The spectrometer results also show that both the Pine I and Corn Fraction oils have strong chemiluminescence from potassium and sodium. The potassium peaks are saturated in the detector such that their relative magnitudes cannot be compared; however, it is interesting to note how strong the potassium chemiluminescence is for the Corn Fraction fuel, given that the potassium content in this fuel is much lower than that in the Pine I fuel. Further, the sodium peak is slightly higher for the Corn Fraction fuel despite the fact that the dispersive energy X-ray analysis results in Figure 3.21 show the Pine I fuel to contain slightly more potassium. This may be an indication of there being substantial uncertainty in the dispersive energy X-ray analysis data.

With regard to exhaust emissions, the CO and HC emissions were found to be less than 100 and 20 ppm, respectively for all fuels. Nitrogen oxide (NOx) emissions were found to be approximately 100 ppm for both the Pine I and Fuel Oil fuels; however, for the Corn

Fraction fuel, NOx emissions were found to be greater than 1400 ppm as shown in Figure 4.25. This large increase in NOx emissions is a result of the high nitrogen content in the Corn Fraction fuel. This suggests that nitrogen levels need to be minimized in pyrolysis oils to prevent unacceptable levels of fuel-bound NOx from forming during combustion.

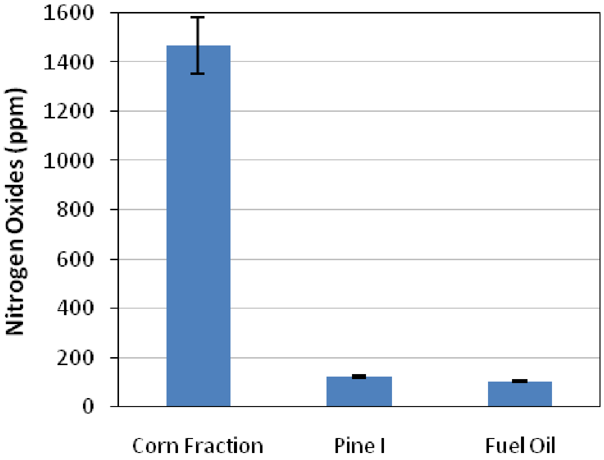

Figure 4.25 Nitrogen oxide emissions of Corn Fraction, Pine I, and Fuel Oil air-atomized flames at 0.95 equivalence ratio.

Particulate emissions are shown Figure 4.26. All of the particulate measurements are very low for the atomization air flames. At these conditions the average Fuel Oil particulate measurement was 0.31 mg/m^3, which is almost zero to within the measurement uncertainty of the device, considering the AVL 415S smoke meter often reports values this high when taking measurements of ambient air. There is a decrease in moving from Corn Fraction to Pine I to Fuel Oil; however, these values are all so low that these differences are somewhat insignificant.

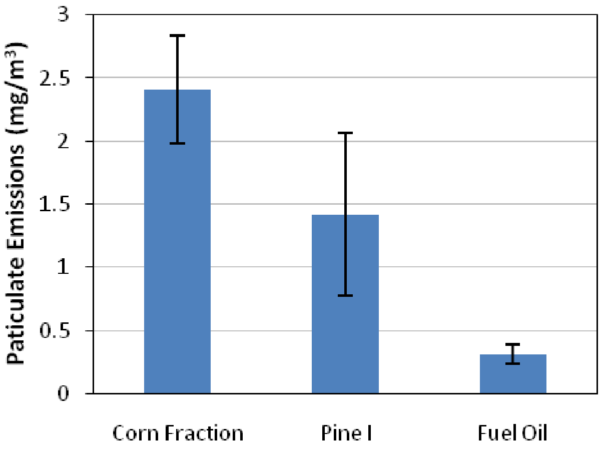

Figure 4.26 Particulate emissions of Corn Fraction, Pine I, and Fuel Oil air-atomized flames at 0.95 equivalence ratio.

What is perhaps more interesting is the fact that the Pine I and Corn Oil fuels both have such low emissions, and further, that both fuels have such similar emissions. The reduction in emissions in the Pine I oil from the pressure-atomized flame to air-atomized flame is very significant. Further, it is somewhat surprising that the Corn Fraction and Pine I oils have such similar particulate emissions given the many differences in their chemical compositions as shown in the GC-MS results in Figure 3.19. It may be that the increase in particulates for the Corn Fraction fuel is a result of having a higher fixed carbon content; however, there is little proof for this claim. These fuels differ significantly in water content and heating value; however, they are very comparable in adiabatic flame temperature, such that the flame temperature may be a better indicator of the combustion results.

Because the particulate emissions were so low for all of these measurements, SEM images of the particulate could not be acquired. However, both the Corn Fraction and Pine I particulate samples were brown in color, suggesting the presence of cenospheres. The Fuel Oil filter paper sample was too faint for its color to be discerned.

Further evidence that the particulate in the pyrolysis oil flames was caused by cenospheres, can be seen in scattering images in the flames as shown in Figure 4.27. In both the Pine I and Corn Fraction images, individual high intensity points can be seen in the chamber, while the Fuel Oil images show no such structures. Given the findings in pressure atomization flame studies, and the fact that these particles have very long residence times in the chamber, it is very likely that these are cenospheres.

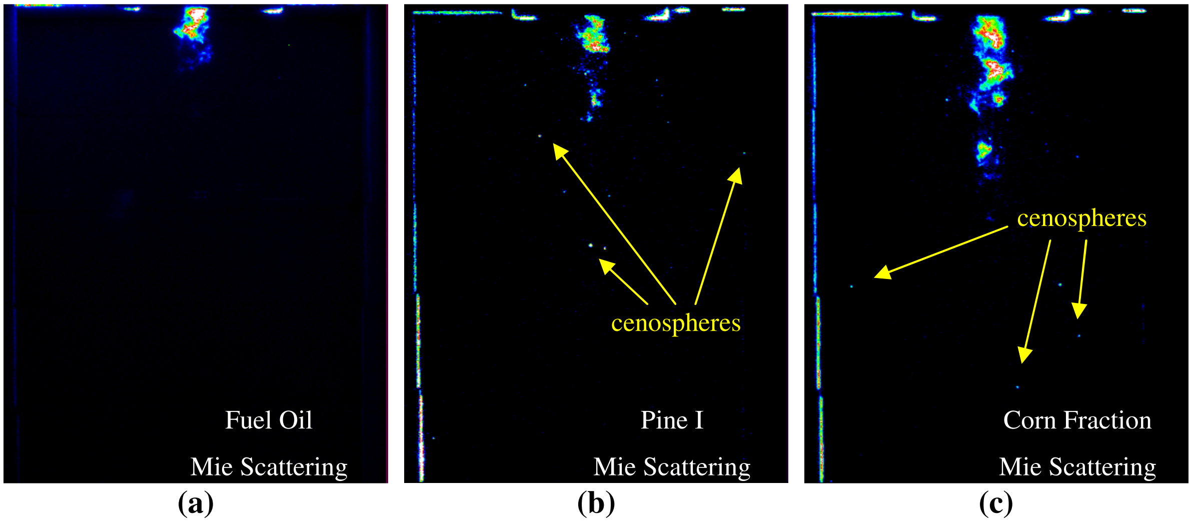

(a) (b) (c)

Figure 4.27 Mie scattering images of Fuel Oil (a), Pine I (b), and Corn Fraction (c) in air-atomized flames at 18 kW and 0.95 equivalence ratio.

To provide further evidence that these structures are indeed cenospheres, Mie Scattering images of cold fuel sprays have been collected as shown in Figure 4.28. The sprays look comparable for all fuels. There are no large individual structures found in the Corn Fraction or Pine I sprays images. As such, the structures which are found in the Mie Scattering images of the flame must have been formed during combustion. With this, it is concluded that these structures are indeed cenospheres.

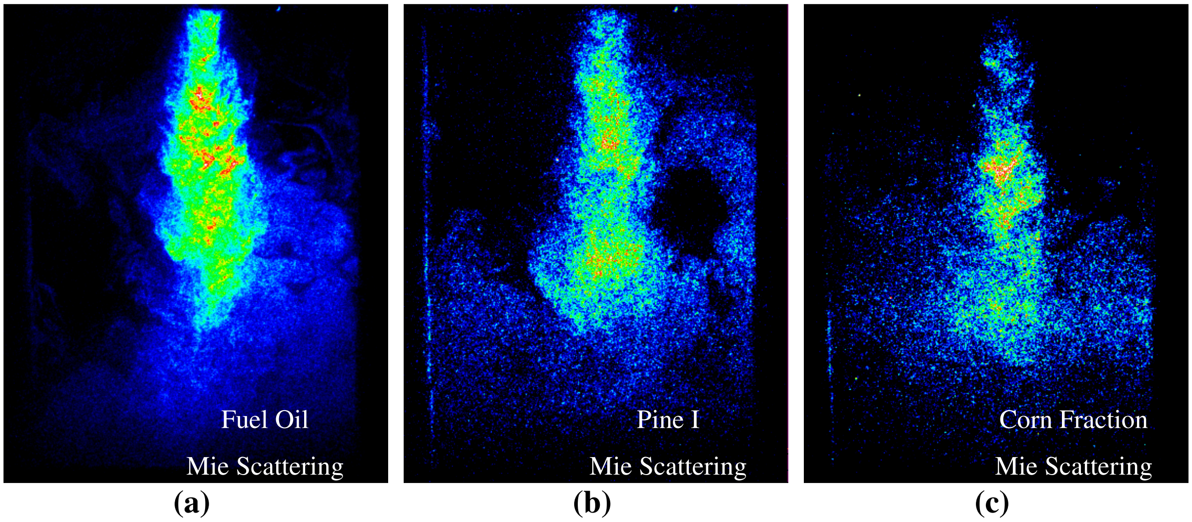

(a) **(b)** **(c)**

Figure 4.28 Mie scattering images of Fuel Oil (a), Pine I (b), and Corn Fraction (c) air-atomized cold flow sprays at 18 kW and 0.95 equivalence ratio.

With regard to the cenospheres, there are far fewer detected in the air-atomized flames than in the pressure-atomized flames. This agrees well with the large reduction in particulate emissions in moving from pressure atomization to air atomization. Further, in the pressure atomization Mie Scattering images, large droplets were observed along the outer edge of the spray in the Fuel Oil flames in Figure 4.11. All of this suggests that the air atomization nozzles produce a better spray with regard to droplet diameter and dispersion. Smaller, more dispersed droplets should result in smaller cenospheres and a reduction of aggregation of cenospheres in the flame; hence the reduction of cenospheres detected in the Mie Scattering images. Smaller cenospheres should also have faster burning rates; hence the reduction of particulate emissions.

Because there are so few cenospheres present in the Mie Scattering images, a threshold average of the images has been produced to show a summation of the cenospheres as shown in Figure 4.29. The pixel intensity histogram of the images is shown in Figure 4.29 as well along with the location of the threshold intensity limit which has been chosen.

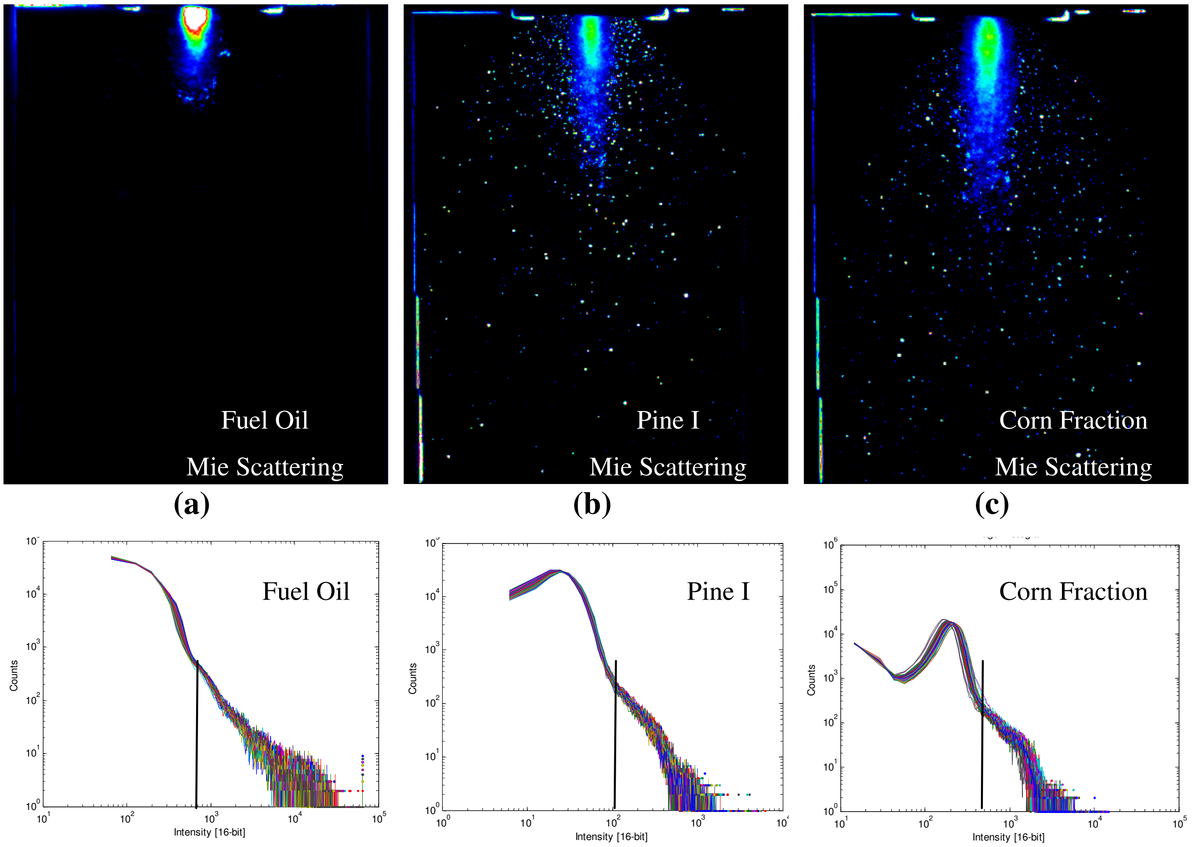

(a) (b) (c)

(d) (e) (f)

Figure 4.29 Threshold average of Mie scattering images of Fuel Oil (a), Pine I (b), and Corn Fraction (c) air-atomized flames at 18 kW and 0.95 equivalence ratio with the corresponding image intensity histogram plots and threshold points for Fuel Oil (a), Pine I (b), and Corn Fraction (c) .

Not surprisingly, Fuel Oil shows no cenospheres. The Pine I and Corn Fraction flames both show several cenospheres; however, there does not appear to be a significant difference between number and distribution of the cenospheres in these two flames. Further, although it is difficult to clearly distinguish size, it does not appear that there is a significant difference in the size of the cenospheres between the two fuels. The only difference between these images is that of the size of the core spray region. This size difference is most likely a result of the difference in volumetric fuel flowrates between the fuels. As such, it appears that there is almost no detectable difference between the cenosphere characteristics of the Pine I and Corn Fraction fuels.

To gain an understanding of the cenospheres in relation to the location of the hot regions of the flame, simple averages of the OH-PLIF and flame luminosity images are shown in Figure 4.30. Because of Fuel Oil fluoresces over the region of OH detection, the hydroxyl radical cannot be detected independently of the fuel. As such, the OH-PLIF image of the Fuel Oil flame has been labeled as OH/Fuel-PLIF, indicating that both fuel and OH are visible in the image. Given the region of dense fuel spray in the Mie Scattering images of the fuel spray, the top portion of the OH/Fuel-PLIF image is attributed to fluorescence from the Fuel Oil.

The distribution looks very similar for all three fuels, with a large region of OH concentration throughout the middle of the chamber. The average flame luminosities look similar between the Pine I and Corn Fraction fuels, with the regions of highest luminosity towards the top of the chamber. The Fuel Oil flame appears to be narrower and longer than the pyrolysis oil flames.

A significant feature of the air-atomized flames is that the region of OH concentration reaches beyond the visible flame region for all flames. In the pressure-atomized flames, this feature was not as evident and is likely the cause of both soot and cenosphere quenching in the flames. In the air-atomized flames, significant amounts of OH are available at lower regions in the chamber allowing for more complete oxidation of both soot and cenospheres.

This is likely a major contributor to the reduction in particulate emissions in air-atomized flames in comparison to pressure-atomized flames.

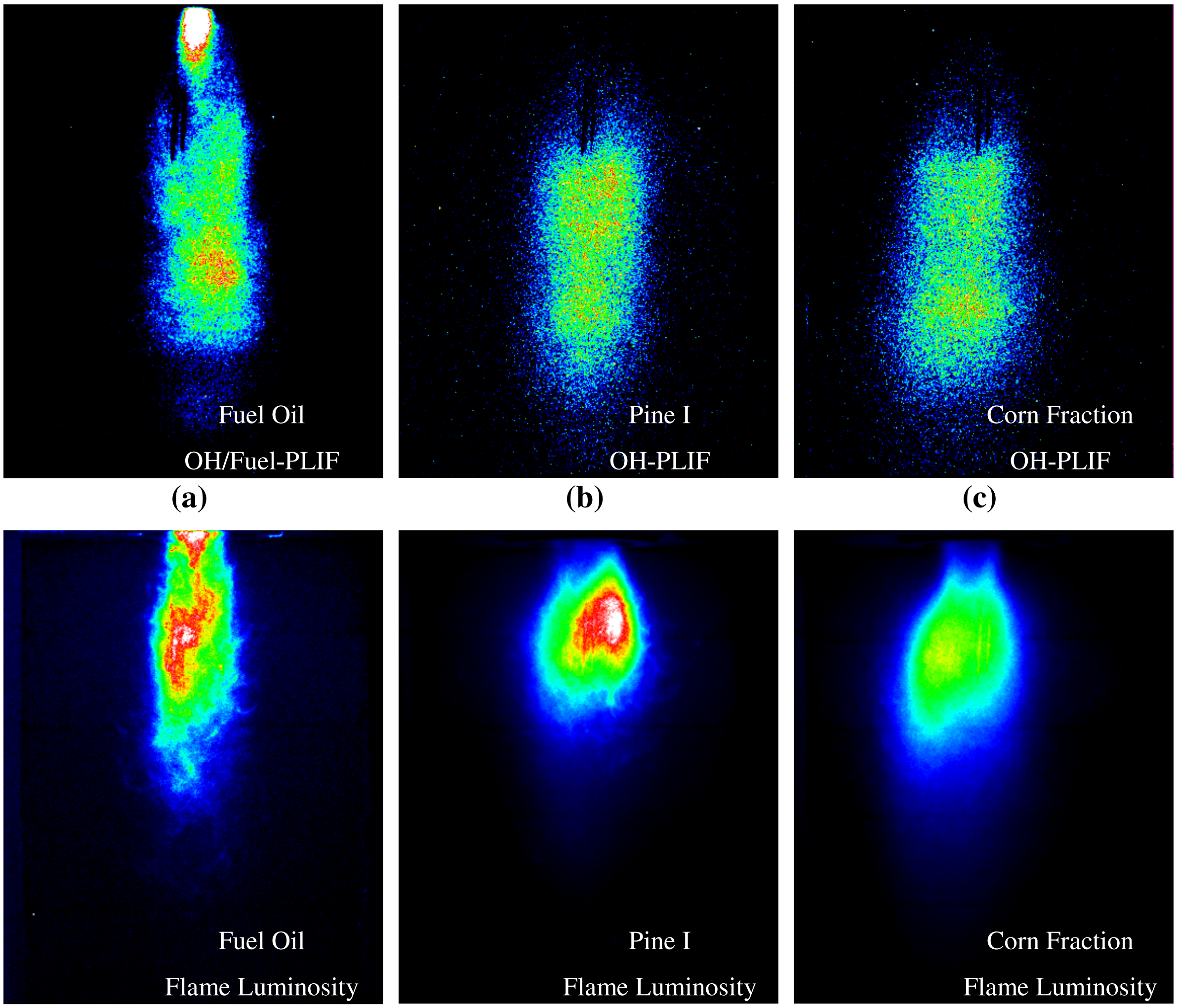

(a) (b) (c)

(d) (c) (e)

Figure 4.30 Simple averages of OH-PLIF images of Fuel Oil (a), Pine I (b), and Corn Fraction (c) air-atomized flames and simple averages of flame luminosity images of Fuel Oil (d), Pine I (e), and Corn Fraction (f) air-atomized flames and at 18 kW and 0.95 equivalence ratio.

Examination of the PM emissions, Mie Scattering, OH-PLIF, and flame luminosity shows that there is little difference between the combustion behavior of the Pine I and Corn

Fraction fuels. However, Fuel-PLIF images of the flames reveals differences in the fluorescence behavior of the two fuels as shown in Figure 4.31. Representative flame background images have been shown to display the magnitude of the Fuel-PLIF signal relative to the background flame emission under the same camera detection settings.

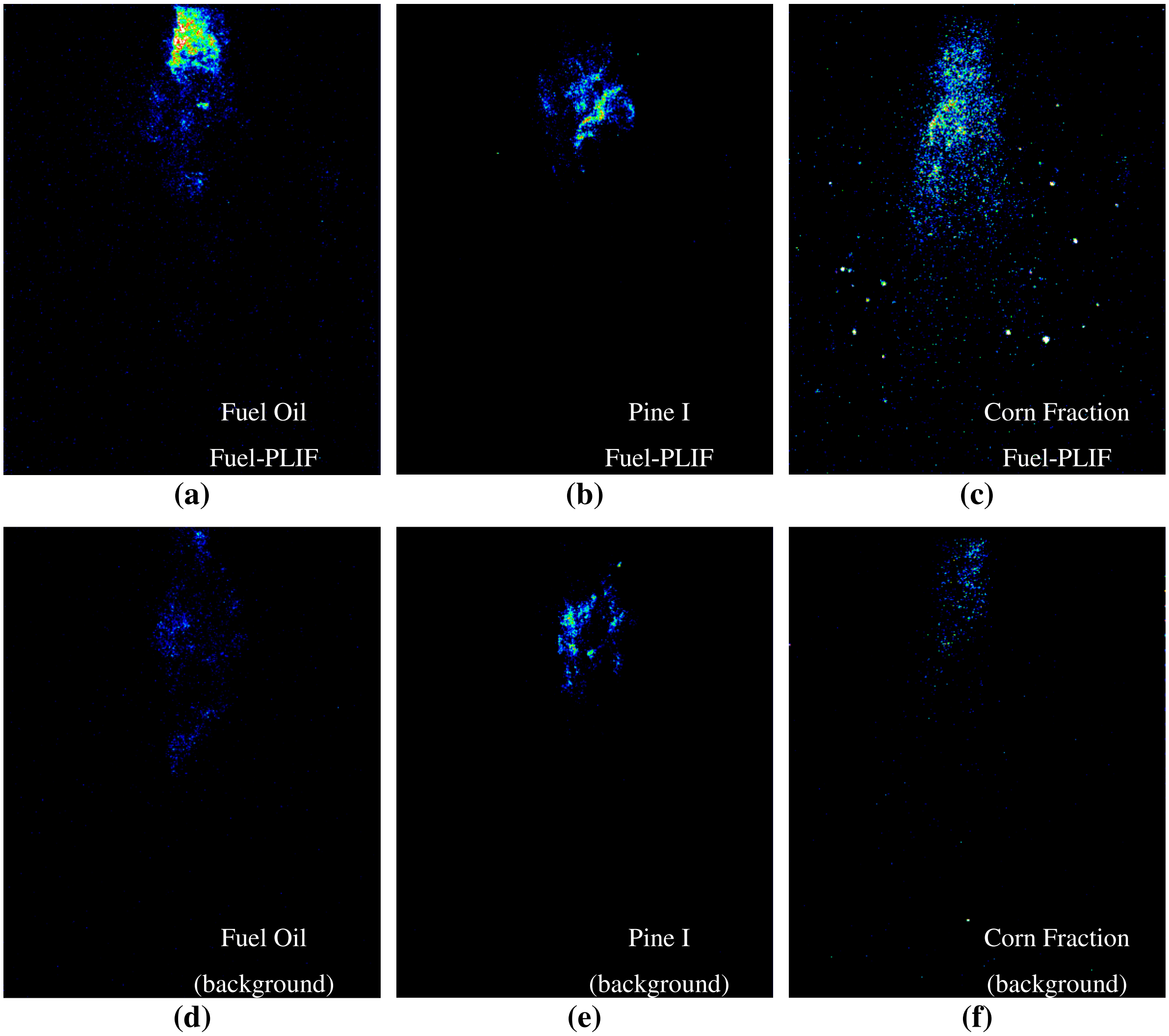

Figure 4.31 Fuel-PLIF images of Fuel Oil (a), Pine I (b), and Corn Fraction (c) in air-atomized flames at 18 kW and 0.95 equivalence ratio.

The Fuel Oil and Corn Fraction fuels show high fluorescence signal relative to the flame background while the Pine I fuel does not, despite the fact that the same camera settings were used and all tests were performed with laser energy of 9 mJ/pulse. This indicates a difference in the fluorescence behaviors, and therefore chemical composition of the fuels. However, it is interesting to note that the trends in these images do not agree with the trends in the UV fuel fluorescence spectrums of Figure 3.30. It seems possible that the fluorescence spectrums are the result of a few key species in the fuels. It may be that the species in the Corn Fraction fuel which provide the strongest fluorescence also have low volatilities, such that they remain in the liquid phase longer in the flame zone, providing stronger Fuel-PLIF signal in the flame images.

Further evidence that the fluorescing species in the Corn Fraction oil have low volatilities is shown by the fact that several individual high intensity points can be seen in lower regions of the combustion chamber, suggesting that these particles have very low volatilities. Indeed, given this low volatility and their shape, these look very similar to the cenospheres which are observed in the scattering data.

Aside from the differences between the Mie Scattering and Fuel-PLIF images, it is of interest to note that the Corn Fraction cenospheres fluoresce, while the Pine I cenospheres do not. Therefore, the physical and/or chemical composition of the cenospheres is likely different between the two fuels. It is striking to note that these cenospheres are apparently different in composition; however, very similar in behavior with regard to rates of formation and oxidation. It may be that the chemical species governing the cenosphere phenomena are the same between both fuels, but that each fuel contains additional chemical species which are present during the cenosphere stage.

Another interesting phenomena of the Corn Fraction oil is that the cenosphere fluorescence is much stronger than the fluorescence in the dense fuel spray region. This suggests that at least some of the fluorescing compounds in the species are concentrated during the production of the cenospheres.

4.3.2 Effect of Equivalence Ratio

To investigate the effect of equivalence ratio on pyrolysis oil combustion in air-atomized flames, Pine II oil and Fuel Oil have been studied at a thermal load of 19.2 kW. This corresponds to volumetric fuel flowrates of 0.86 for the Pine II oil and 0.47 for the Fuel Oil. Because there is such a large difference in fuel flowrates, it is not possible to use the same nozzle size for each fuel. A Delevan Siphon Air nozzle size -8 was used for the Pine II oil and size -5 was used for the fuel oil. Atomization air flowrates of 33 and 20 slpm were used for the Pine II oil and Fuel Oil respectively, such that the volumetric ratio of fuel flowrate to atomization air flowrate was similar between both studies. Equivalence ratio has been varied by adjusting the flowrate of the combustion air to the burner. During the Fuel Oil tests neither the fuel nor the combustion air was intentionally heated; however, the fuel temperature was increased to 50 °C and the air temperature increased to 130 °C due to heat transfer from the chamber to the burner housing. The Pine II fuel was heated to 80 °C and the combustion air preheated to 300 °C for all tests.

Only one PI-MAX SB camera was available during these studies such that only one laser diagnostic measurement could be performed at a time. High power LII studies were performed with laser energy of 700 mJ/pulse for Pine II and 425 mJ/pulse for Fuel Oil mJ/pulse. The high energy was required to visualize soot in the Pine II flames; however, for Fuel Oil the soot levels were so high that attempts at using 700 mJ/pulse lead to saturation ofthe ICCD camera. The Phantom high speed camera was available during these studies, such that high speed imaging of the flame luminosity was performed with the LII measurements. For the high speed imaging exposure times of 2 and 10 microseconds were used for Fuel Oil and Pine II oil, respectively, due to the significant difference in the flame luminosities between the two flames.

Carbon monoxide (CO) and HC emissions were measured with the Horiba MEXA-554J gas analyzer. Nitrogen oxide emissions were not measured. All emissions data presented represents an average of at least three measurements. The error bars shown correspond to a 68% confidence interval of those measurements. If error bars are not displayed, then they are smaller than the data point symbol on the plot.

4.3.2.1 Effect of Equivalence Ratio – Exhaust Emissions

The particulate emissions as a function of equivalence ratio for both the Pine II oil and Fuel Oil are shown in Figure 4.32. Fuel oil shows a characteristic trend with very low particulate emissions at lean conditions ($\phi < 1$) and a significant increase in particulate at rich conditions ($\phi > 1$) resulting from soot exiting the combustor because of insufficient concentrations of fuel oxidizer.

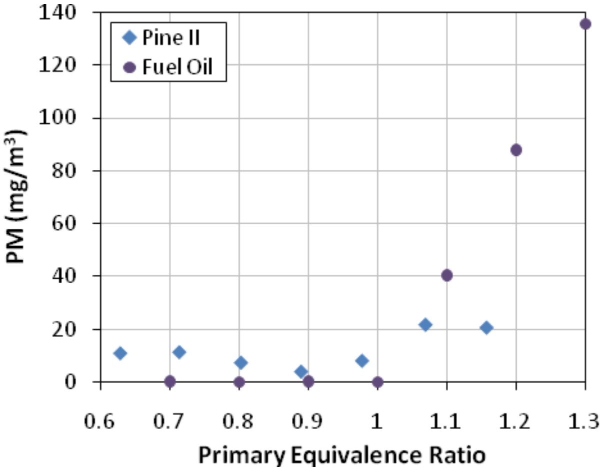

Figure 4.32 Particulate concentration vs. equivalence ratio for Pine II and Fuel Oil.

The Pine II oil shows some unique characteristics in its particulate emissions trend. At lean conditions, the particulate levels are not zero, and in fact they decrease in going from lean conditions towards an equivalence ration of 0.9. At equivalence ratios of 1 and above, the particulate emissions increase; however, they do not increase as significantly as the increase in particulate observed for the fuel oil at rich conditions. Moreover, the particulate emissions level off at very high equivalence ratios.

The trend in particulate emissions with equivalence ratio at rich conditions is highlighted somewhat by examining the unburned hydrocarbon emissions (HC) as shown in Figure 4.33. The Pine II oil has higher HC emissions than the Fuel Oil at all conditions, and the increase in HC emissions at rich conditions is much more significant for Pine II oil than Fuel Oil. This suggests that in moving towards richer conditions, pyrolysis oil becomes more difficult to oxidize than fuel oil.

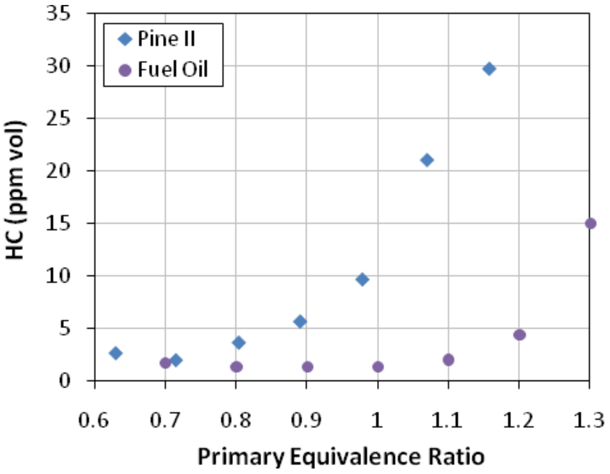

Figure 4.33 Unburned hydrocarbons vs. equivalence ratio for Pine II and Fuel Oil.

In comparing the PM and HC emissions between the two fuels, it is interesting to note that as the equivalence ratio is increased at rich conditions, HC's increase more rapidly for Pine II oil while the soot increases less rapidly. This suggests that at rich conditions, when oxidizer is scarce, pyrolysis oil fails to react, while fuel oil reacts strongly to produce soot.

An examination of the CO emissions versus equivalence ratio for both fuels yields very similar results. Both fuels have very low CO emissions at lean conditions, with the CO emissions increasing at almost identical rates above an equivalence ratio of 1. This trend is as expected since CO emissions will increase when insufficient oxidizer is present to convert fully to CO_2. The Pine II oil does show a slight reduction in the rate of CO increase with equivalence ratio relative to Fuel Oil. This reduction may be a result of the increased amounts of HC in the exhaust emissions, and hence a decrease in the oxidation of the fuel.

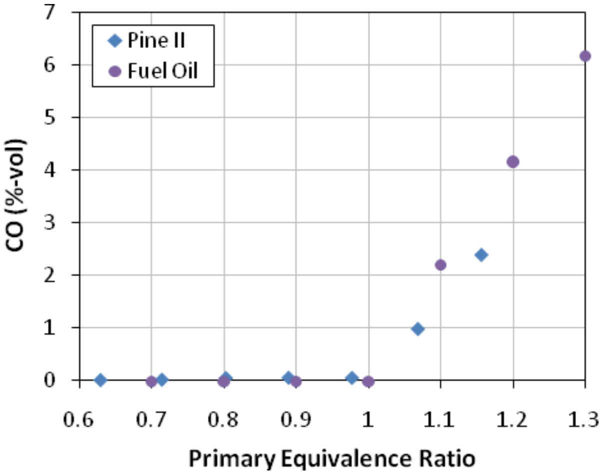

Figure 4.34 Carbon monoxide vs. equivalence ratio for Pine II and Fuel Oil.

The only trend in the rich portion of the particulate emissions for the Pine II oil that remains to be explained is that of the flattening of the curve at high equivalence ratios. One might expect that this would correspond with a significant increase in HC emissions, due to a failure of the fuel to react. However, this trend is not seen in the data. One possibility is that the HC emissions being measured (n-Hexane and Propane) are not detecting many of the unburned hydrocarbons in the pyrolysis oil.

At lean conditions, the trend in particulate is somewhat confounding. The low CO emissions at these conditions suggest that there is sufficient oxidizer present in the flame and that it is sufficiently well mixed with the fuel. As such, this suggests that the particulate being emitted under these conditions is difficult to oxidize. To further understand this trend, SEM images of the particulate have been collected, as discussed below.

4.3.2.2 Effect Equivalence Ratio – SEM Imaging

Scanning electron microscope images of exhaust particulate are shown in Figure 4.35. Given the costs of attaining SEM images and the inability to locate particulate at measurements below 5 mg/m^3, SEM images have only been displayed for a few key conditions.

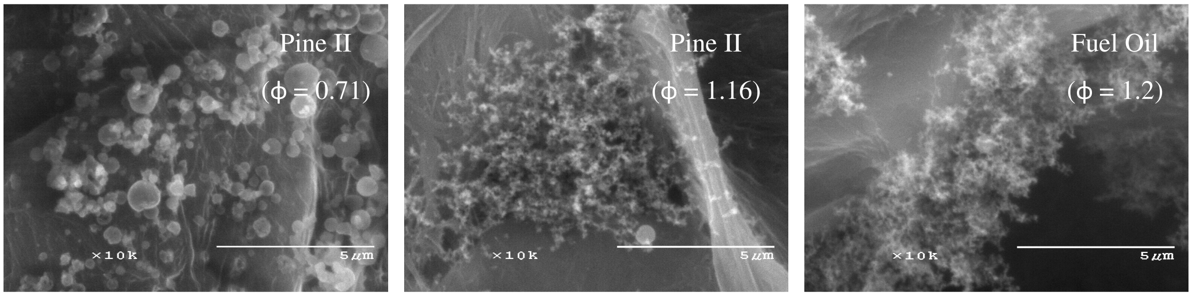

(a) **(b)** **(c)**

Figure 4.35 SEM images of particulate from Pine II oil at 0.71 (a) and 1.16 (b) equivalence ratios and Fuel Oil at 1.20 equivalence ratio (c).

At lean conditions (ϕ = 0.71), the Pine II oil particulate is dominated by cenospheres, with no indication of soot. The filter paper sample at this condition was brown in color, which agrees with the characteristics of cenospheres and filter color found in the pressure atomization studies. Scanning electron microscope images of the Pine II oil at other lean conditions were either not taken, or had particulate loadings which were too low to allow for detection of particulate. However, all of the filter paper samples at lean conditions at or below an equivalence ratio of 0.89 were brown in color, and as such, it is concluded that all of the particulate at these conditions is dominated by cenospheres. Therefore, the reduction of particulate emissions with increasing equivalence ratio under lean conditions is the result of a reduction of cenospheres in the exhaust emissions.

At an equivalence ratio of 0.98, the filter paper was a faint grayish color. As such, the increase in particulate from 0.89 to 0.98 equivalence ratio is the result of an increase in soot in the exhaust, not cenospheres.

An SEM image of the Pine II particulate at rich conditions ($\phi = 1.16$) shows that the particulate is dominated by soot. This agrees with the soot paper having a gray color. A comparison of this image to the particulate of Fuel Oil under rich conditions ($\phi = 1.2$) shows that the soot produced in the rich pyrolysis oil flame looks quite similar to that of the rich fuel oil flame. This further confirms that the rich Pine II particulate is indeed soot. The increase in particulate at rich conditions is therefore the result of an increase in soot. Indeed, all of the Pine II oil rich particulate filter samples were grey or black in color.

The SEM image of the Pine II particulate at 1.16 equivalence ratio does show one cenosphere. This is a significant reduction in cenospheres from the 0.71 equivalence ratio image, which further supports the conclusion that the reduction in particulate under lean conditions is the result of a reduction of cenospheres in the exhaust.

Another noteworthy comment of the cenospheres is that although there is a high concentration in the 0.71 equivalence ratio image, they are not packed together in large agglomerates as they were for the pressure-atomized condition at 0.7 equivalence ratio. This may suggest that the air atomization nozzle leads to improved atomization with regard to fuel dispersion. That is, if agglomeration occurs because fuel droplets are packed close together in a dense spray as has been suggested, then air atomization may be improving the droplet dispersion. This seems reasonable given that air atomization generally produces finer sprays and the introduction of air at the initiation of spray formation.

4.3.2.3 Effect of Equivalence Ratio – Visualization Methods

To better understand the reasons for the observed trends in exhaust particulate with equivalence ratio, flame visualization studies have been carried out, including high speed imaging and high power LII. Simple averages of the high speed images of the Fuel Oil flames are shown in Figure 4.36. As the equivalence ratio increases up to 1.2, the flame length and luminosity increases. The increase in luminosity is likely the result of an increase in the amount of soot in the flame. The increase in flame length is likely the result of reduced mass transfer between fuel and oxidizer, leading to slower burning rates. The decrease in flame luminosity from 1.2 to 1.3 equivalence ratio is likely the result of a decrease in flame temperature and, therefore, a reduction in radiative intensity from the soot in the flame. These speculations highlight the need for LII measurements of soot in the flame. At very rich conditions, a dark region is observed in the top of the flame, indicating a slightly lifted flame resulting from insufficient fuel/oxidizer mixing.

Simple averages of the high speed images of the Pine II flames are shown in Figure 4.37. As equivalence ratio is increased, the flame length increases as it did for Fuel Oil. However, as equivalence ratio increases, the flame luminosity decreases, which is the opposite of the trend observed with the Fuel Oil. Further, the change in luminosity for the Pine II oil trend is much less significant than the change in luminosity observed for fuel oil. This is very atypical and further highlights the need for investigation of soot in the flame through LII measurements. Once again, at high equivalence ratios the flame is slightly lifted.

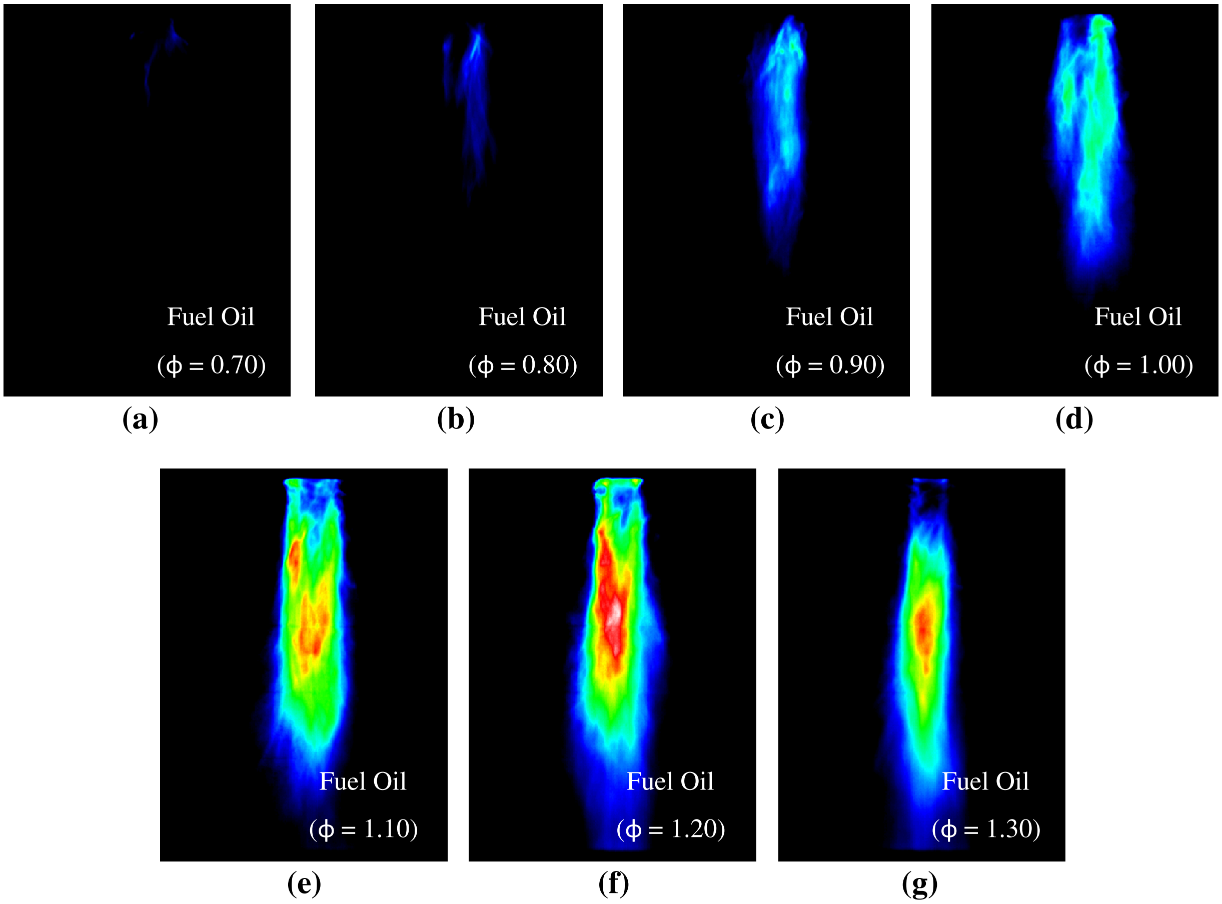

Figure 4.36 Simple average of high speed flame luminosity images of Fuel Oil flames at (a) ϕ = 0.7, (b) ϕ = 0.8, (c) ϕ = 0.9, (d), ϕ = 1.0, (e), ϕ = 1.1, (f) ϕ = 1.2, and (g) ϕ = 1.3.

In comparing the average flame luminosity images between the two fuels, it is interesting to note that the flame lengths are comparable, despite the significant difference in fuel flowrates. This suggests, that the flame size in the air-atomized flame is governed more by the thermal loading (i.e. both fuels operated at 19.2 kW) than by fuel flowrates. Therefore, this may make implementation of pyrolysis oil into existing turbine or boiler systems possible.

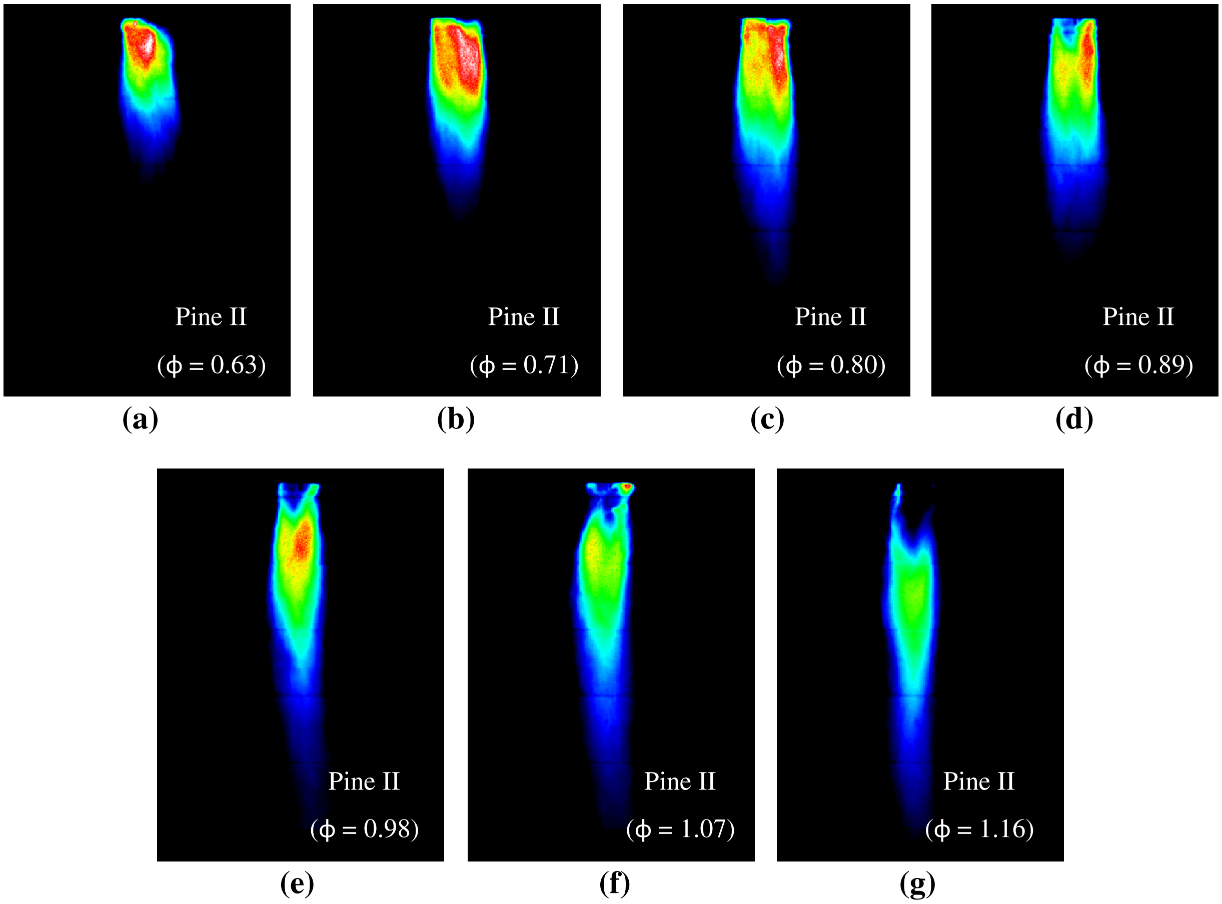

(a) **(b)** **(c)** **(d)**

(e) **(f)** **(g)**

Figure 4.37 Simple average of high speed flame luminosity images of Pine II flames at (a) ϕ = 0.63, (b) ϕ = 0.71, (c) ϕ = 0.80, (d), ϕ = 0.89, (e), ϕ = 0.98, (f) ϕ = 1.07, and (g) ϕ = 1.16.

Background subtracted simple averages of the LII images of the Fuel Oil flames are shown in Figure 4.38. During the Fuel Oil LII measurements, the beam profile was not uniform in the bottom of the chamber, such that the LII signal appears artificially low in this region. Further, a reflection was present which generated a high intensity line through the upper part of the images.

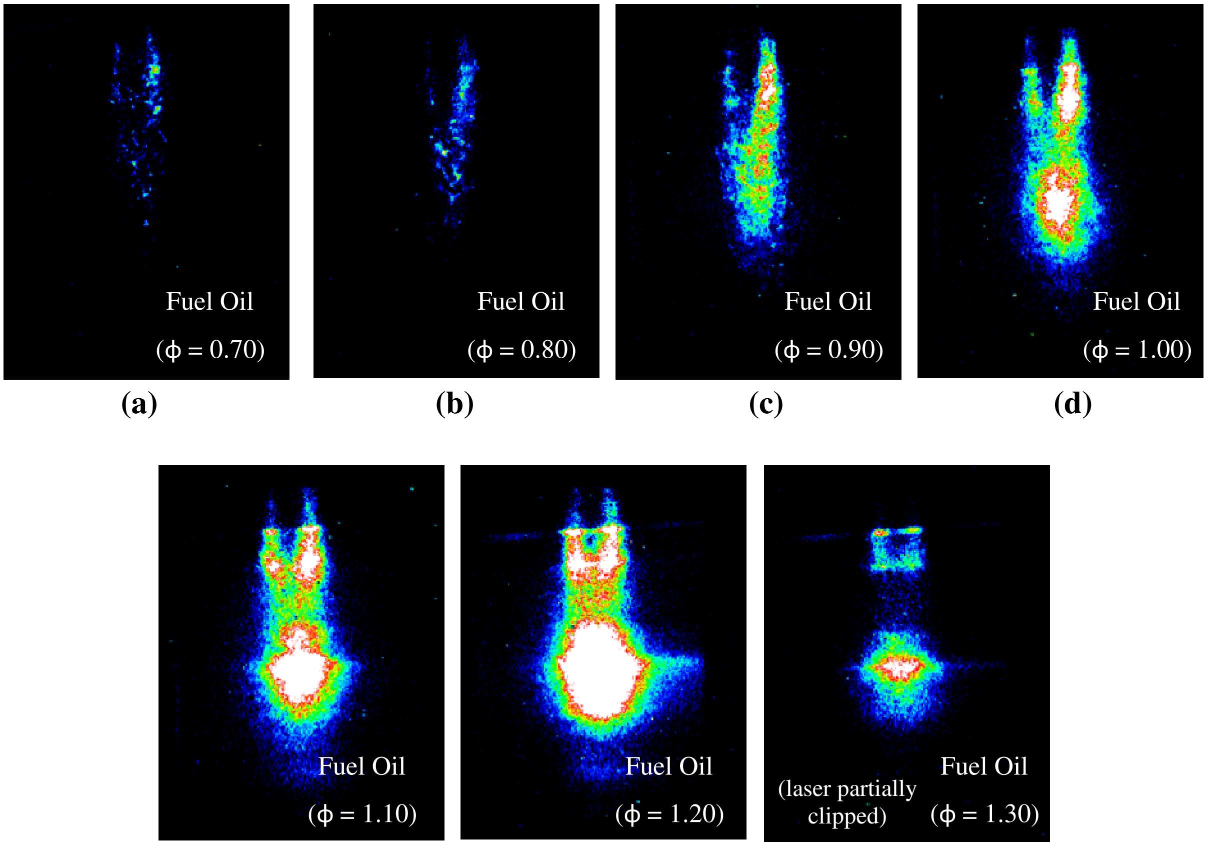

(a) **(b)** **(c)** **(d)**

(e) **(f)** **(g)**

Figure 4.38 Simple average of LII images of Fuel Oil flames at (a) ϕ = 0.7, (b) ϕ = 0.8, (c) ϕ = 0.9, (d), ϕ = 1.0, (e), ϕ = 1.1, (f) ϕ = 1.2, and (g) ϕ = 1.3.

As equivalence ratio increases, the amount of soot in the flame increases in agreement with the flame luminosity images. At lean conditions, the soot structures are well defined along the outer edges of the flame. At equivalence ratios greater than 1, the LII shows soot to exist lower in the flame, and outside of the luminous zone of the flame. This indicates that soot exists in lower temperature regions in the flame. This soot likely fails to oxidize due to the reduced temperatures and scarcity of oxidizer, leading to the high soot emissions at rich conditions. The decrease in LII signal from 1.2 to 1.3 equivalence ratio is likely the result of partial blockage of the laser during the LII measurement.

Background subtracted simple averages of the LII images of the Pine II flames are shown in Figure 4.39. The trend in LII image signal intensity agrees fairly well with the trend in particulate emissions in Figure 4.32; however, the minimum exhaust particulate occurs at an equivalence ratio of 0.89 while the minimum LII signal occurs at 0.98.

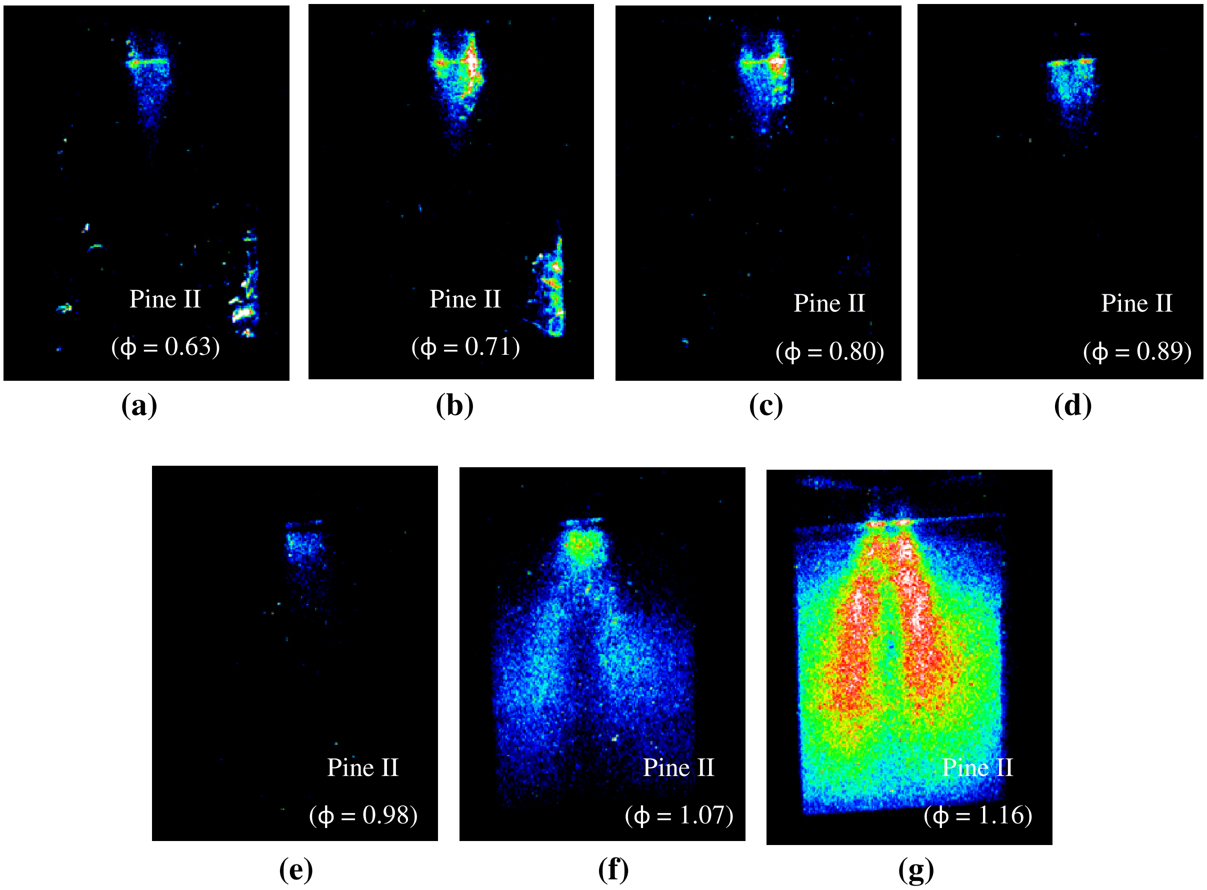

(a) **(b)** **(c)** **(d)**

(e) **(f)** **(g)**

Figure 4.39 Simple average of LII images of Pine II flames at (a) ϕ = 0.63, (b) ϕ = 0.71, (c) ϕ = 0.80, (d), ϕ = 0.89, (e), ϕ = 0.98, (f) ϕ = 1.07, and (g) ϕ = 1.16.

At rich conditions the LII signal is very widely distributed throughout the chamber, with two high intensity regions appearing along the outer edge of the flame. Under these conditions, there are no characteristic chain structures of soot as is normally seen. Rather, the soot appears to be widely produced throughout the combustion chamber, rather than grouping at locally fuel rich regions.

At lean conditions there is very little LII signal present in the flame zone. In this region, the soot is concentrated along the edges of the flame. It is interesting to note that as equivalence ratio is decreased from 0.98 to 0.71, the amount of soot in these regions increases. This is the opposite of the trend observed for fuel oil, and the opposite of what would be expected of most fuels (i.e. leaner conditions, less soot). One possible explanation for this trend is that as the equivalence ratio decreases, the pyrolysis oil volatizes and burns more rapidly due to the increased availability of oxygen, producing a short, sooty, high luminosity flame. The pyrolysis exhaust emissions of HC's and soot suggest that when conditions are locally rich, the Pine II fuel tends to fail to react, rather than produce soot. Therefore, at equivalence ratios close to unity, flame conditions are typically locally rich such that overall combustion rates are slowed. At lean conditions, the local conditions are less fuel rich, allowing for faster rates of combustion, higher flame temperatures, and higher rates of soot production. In droplet studies, Wornat et al. found burning ratesincrease with increasing oxygen content in the surrounding environment [67]. The confounding issue with this explanation is that the flame increases in soot content with increasing oxygen availability, which is opposite of what would be expected. It may be that by burning in a shorter, hotter flame, the fuel volatilizes rapidly releasing fuel vapors into hot regions within the flame which promote soot formation.

At very lean conditions (ϕ = 0.63 and ϕ = 0.71), large regions of LII signal can be seen at locations lower in the flame. This is likely the result of the sooty combustion of censospheres which are burned upon nearing the combustor walls, as has been discussed in previous sections. It is very interesting to note that this phenomenon is only observed during very lean combustion conditions. One possible explanation for this is that the flame length is very short for these conditions. As such, cenospheres have a very short residence time in the flame and are therefore not capable of burning completely before leaving the flame zone and instead, do not burn until reaching the hot combustor walls. This explanation also corroborates well with the observed increase in particulate emissions at very lean conditions.

Additional evidence of this can be seen by examining single images from the high speed flame luminosity images. Representative flame luminosity images are shown in Figure 4.40 for each of the equivalence ratios studied. In all of the flames, individual high intensity points can be seen at about the midpoint in the chamber, with structures which resemble that of cenosphere combustion. It is very interesting that the cenosphere combustion occurs at approximately the same location within the chamber. This suggests than for all cases, the cenospheres require approximately the same residence time before igniting and burning.

At equivalence ratios nearer and greater than 1, the cenospheres are observed to burn well within the limits of the visible flame. These signals have relatively low signal intensity in comparison to the surrounding flame. At these conditions, several cenospheres are observed to be burning within the flame.

At lean conditions where the flame is very short, cenosphere combustion occurs near the end of the flame. These signals have a relatively high intensity, especially in relation to the flame intensity in that region. At these conditions very few cenospheres are observed to be burning. As such, this further supports the suggestion that cenosphere emissions increase at lean conditions because the cenospheres experience a shorter residence time within the flame and, therefore, have insufficient time at elevated temperatures to fully burn.

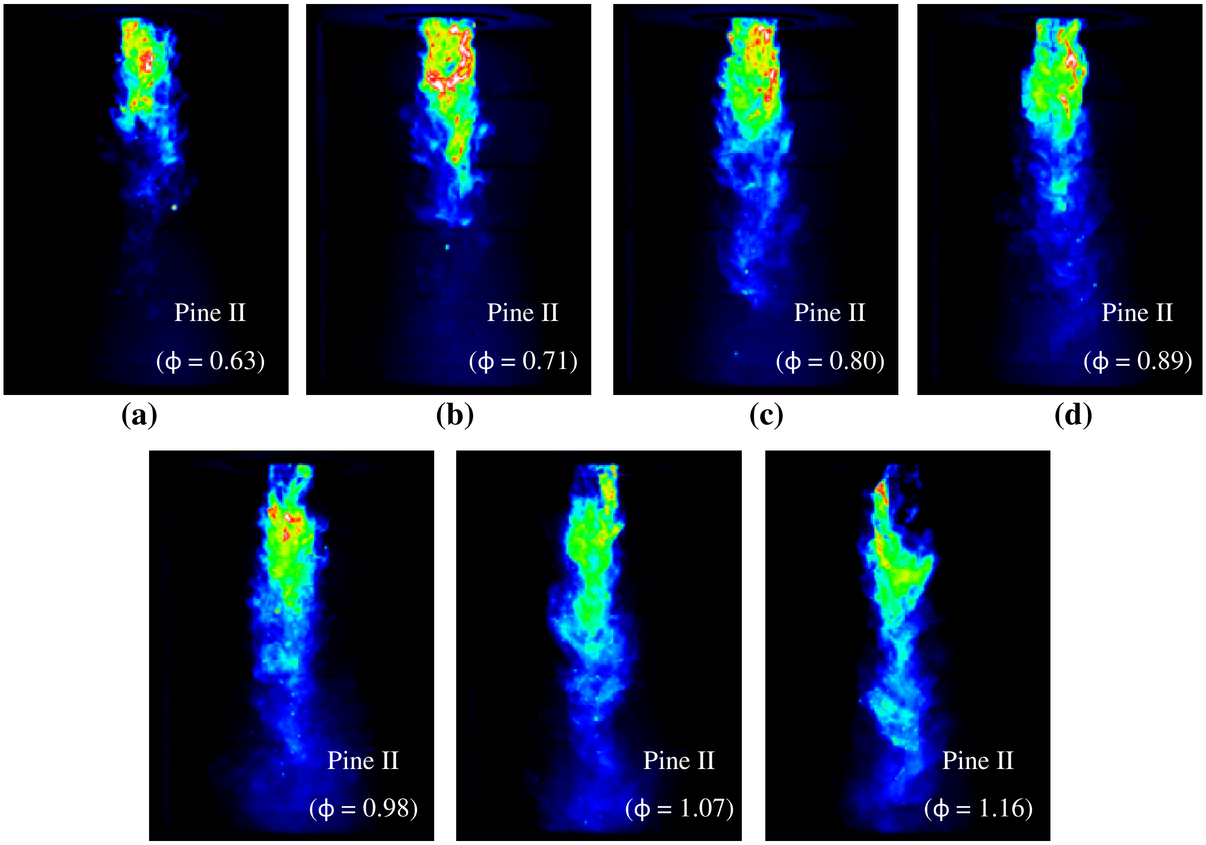

(a) **(b)** **(c)** **(d)**

(e) **(f)** **(g)**

Figure 4.40 Representative single-shot images of Pine II flame luminosity at (a) ϕ = 0.63, (b) ϕ = 0.71, (c) ϕ = 0.80, (d), ϕ = 0.89, (e), ϕ = 0.98, (f) ϕ = 1.07, and (g) ϕ = 1.16.

4.3.3 Effect of Atomization Air Flowrate

To investigate the effect of atomization air rate on pyrolysis oil combustion in air-atomized flames, Pine II oil and Fuel Oil have been studied at a thermal load of 19.2 kW.

This corresponds to volumetric fuel flowrates of 0.86 for the Pine II oil and 0.47 for the Fuel Oil. Because there is such a large difference in fuel flowrates, it is not possible to use the same nozzle size for each fuel. A Delevan Siphon Air nozzle size -8 was used for the Pine II oil and size -5 was used for the fuel oil. The Pine II tests were carried out at an equivalenc e ratio of 0.89 and the Fuel Oil tests were performed at an equivalence ratio of 1.0. During the Fuel Oil tests neither the fuel nor the combustion air was intentionally heated; however, the fuel temperature increased to 50 °C and the air temperature increased to 130 °C due to heat transfer from the chamber to the burner housing. The Pine II fuel was heated to 80 °C and the combustion air preheated to 300 °C for all tests.

Only one PI-MAX SB camera was available during these studies such that only one laser diagnostic measurement could be performed at a time. High power LII studies were performed with laser energy of 700 mJ/ pulse for Pine II and 425 mJ/ pulse for Fuel Oil mJ/ pulse. The high energy was required to visualize soot in the Pine II flames; however, for Fuel Oil the soot levels were so high that attempts at using 700 mJ/pulse led to saturation the ICCD camera. The Phantom high speed camera was available during these studies, such that high speed imaging of the flame luminosity was performed with the LII measurements. Carbon monoxide (CO) and HC emissions were measured with the Horiba MEXA-554J gas analyzer. Nitrogen oxide emissions were not measured. All emissions data presented represent athe average of at least three measurements. The error bars shown correspond to a 68% confidence interval of those measurements. If error bars are not displayed, then they are smaller than the data point symbol on the plot.

PDPA measurements were also performed to better understand the effect of atomization air rate on the fuel spray. Canola oil has been used in place of Pine II as a surrogate liquid for comparison in spray behavior. The canola was preheated to 120 °C during the spray experiments to generate kinematic viscosity and surface tension values in the liquid which are very similar to the pyrolysis oil properties at 80 °C, which is the fuel preheat temperature which has been used in the combustion studies. A detailed discussion of the viscosity and surface tension measurements of the canola can be found in the appendixes. All PDPA measurements were made at a distance of 20 mm below the nozzle exit, which corresponded approximately to the distance from the nozzle where the flame was stabilized.

4.3.3.1 Effect of Atomization Air Flowrate – Exhaust Emissions

The exhaust particulate emissions as a function of atomization air rate are shown in Figure 4.41. For all Fuel Oil conditions the particulate readings were zero within the uncertainty of the instrument. For the Pine II oil, the particulates decreased with increasing atomization air rate. In fact, at the highest atomization air flowrate, the particulates were zero, within the limits of the instrument.

Unburned hydrocarbon emissions are shown in Figure 4.42, and display trends very similar to that in the particulate measurements. Given that the resolution of the instrument was 1 ppm, the Fuel Oil emissions were very close to zero for all conditions. The Pine II oil shows a decrease in HC emissions with increasing atomization air rate, with near zero emissions at 42 slpm.

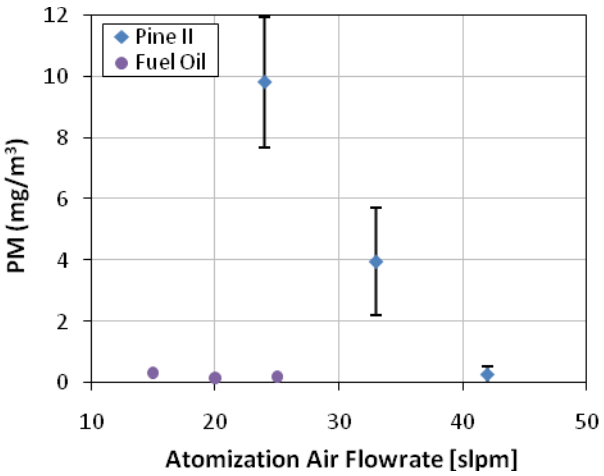

Figure 4.41 Particulate concentration vs. atomization air flowrate for PineII and Fuel Oil.

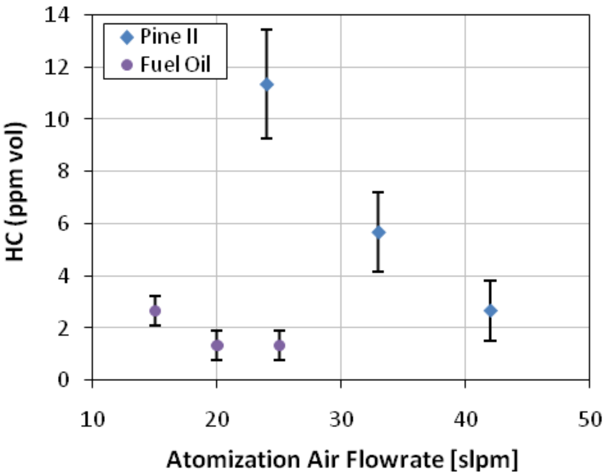

Figure 4.42 Unburned hydrocarbons vs. atomization air flowrate for Pine II and Fuel Oil.

Carbon monoxide emissions are shown in Figure 4.43. Once again, the trends appear very similar to those seen in the PM and HC results. The Fuel Oil readings are zero within the measurement uncertainty of the device for all conditions. The Pine II oil shows a decrease in CO emissions with increasing atomization air rate. At 42 slpm, the CO emissions are zero within the resolution of the instrument.

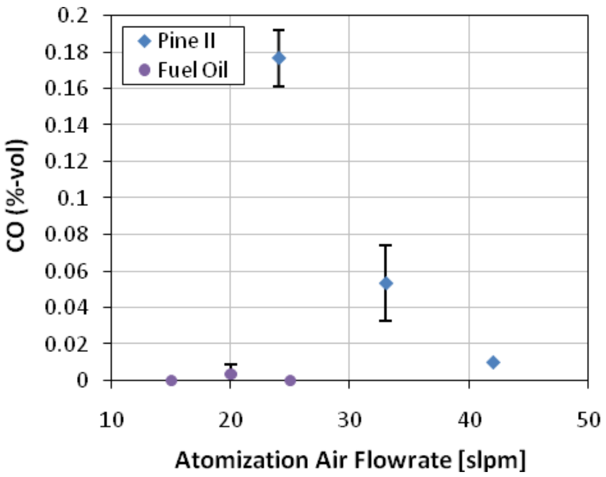

Figure 4.43 Carbon monoxide vs. atomization air flowrate for Pine II and Fuel Oil.

4.3.3.2 Effect of Atomization Air Flowrate – SEM Imaging

The particulate readings at 33 and 42 slpm were too low to allow the particulate structures to be detected with SEM imaging. However, for all particulate samples of Pine II oil, the filter paper sample was brown, indicating censopheres rather than soot.

At 24 slpm particulate could be imaged as shown in Figure 4.44. This particulate shows several cenospheres gathered together in large agglomerates. This is different than the particulate observed at 33 slpm and 0.71 equivalence ratio shown in Figure 4.35. The cenospheres in this sample were not bound together in large aggregates as those shown below. Rather, the particulate at 24 slpm appears more like the cenospheres observed for pressure atomization in Figure 4.21. Therefore, a reduction in atomization air flowrate appears to reduce the degree of separation of the cenospheres in the spray and flame, resulting in more agglomerated structures.

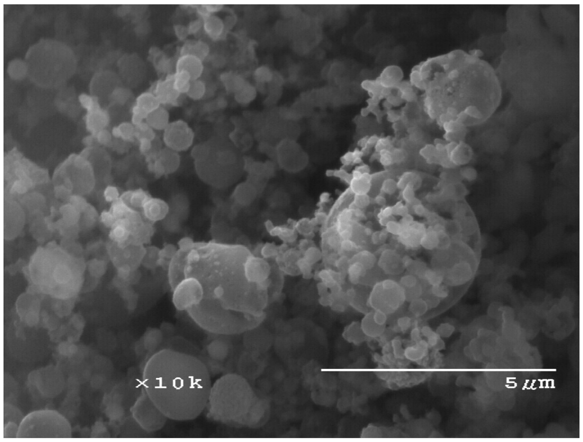

Figure 4.44 SEM image of Pine II particulate at 42 slpm atomization air flowrate.

4.3.3.3 Effect of Atomization Air Flowrate – Visualization Methods

The visual appearance of the flame changes rather significantly as the atomization air flowrate is adjusted, as shown in Figure 4.45. At lower atomization air rates the flame is shorter, and more yellow in color, indicating sooty combustion. At high atomization air rates, the flame is longer and narrower, with its color dominated by the potassium in the flame.

The changes in the Fuel Oil flame with changing atomization air rate are similar to those found for Pine II oil as shown in Figure 4.46. At the lowest atomization air rate the flame is very luminous and sooty. As the atomization air rate is increased, the luminosity of the flame decreases and the flame color becomes blue.

The trends seen in the color camera images are also seen in averages of the high speed images for Pine II flames as shown in Figure 4.47. As atomization air rate increases, the luminosity and width of the flame decrease. Thus, although the flame emissions are reduced to their lowest levels at the high atomization air rates, this condition has very low radiative heat transfer such that this operating condition is not favored for operation in radiative boilers.

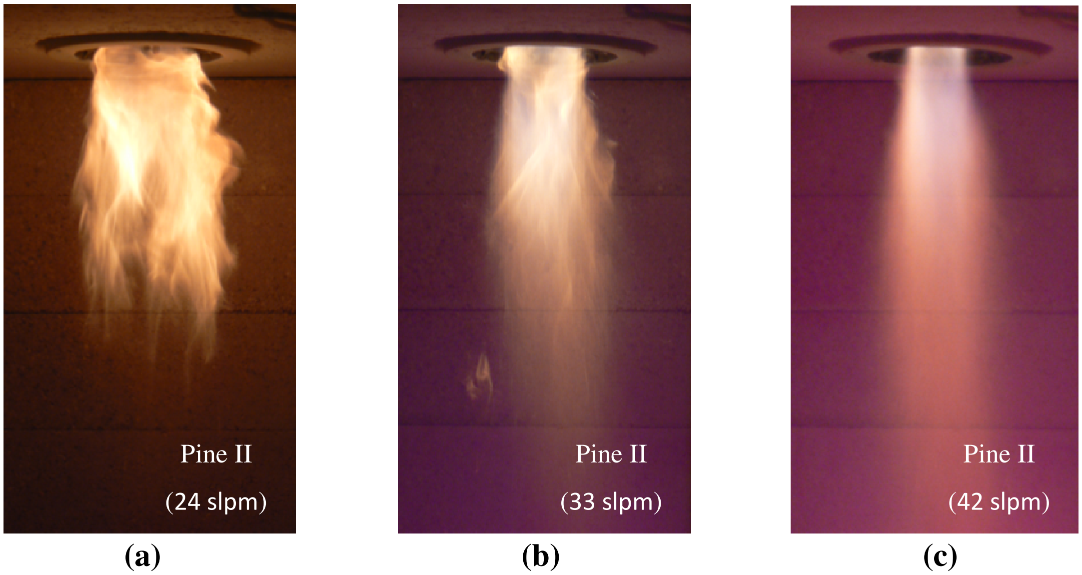

(a) (b) (c)

Figure 4.45 Color camera images of Pine II flames at varying atomization air flowrates of (a) 24 slpm, (b) 33 slpm, and (c) 42 slpm.

Although the luminosity and flame color provide good indicators of soot levels in the flame, these images do not well distinguish between soot concentration and soot temperature. Simple averages of LII images for the Fuel Oil flames is shown in Figure 4.49. At 15 slpm the LII signal from the soot is so strong that it fills the combustion chamber, scattering off the walls and into the camera. At 25 slpm, the LII level is very low, appearing only along the edges of the flame. Thus, atomization has a dramatic effect on the amount of soot in the fuel oil flame. Given that soot arises in nonpremixed flames as a result of mass transfer limitations, this suggests that atomization air rate is having a dramatic influence on the mass transfer rates of fuel and oxidizer in the flame. It is also interesting to note that this significant variation in soot in the flame has no effect on the amount of soot in the exhaust.

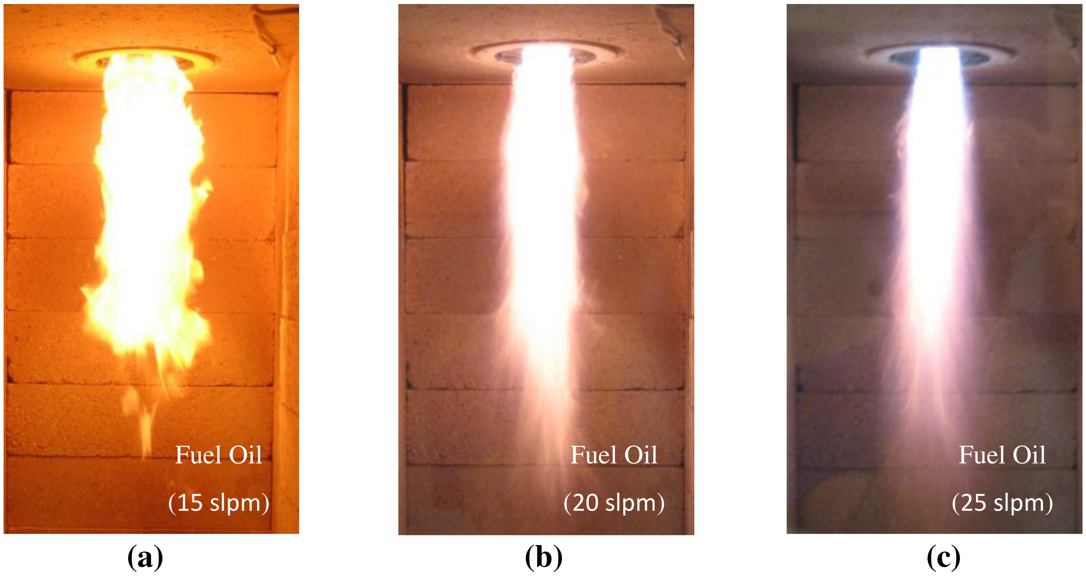

(a) **(b)** **(c)**

Figure 4.46 Color camera images of Fuel Oil flames at varying atomization air flowrates of (a) 15 slpm, (b) 20 slpm, and (c) 25 slpm.

Once again, the trends observed in the color camera images of the Fuel Oil flames are repeated in the simple averages of the high speed images, as shown with a false color scale in Figure 4.48. As atomization air rate increases, the luminosity and width of the flame decrease. It is interesting to note that the change in luminosity for the Fuel Oil flames is much more significant than the change in luminosity observed for the Pine II flames.

Simple averages of LII images for the Pine II flames is shown in Figure 4.50. Once again, as the atomization air rate increases, the amount of soot in the flame is reduced. However, this reduction is not nearly as significant as that observed for fuel oil.

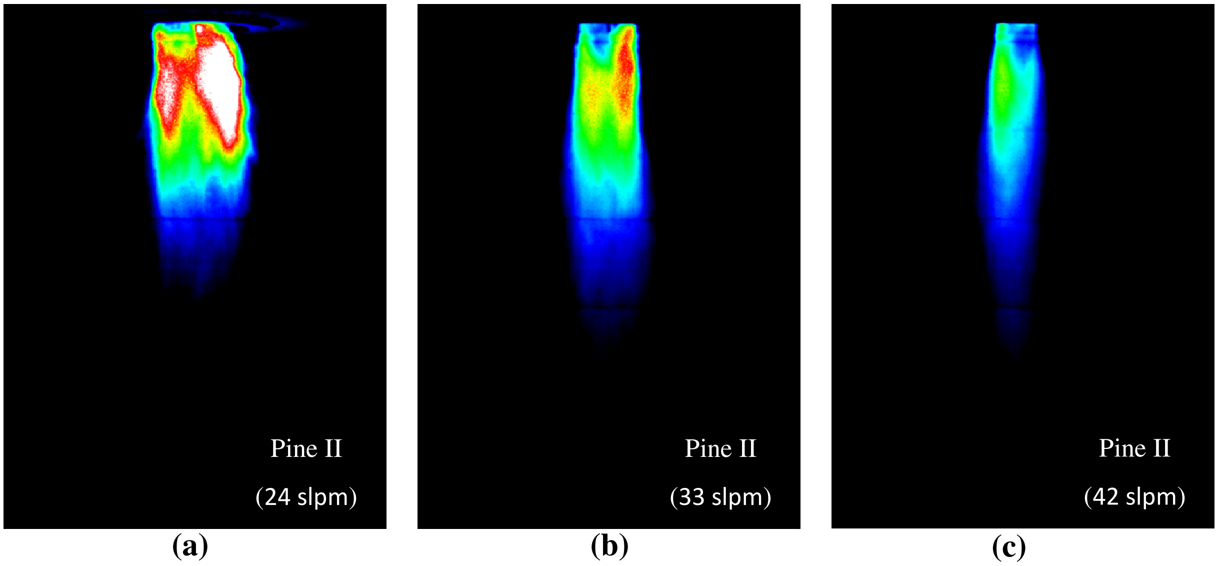

(a) **(b)** **(c)**

Figure 4.47 Simple average of Pine II flame luminosity images at varying atomization air flowrates of (a) 24 slpm, (b) 33 slpm, and (c) 42 slpm.

The LII results suggest that mass transfer rates are increased in flames with higher atomization air flowrates. This increase in mass transfer may be a result of smaller droplet sizes or increased spray momentum, which serves to increase evaporation and mixing rates. To understand which of these phenomena is more important in the fuel sprays, PDPA studies have been performed.

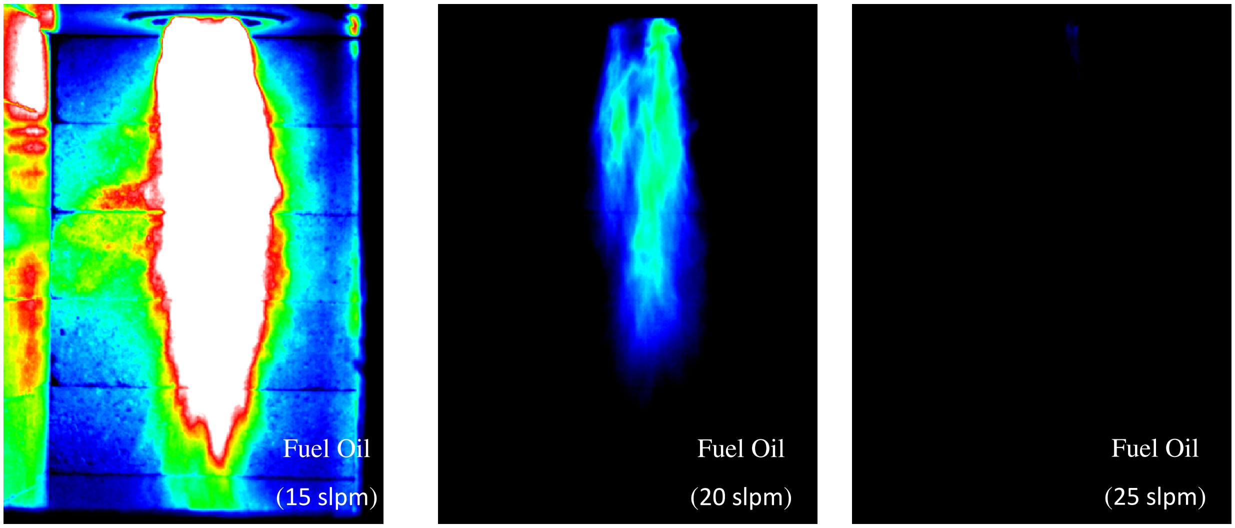

(a) **(b)** **(c)**

Figure 4.48 Simple average Fuel Oil flame luminosity images at varying atomization air flowrates of (a) 15 slpm, (b) 20 slpm, and (c) 25 slpm.

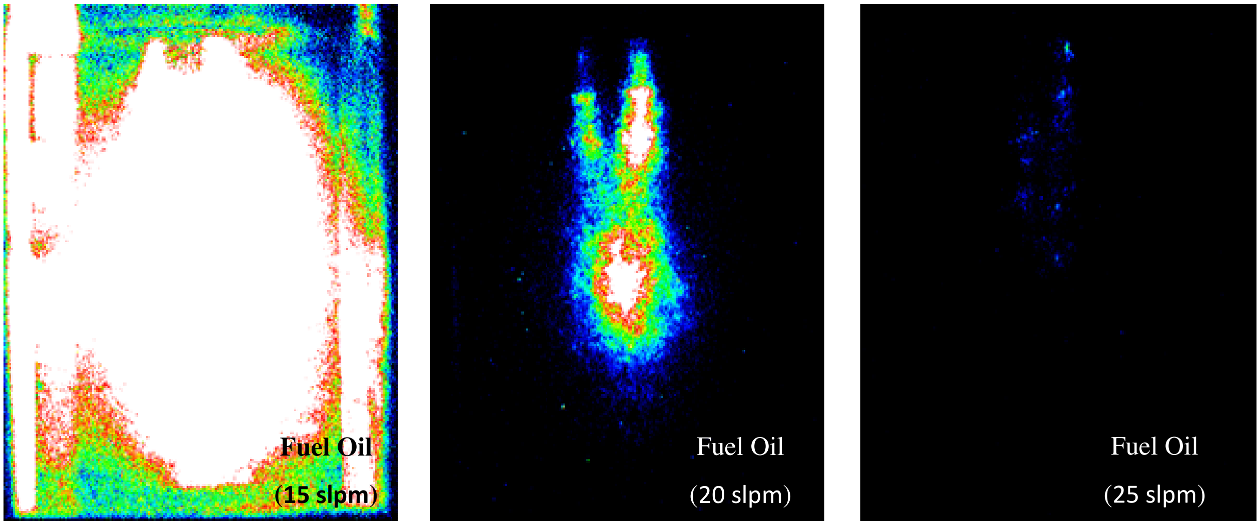

(a) **(b)** **(c)**

Figure 4.49 Simple averages of LII images of Fuel Oil flames at varying atomization air flowrates of (a) 15 slpm, (b) 25 slpm, and (c) 30 slpm.

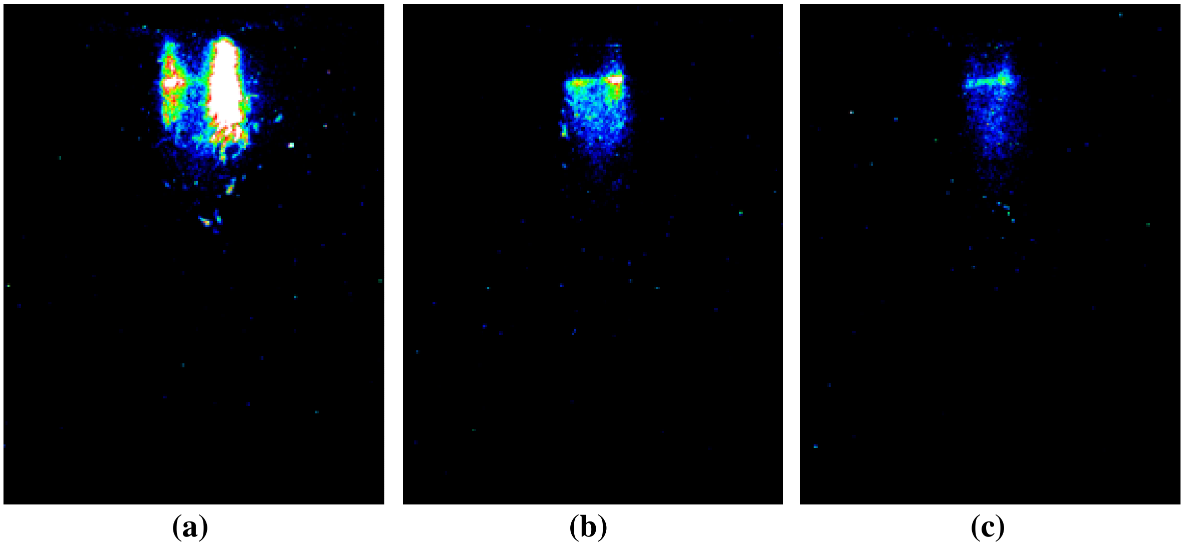
(a) (b) (c)

Figure 4.50 Simple averages of LII images of Pine II flames at varying atomization air flowrates of (a) 24 slpm, (b) 33 slpm, and (c) 42 slpm.

4.3.3.4 Effect of Atomization Air Flowrate – PDPA

The Sauter mean diameter (SMD) of the canola oil spray as a function of the radial distance from the spray center is shown in Figure 4.51. In decreasing from 24 to 15 slpm, the effect of atomization air rate on droplet diameter is significant throughout the entire spray; however, all of the Pine II combustion tests were performed at 24 slpm and above. From 24 to 42 slpm there is very little change in the SMD in the central core of the spray. However, further from the center of the spray, the change in droplet diameter is more significant. As such, the increase in mass transfer rates with increasing atomization air rate, may be a reduction of droplet size in the outer edges of the spray.

The mean velocity of the canola oil spray as a function of distance from the nozzle center is shown in Figure 4.52. Once again, from 15 to 24 slpm, there is a significant change in the spray characteristics; however, all Pine II combustion tests were performed at 24 slpm and above. From 24 to 42 slpm, the velocity at the center of the spray does increase significantly. However, beyond this, the mean spray velocity varies little as a function of atomization air flowrate.

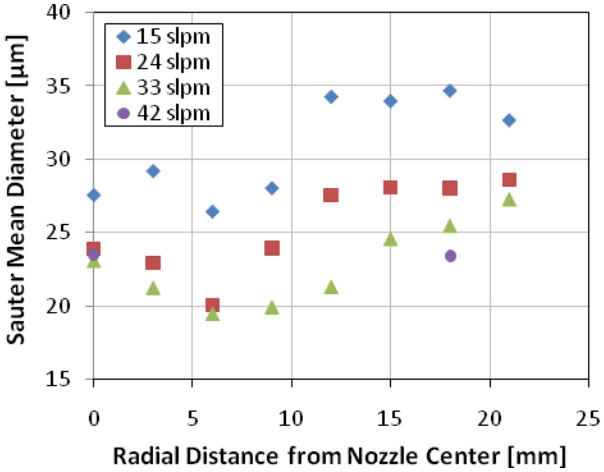

Figure 4.51 Sauter mean diameter vs. radial distance of Canola Oil sprays at 120 °C for varying atomization air flowrates.

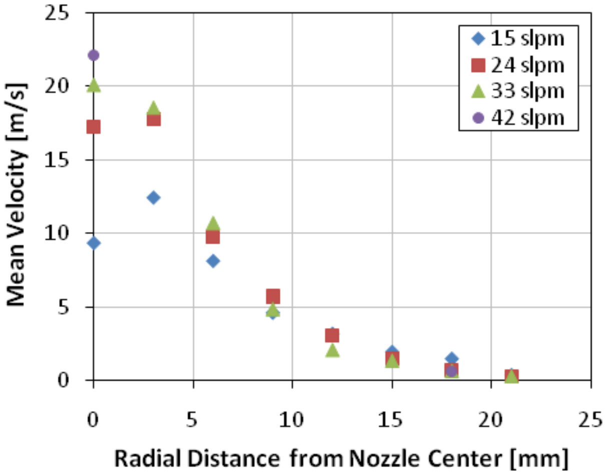

Figure 4.52 Mean velocity vs. radial distance of Canola Oil sprays at 120 °C (ν = 4.6 cSt) for varying atomization air flowrates.

The results of the PDPA studies suggest that increasing the atomization air rate improves mass transfer rates in two ways. It increases the jet momentum in the middle of the spray, improving mixing and reducing the size of the droplet diameters near the outer edges of the spray.

In addition to affecting mass transfer rates, it seems likely that increasing atomization air flowrate will aid in the combustion of cenospheres. By reducing the droplet diameter, the increase in atomization air flowrate should aid in reducing the size of the cenospheres formed during combustion. Smaller cenospheres should volatilize and increase in temperature more rapidly, increasing their burning rates. Further, the increased velocity in the core of the spray may help improve spray dispersion such that agglomeration of cenospheres is reduced.

4.3.4 Effect of Water Content

To investigate the effect of water content on pyrolysis oil combustion, water has been added to the Pine II oil to produce batches which contain 24.5 and 26 wt-% water content (up from the original 23% water content). Attempts were made to study changes in water content which were greater than this; however, attempts at burning oils with water contents of 27% and higher resulted in very poor ignition and unstable combustion. In fact, even the 26% water content oil was difficult to ignite, requiring combustion air preheat temperatures of 200 °C to prevent blow-off. As such, the range of water contents studied is quite narrow.

All of the fuels have been burned at a thermal load of 19.2 kW, resulting in fuel flowrates of 0.86, 0.88, and 0.90 gph for the 23, 24.5 and 26% water content fuels respectively. A Delevan Siphon Air nozzle size -8 was used and the fuels were preheated to 80 °C for all studies. Equivalence ratio, atomization air flowrate, and combustion air preheat temperature were varied and exhaust emissions measured. Carbon monoxide (CO) and HC emissions were measured with the Horiba MEXA-554J gas analyzer. Nitrogen oxide emissions were not measured. All emissions data presented represent the average of at least three measurements. The error bars shown correspond to a 68% confidence interval of those measurements. If error bars are not displayed, then they are smaller than the data point symbol.

4.3.4.1 Effect of Water Content - Equivalence Ratio Variation

Equivalence ratio was varied by adjusting the combustion air flowrate. All fuels were sprayed with an atomization air flowrate of 33 slpm. The combustion air was preheated to 300 °C for all tests.

The particulate emissions are shown in Figure 4.53. The 24.5 and 26% water content fuels follow same characteristic trend as that shown for the Pine II oil. There does not appear to be a significant trend in PM with water content at any of the equivalence ratios studied except at an equivalence ratio of 1.16. At this condition, the 24.5 water content oil had higher PM emissions. Considering that this is the middle water content oil, and that there were no significant differences at any other equivalence ratios, it seems likely that this data point is an outlier, perhaps resulting in flame instability during those measurements.

The unburned hydrocarbon emissions are shown in Figure 4.54. Once again, the 24.5 and 26% water content oils show the same trends as those seen in the baseline Pine II oil.

Further, there does not appear to be a strong trend in HC emissions with water content at any equivalence ratio except 1.16. At this condition the 24.5% water content oil has the highest HC emissions, which corroborates well with the PM emissions.

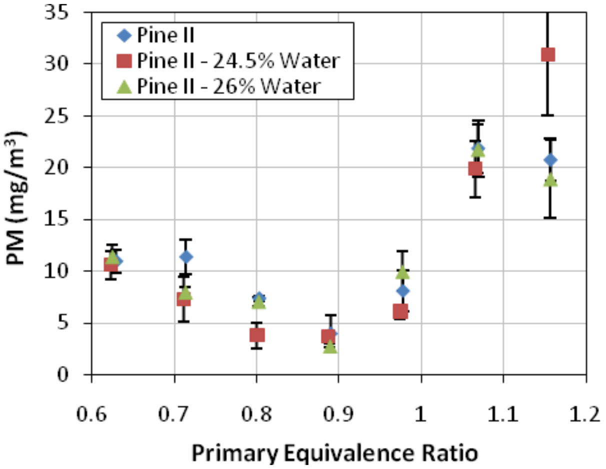

Figure 4.53 Particulate concentration vs. equivalence ratio for Pine II fuels of varying water content.

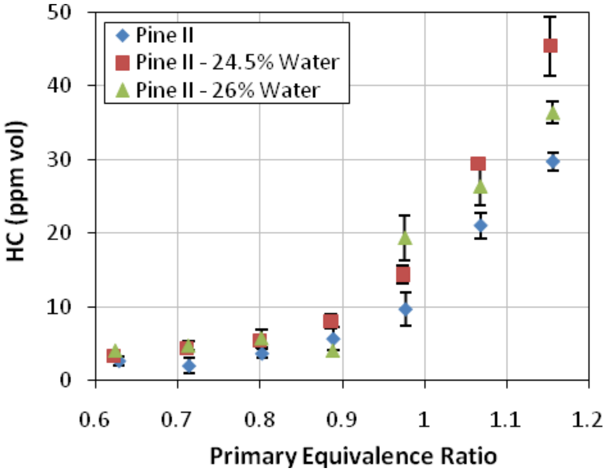

Figure 4.54 Unburned hydrocarbons vs. equivalence ratio for Pine II fuels of varying water content.

The carbon monoxide emissions are shown in Figure 4.55. Once again, the 24.5 and 26% water content oils show the same trends as those seen in the baseline Pine II oil. Further, there does not appear to be a strong trend in CO emissions with water content at any equivalence ratio.

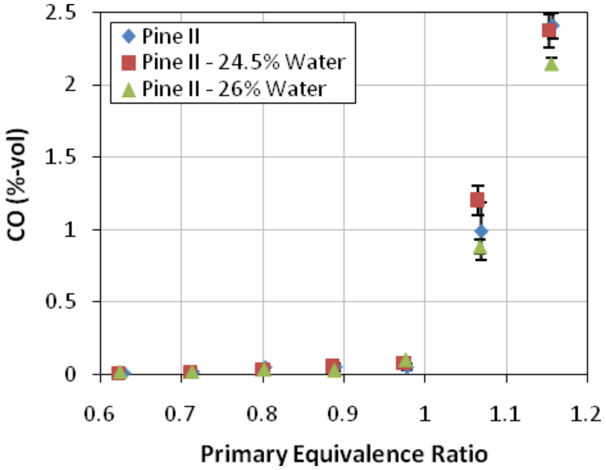

Figure 4.55 Carbon monoxide vs. equivalence ratio for Pine II fuels of varying water content.

4.3.4.2 Effect of Water Content - Atomization Air Rate Variation

The atomization air flowrate has been varied from 24 to 42 slpm for each water content fuel. All fuels were burned at an equivalence ratio of 0.89. The combustion air was preheated to 300 °C for all tests.

The particulate emissions are shown in Figure 4.56. The 24.5 and 26% water content fuels follow same characteristic trend as that shown for the Pine II oil from 33 to 42 slpm. However, in decreasing from 33 to 24 slpm, the baseline Pine II oil shows a significant increase in emissions, while the 24.5 and 26% water content oils do not show such an increase. This may be an indication that water is indeed having an effect on the PM emissions; however, this may also be an outlier in the data.

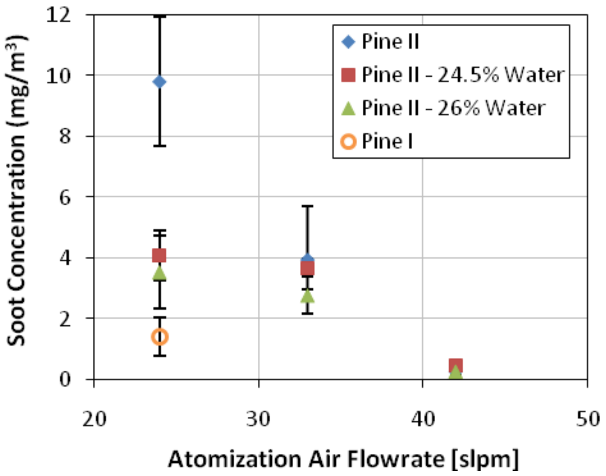

Figure 4.56 Particulate concentration vs. atomization air flowrate for Pine II fuels of varying water content.

To further highlight the possibility of this data point being an outlier, the PM measurement from the Pine I oil has been overlaid on this plot. This measurement was taken at very a similar equivalence ratio and combustion air preheat temperature. The Pine I oil has 22% water content, which is lower than the 23% water content of the Pine II oil; however, it yields an even lower particulate reading than the 24.5 or 26% water content oils. As such, it does not appear that there is a strong trend with water content and rather, that there is significant variation in the data at 24 slpm atomization air rate.

Further evidence of this data point being an outlier is shown in the unburned hydrocarbon measurements in Figure 4.57. Typically the HC trends have followed the PM trends; however, they do not do so for this data point. Rather, the HC values are very similar at all atomization air flowrates for each water content oil.

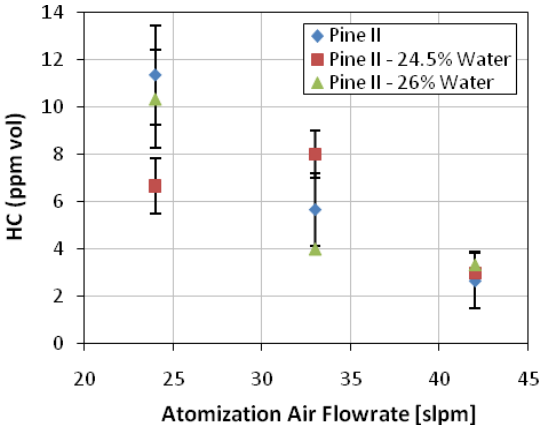

Figure 4.57 Unburned hydrocarbons vs. atomization air flowrate for Pine II fuels of varying water content.

The carbon monoxide emissions are shown in Figure 4.58. At 33 and 42 slpm there does not appear to be a trend in CO emissions with water content. At 24 slpm the 24.5% water content oil has lower CO emissions than the other data points. However, this may once again be an outlier in the data, and suggest that the variability in combustion behavior at 24 slpm atomization air flowrate is high.

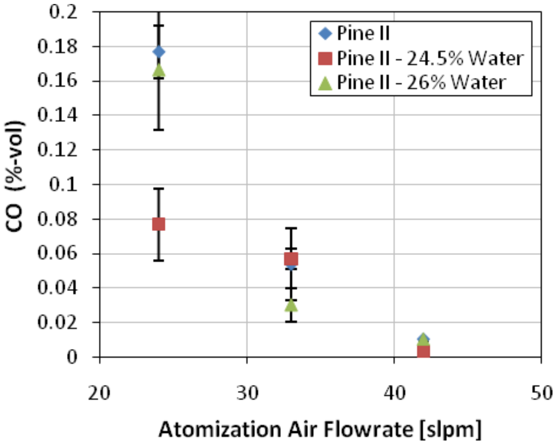

Figure 4.58 Carbon monoxide vs. atomization air flowrate for Pine II fuels of varying water content.

4.3.4.3 Effect of Water Content - Combustion Air Preheat Variation

The combustion air preheat temperature has been varied from 100 to 300 °C for the 23 and 24.5% water content oils and from 200 to 400 °C for the 26% water content oils. As has been discussed, the 26% water content oil was not stable at a preheat temperature of 100 degrees and therefore, it could not be effectively investigated. The combustion air preheat temperature has been studied in conjunction with water content as it has been suspected combustion air preheat may help to compensate for the slight reduction in flame temperature caused by increasing the water content of the fuel. All conditions were operated at an equivalence ratio of 0.89 and with an atomization air flowrate of 33 slpm.

The particulate emissions are shown in Figure 4.59. Neither combustion air temperature nor water content appears to have an effect on PM emissions.

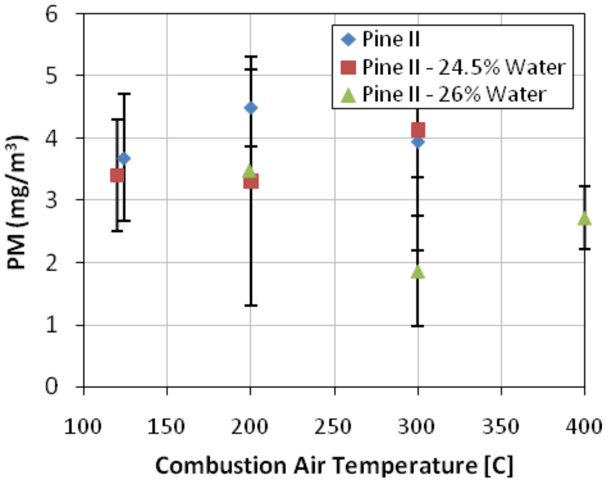

Figure 4.59 Particulate concentration vs. combustion air temperature for Pine II fuels of varying water content.

The unburned hydrocarbon emissions are shown in Figure 4.60. Neither combustion air temperature nor water content appears to have strong effects on HC emissions.

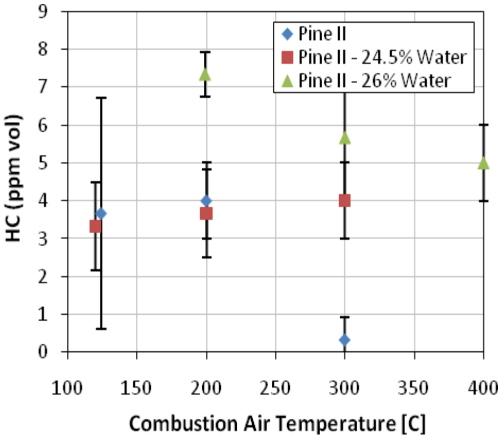

Figure 4.60 Unburned hydrocarbons vs. combustion air temperature for Pine II fuels of varying water content.

The carbon monoxide emissions are shown in Figure 4.61. Neither combustion air temperature nor water content appears to have strong effects on HC emissions.

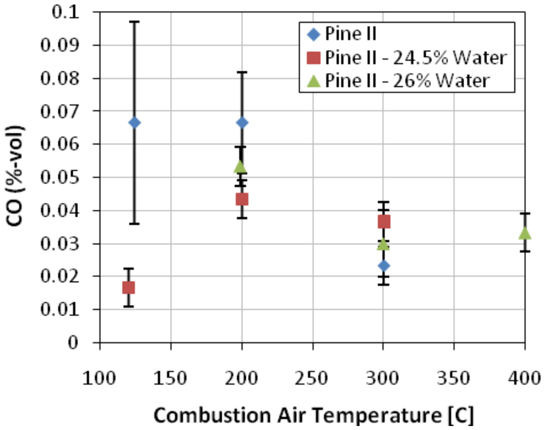

Figure 4.61 Carbon monoxide vs. combustion air temperature for Pine II fuels of varying water content.

CHAPTER 5. SUMMARY AND FUTURE WORK

A swirl-stabilized, optically accessible combustor has been developed to allow for the investigation of the combustion characteristics of biomass derived fast pyrolysis oils. Although particulate emissions have typically been found to be of concern in pyrolysis oil combustion, the burner developed in this research has proven capable of achieving particulate emissions which are below detectable levels. This is an important finding, given the challenges associated with nozzle clogging and heat losses for burners of this scale.

Ignition and flame stability have proven to be challenges in pyrolysis oil combustion, in agreement with the findings of other researchers. Flammability limits have been found to be narrower than fuel oil, with 1.16 being the highest equivalence ratio achievable while still maintaining stable combustion.

Potassium and Sodium were found to have very strong chemiluminescence in the pyrolysis oil flames. The Potassium signal was strong enough that it dominated the flame color of air atomization flames operating at moderate to high atomization air flowrates. Along with the chemiluminescence of these inorganic species; however, significant amounts of ash were found to collect on burner surfaces during pyrolysis oil combustion.

Pyrolysis oil has been shown to have a lower flame luminosity than fuel oil, regardless of whether pressure or air atomization is employed. This is a result of a reduction in sooting tendency of the pyrolysis oil fuels in comparison to fuel oil. This may be a significant deterrent in using pyrolysis oil in radiative boilers. The luminosity of the flame can be increased by utilizing pressure atomization; however, this comes at the cost of a substantial increase in particulate emissions. Hence, additional strategies such as staged combustion with other fuels may be required under these conditions.

The level of stability and turbulence in the air-atomized pyrolysis oil flames was greatly improved over that of the pressure-atomized flames. Further, the air atomization nozzles allowed for greater control over the spray and, ultimately, of emissions characteristics from the flame. However, clogging and coking arose as significant challenges for both nozzle types. It may be possible to intermittently operate with fuel oil to clear the fuel nozzle passages.

In the pressure atomization studies, it was found that soot can be a significant contribution to particulate emissions when the flame is poorly stabilized and operating near stoichiometric conditions. However, all of the studies of well stabilized pyrolysis oil flames at lean conditions have shown that particulate emissions are a result of failed combustion of heavy fuel residues, referred to as cenospheres, rather than soot or solid char remains in the fuel. Moreover, this research has shown that the sooting tendency of pyrolysis oil is quite low in comparison to fuel oil.

The failure of cenospheres to burn in the flame is somewhat contrary to the findings of Wornat et al. and Shaddix et al. who found that the burning rates of pyrolysis oil were comparable to that of light fuel oil in single droplet combustion studies.[65, 67]. In these single droplet combustion studies, external heating is supplied to burn the fuel, with uniform chamber temperatures. However, in a spray flame, the flame is supported by heat transfer from the hot combustion products to the incoming reactants. For pyrolysis oil, the flame is stabilized by the combustion of high volatility compounds in the fuel. This research has shown that the volatile fuel species can be expended long before the heavier components have been fully oxidized. As such, the low volatility compounds can exit the hot flame zone, further reducing their burning rates and allowing them to be emitted as stack solids. Single droplet combustion studies do not capture the nature of fuel heating and mixing rates present in a spray flame, and as such these studies may result in shorter burning times than those which occur in spray flames.

Apart from issue of burning rates, there is some agreement between the observation of cenospheres outside of the flame zone and findings in the single droplet combustion studies. Wornat et al. notes that the first stage of droplet combustion is that of the combustion of the light volatility compounds [67]. Further, she notes that this combustion stage is marked by an abrupt end in combustion, followed by droplet swelling and microexplosion without burning. Thus, the discontinuity in the combustion event may be what allows the cenospheres to exit the flame zone.

Coupled with the tendency of low volatility fuel to pass beyond the flame zone is a very interesting trend in pyrolysis oil combustion with regard to equivalence ratio. As conditions become leaner the flame length shortens and the particulate emissions increase. The increased availability of oxygen in the lean flames generates more rapid combustion of the high volatility fuel compounds resulting in a shorter flame length. However, high speed imaging of the flame shows that the cenospheres in the flame do not experience the same increase in burning rates such that they likely exit the flame zone having not yet fully oxidized. Given this phenomenon, particulate emissions have been found to be minimized near stoichiometric conditions, where temperatures are high and where there is sufficient oxygen to burn the fuel, but where reduced mass transfer rates between the fuel and oxidizer result in slower combustion rates of the volatile compounds and longer flame lengths. This provides the cenospheres with a longer flame residence time, allowing them to oxidize more completely before leaving the flame.

Given the impact of equivalence ratio on pyrolysis oil combustion, particulate emissions may be most effectively reduced by using staged combustion. By burning the pyrolysis oil at initially rich conditions and then introducing secondary combustion air, the flame length could be increased, allowing for longer residence times of the cenospheres in the flame. Care should need to be taken not to introduce secondary air too far downstream or with temperatures that are too cool such that they quench any soot that may be in the flame. However, given the tendency of pyrolysis oil to fail to react under rich conditions, rather than produce soot, this may not be a critical concern.

Air atomization has also been shown to significantly reduce particulate emissions, with particulate readings reaching zero at high atomization air flowrates. Phase Doppler particle analysis (PDPA) has shown that increasing the atomization air flowrate reduces the droplet diameter along the outer edges of the spray and increases the spray velocity along the centerline of the spray. The reduction of droplet diameter likely leads to smaller cenospheres which burn more rapidly, yielding the low particulate emissions. Further, the increase in spray velocity likely aids in the dispersion of droplets, reducing the formation of large cenosphere agglomerates which have slower burning rates. Some evidence of this is seen in the SEM images of the cenospheres for low and moderate atomization air flowrates. At lower atomization air flowrates, the cenospheres appear in agglomerate structures whereas at moderate atomization air flowrates the cenospheres are found individually in the exhaust. Particulate matter collected during pressure atomization studies also reveals cenosphere aggregates, further suggesting a reduction in atomization performance of the pressure atomization nozzles.

Investigations into the effects of chemical composition on pyrolysis oil combustion have yielded few significant findings. An increase from 23 to 26% water content in the Pine II oil has shown no change in exhaust emissions or flame structure. The only effect of the water addition was a reduction in the ignition quality of the oil, with water contents of 27% and higher leading to highly unstable flames.

In comparing the Pine I and Corn Fraction oils, there were almost no differences in flame structure and particulate emissions, despite the many differences in there chemical compositions. The differences in the chemical composition of the fuels was evident in the fuel fluorescence images, with the Corn Fraction oil showing very strong fluoresce in the fuel spray and cenospheres. The only significant difference between these oils was with respect to NOx emissions, which were much higher for the Corn Fraction oil as a result of the high nitrogen content in that fuel.

As such, the key chemical species which lead to cenosphere production, and eventually particulate emissions, have not been identified. However, a few variables in the fuel properties can be ruled out as having a significant effect. The fixed carbon increases from 15 to 21% from Pine I to Corn Fraction, indicating that a 30% increase in fixed carbon does not significantly affect cenospheres. The water content increases from 22 to 26.5% and the heating value decreases from 18.7 to 16.6 MJ/kg such that this change does not appear to be significant factor in cenosphere burnout rates. However, this change may be obscured by the fact that the Corn Fraction oil has higher O/C and O/H ratios, such that its air-fuel ratio is lower, giving it a relatively high adiabatic flame temperature. From Pine I to Corn Fraction, the adiabatic flame temperature only decreases by 44 K, such that this may be a better indicator of the burning rates in the fuel. Nonetheless, this does suggest that a 44 K change in adiabatic flame temperature is not significant enough to affect the flame characteristics substantially.

Identification of the fuel components which lead to cenosphere formation during combustion would be an excellent area for further investigation. As was done with water in this research, various known components could be added to the oil in known quantities to quantify the effects of various chemical species on cenosphere production and oxidation. This may be not be feasible to do in a spray flame, and as such, it may be more appropriate to use an intermediate test, such as the Conradson carbon residue test. For heavy fuel oils, this test serves as the best method for characterizing the tendency of the fuel to form cenospheres. It would first be necessary to indeed show a correlation between the Conradson carbon number and cenosphere tendency. However, if this relationship were established, it would lead to a relatively simple test for determining if a particular oil will result in cenosphere production, simply by performing Conradson carbon residue tests.

In addition to the chemical characteristics of cenospheres, it is also of interest to gain a better understanding of their physical characteristics. This research has shown that cenospheres can be more than an order of magnitude larger than the original droplet size. This is likely a combined effect of cenosphere swelling and agglomeration. It would be of interest to study pyrolysis oil combustion using an ultrasonic nozzle to produce a very uniform spray. This would allow for cenosphere size to be studied as a function of droplet diameter. Further, by varying the degree of spray dispersion, cenosphere agglomeration could be investigated.

APPENDIX A. ORIFICE FLOWMETER DESIGN AND CALIBRATION

An orifice plate flowmeter operates by correlating the pressure difference across a small opening to the flowrate through that opening as shown in Figure A.1 [79]. The pressure difference is generated both by the acceleration of the fluid through the orifice and from frictional losses. The flowrate (Q) is typically related to the pressure drop (ΔP) in the following equation

$$Q = C_f A_o \sqrt{\frac{2\Delta P}{\rho}} \quad [79] \qquad \text{A.1}$$

where A_o is the area of the orifice, ρ is the density of the fluid, and C_f is the calibration coefficient for the flowmeter.

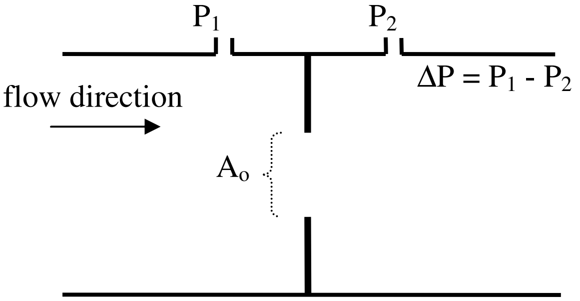

Figure A.1 Orifice flowmeter.

The exhaust flowing through the orifice flowmeter in this combustion apparatus was always high enough above the saturation point of the water that it behaves as an ideal gas.

Treating the fluid in the orifice flowmeter as an ideal gas yields the following relationship between the calibration coefficient and the mass flowrate ($\dot{m}$)

$$C_f = \frac{\dot{m}}{A_0}\sqrt{\frac{R\,T}{2\,\Delta P\,M\,P_{abs}}} \qquad \text{A.2}$$

where R is the ideal gas constant, T is the absolute temperature, P_{abs} is the absolute pressure, and M is the molecular weight of the gas.

Equation A.2 is the calibration equation that has been used in designing the orifice flowmeter in this research. Calibrations have been carried out by setting a constant mass flow through the device with an Alicat mass flow controller and measuring the pressure drop across the device. The Alicat mass flow controller was used to measure the local atmospheric pressure. A K-type thermocouple was installed in the flowmeter to correct for temperature variations. Two Omega PX653differential pressure transducers were used with ranges of 0 to 1 -inH2O and 0 to 10 -inH2O respectively, both having accuracies of ±0.25% of full-scale. The use of two pressure transducers allowed for the device to be calibrated for a very large range of flowrates, while maintaining a high degree of accuracy.

The main thrust of the development of the orifice flowmeter was in developing a design which yielded a constant calibration coefficient over a wide range of operating parameters. This was not a simple task, given the tortuous flow path leading up to the orifice flowmeter. Typically, a straight run of pipe is placed in front of the flowmeter for a distance of several pipe diameters; however, for this particular application, space constraints did not allow for this [80]. As such, several alterations of orifice diameter and orientation of the device were studied, to find a design which provides a constant calibration coefficient.

All calibrations of the flowmeter have been carried out with the flowmeter positioned in the exhaust ducting as it was during use, to eliminate the effects of any geometric dependencies in the calibration. Nearly all of the calibrations were carried out with air near standard conditions. The results of these calibrations for the final orifice flowmeter design are shown in Figure A.2 as a function of Reynolds number (based on the duct diameter). Over this range of Reynolds number, the average coefficient is 0.79 ± 2%, based on a 95% confidence interval.

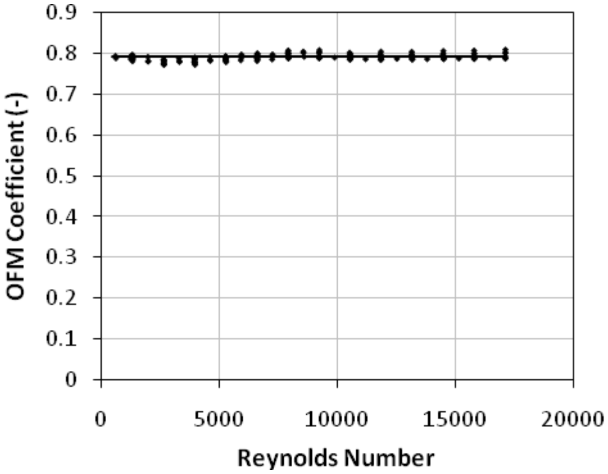

Figure A.2 Orifice flowmeter calibration coefficient versus Reynolds number.

Although the orifice flowmeter shows consistent behavior with regard to Reynolds number in Figure A.2, this calibration curve does not account for all possible variables which might affect the calibration constant, since the temperature, ambient pressure, and molecular weight of the gas were held constant during these calibrations. For the sake of this application, the ambient pressure is not likely to vary significantly. The molecular weight of the exhaust could potentially be an issue; however, the difference is less than 0.5%, even at rich conditions. Thus, the final remaining variable which must be calibrated against is that of temperature. The calibration of the flowmeter versus temperature was shown in Figure A.3. Once again, the calibration constant of the orifice flowmeter was very steady over a wide range of conditions.

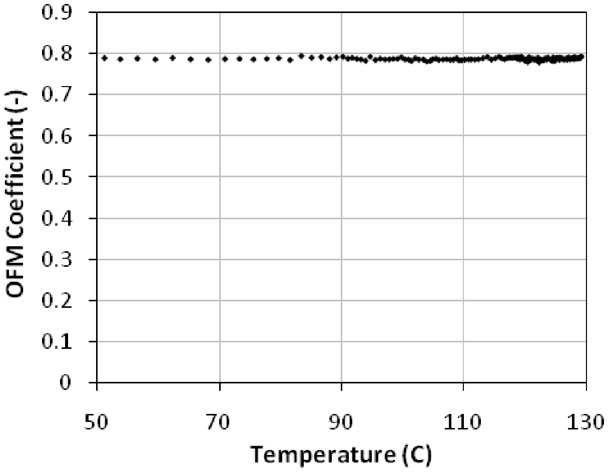

Figure A.3 Orifice flowmeter calibration coefficient versus temperature.

APPENDIX B. VISCOSITY MEASUREMENT RESULTS

B.1 Pine II Oil Viscosity Results

The results of the Pine II oil viscosity measurements are discussed in detail below. The results of the Pine I oil viscosity measurements are very similar both in magnitude and characteristic to the Pine II oil, such they are not discussed in detail. Rather, the results of the Pine I oil viscosity are summarized in Table 3.6.

Above 40 °C, the Pine II pyrolysis oil samples behaved as a Newtonian fluid, with linear shear stress versus shear rate relationships as shown in Figure B.1. Moreover, the measurements of samples showed very high repeatability, with 95% confidence interval error bars which are too small to be seen in Figure B.1.

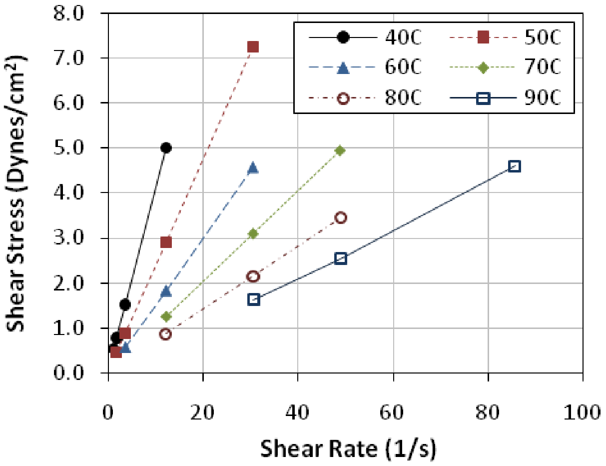

Figure B.1 Shear stress vs. shear rate for Pine I pyrolysis oil.

At 25 °C, the Pine II oil samples showed more variability in measurement as well as a slight deviation from Newtonian behavior as is shown in Figure B.2. The variability in these measurements is likely attributed to slight variations in the samples pulled from the overall batch, rather than the measurement device itself, as measurements repeated in different tests of the same oil showed the same results. These variations become less significant at higher temperatures as is evident by the high repeatability shown in Figure B.1.

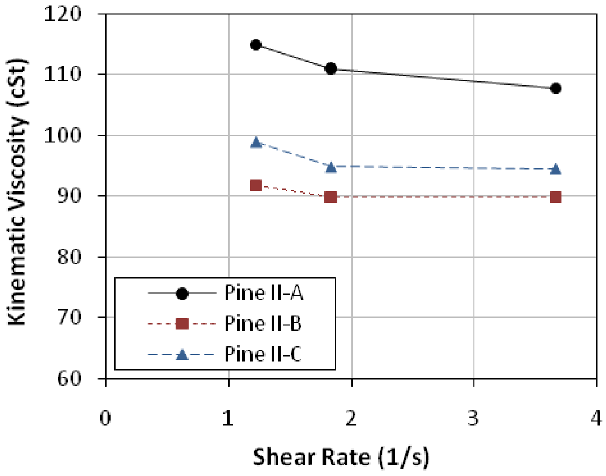

Figure B.2 Kinematic viscosity vs. shear rate for Pine II samples.

Further, notice that the oil is slightly non-Newtonian at 25 °C. The oil undergoes shear thinning, which is an advantage for pumping and spraying. Although there are only 3 data points, it appears that at higher shear rates the rate of viscosity change is less.

A plot of kinematic viscosity versus temperature for the Pine II oil is shown in Figure B.3. Many pure fluids exhibit a viscosity-temperature relationship which is an exponential decay function; however, the Pine II oil does not appear to have such behavior as shown in

Figure B.3. Given this, linear interpolation will be used to estimate the viscosity of the oil at temperatures between measurement points.

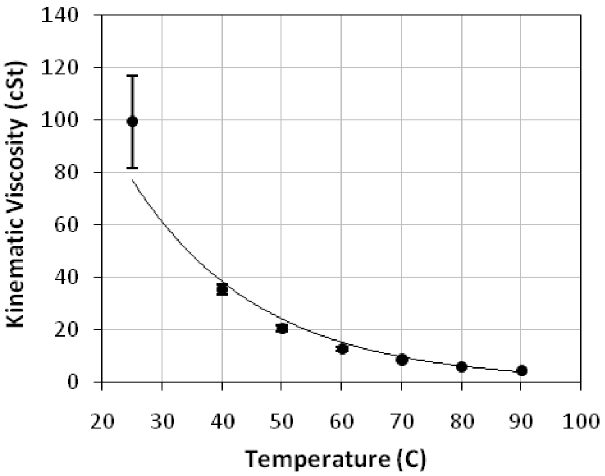

Figure B.3 Kinematic viscosity vs. temperature of Pine I oil.

The water content in the Pine I oil is approximately 23%. Additional water was added to Pine I oil to produce mixtures containing 24.5% and 26% water. The viscosity versus temperature profiles are shown in Figure B.4. This figure shows temperature to have a more significant impact on viscosity than changes in water content, especially at elevated temperatures. If the temperature is varied ±2 °C (the uncertainty of the fuel temperature control in this research) at 80 °C, the corresponding change in viscosity is roughly the same as that between the 23% and 26% water content oil.

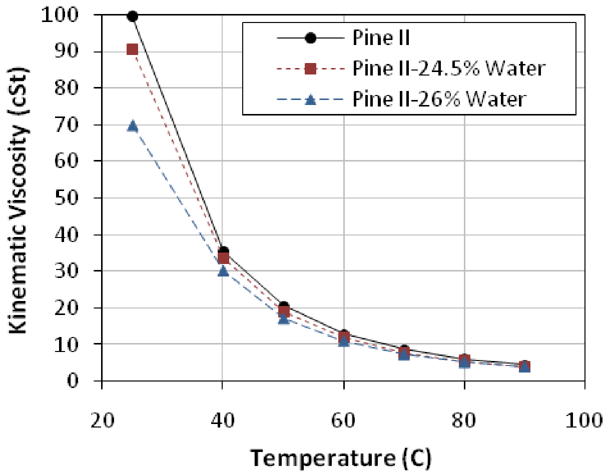

Figure B.4 Kinematic viscosity vs. temperature for Pine I oils of varying water content.

B.2 Corn Oil Viscosity Results

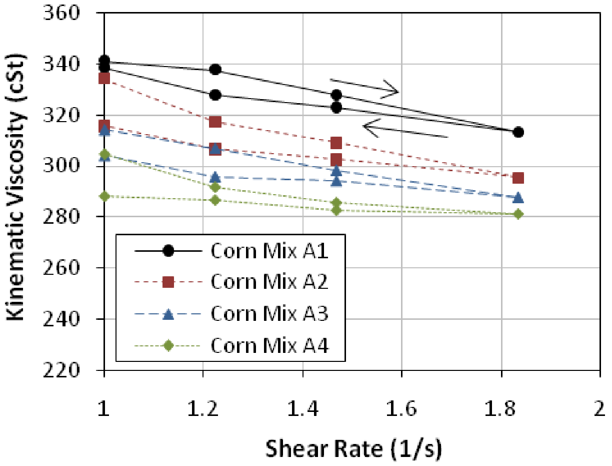

Figure B.5 Kinematic viscosity vs. shear rate for Corn Mix oil sample A low shear rates at 25 °C.

- A1, A2, A3, A4 indicates the order in which the measurements were made

- The arrows further indicate the order in which measurements were made
- Time between measurements was approximately 10 seconds
- The oil is shear thinning
- It is also thixotropic, with viscosity decreasing over time

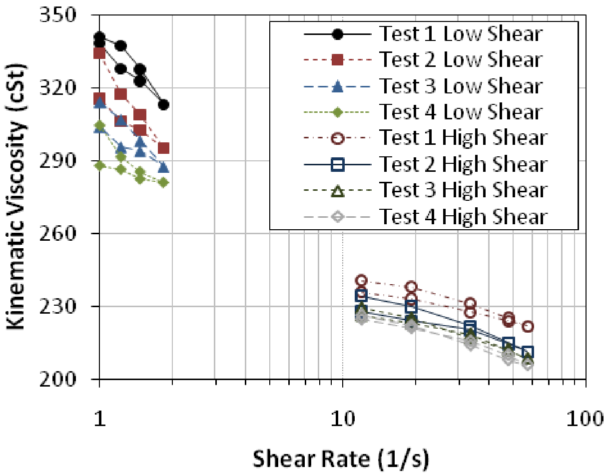

Figure B.6 Kinematic viscosity vs. shear rate for Corn Mix oil sample A at both high and low shear rates at 25 °C.

- Test numbers indicate the order of the measurements
- Once again, the order of the tests was from high viscosity to lower
- The samples are found to be both shear thinning and thixotropic
- This is true for both low and high shear rates

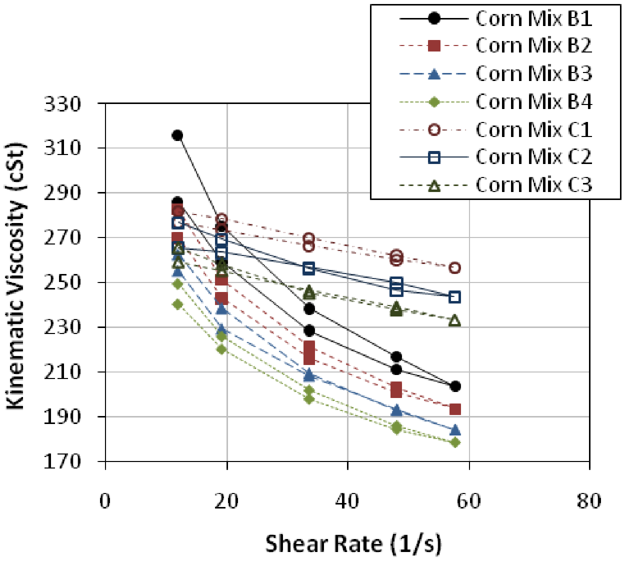

Figure B.7 Kinematic viscosity vs. shear rate for Corn Mix oil samples B and C at high shear rates at 25 °C.

- Test number indicate the order of the measurements
- Once again, the order of the tests was from high viscosity to lower
- Both samples are found to be both shear thinning and thixotropic
- Sample C is even more shear thinning and more thixotropic

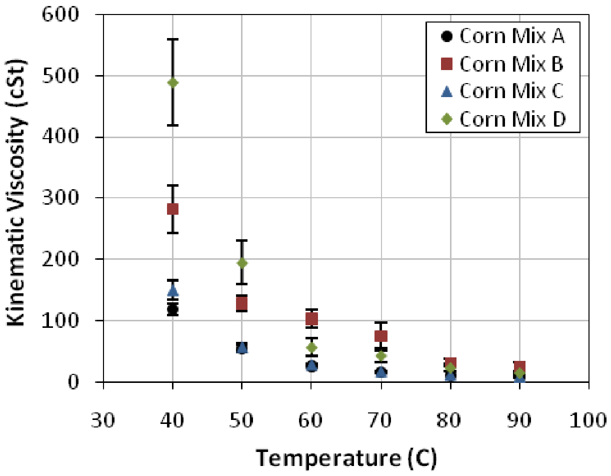

Figure B.8 Average kinematic viscosity vs. temperature for Corn Mix oil samples A, B, C, D.

- The large error bars at low temperatures are due to Non-Newtonian behavior
- Sample D has a more pronounced temperature dependence than others

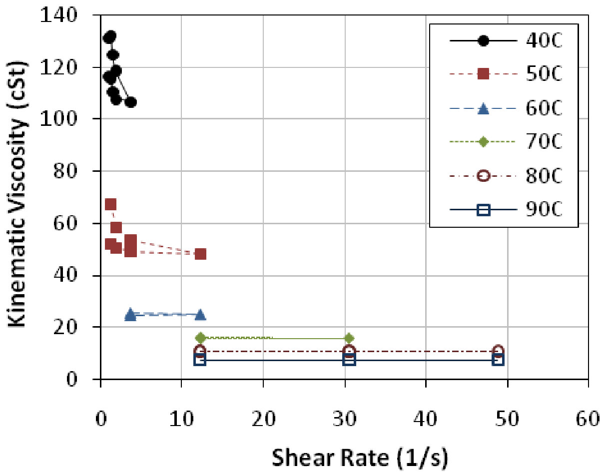

Figure B.9 Average kinematic viscosity vs. shear rate for Corn Mix oil samples A.

- Oil is Newtonian above 60 °C

B.3 Fuel Oil Viscosity Results

- Fuel oil only tested up to 60 °C for safety reasons
- Also did not test fuel oil with high preheat temperatures because the viscosities are already low enough to achieve good sprays

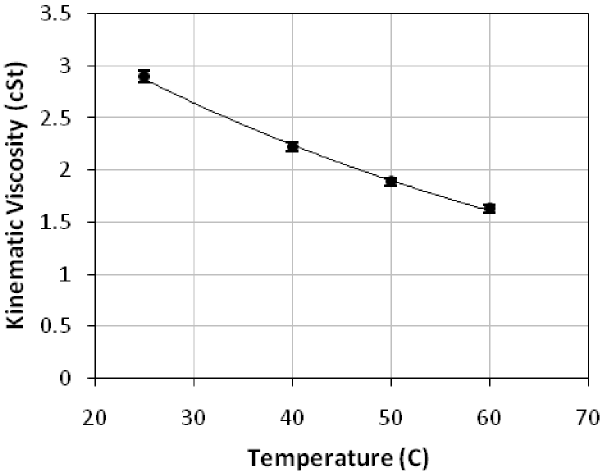

Figure B.10 Kinematic viscosity vs. temperature for fuel oil.

- Error bars are plot, but are so small they are not visible
- The data fits an exponential decay function very nicely

B.4 Canola Oil Viscosity Results

- Canola oil tested because it is being studied as a surrogate to py oil for spray studies

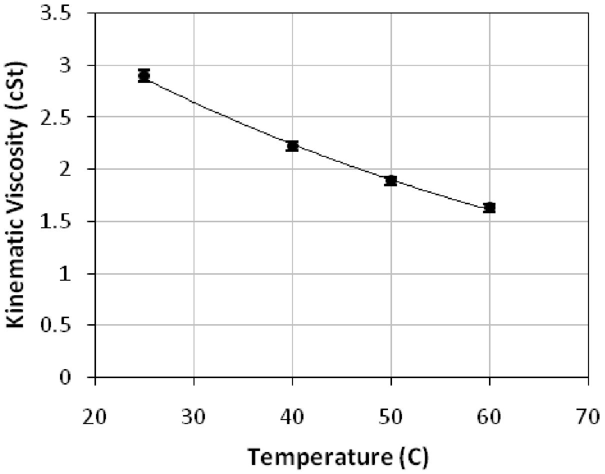

Figure B.11 Kinematic viscosity vs. temperature for canola oil.

- Error bars are sizeable at 25 °C, but are very small at temps above 40 °C
- The data fits fairly well to an exponential decay function

Fuel oil, Canola, and Py oil are plotted against each other

- Put in terms of kinematic viscosity (cSt)because both viscous and inertial (density) forces are significant in sprays

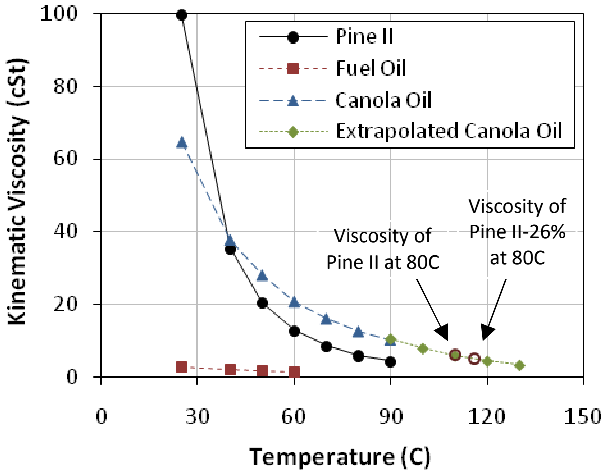

Figure B.12 Kinematic viscosity vs. temperature for BTG Pine 23%, Fuel Oil, and Canola Oil.

- Canola is lower than Pine II at 25 C, but greater at temps above 40
- Canola fits exponential decay whereas Pine II did not
- Pine II oil viscosity changes more significantly at lower temps than predicted by exponential decay function
- All combustion of Pine II oil was run at 80 °C
    - Viscosities of 5.17 and 5.99 cSt for BTG 23 and BTG 26 respectively
    - Corresponds to temperatures of 116 and 110 C for canola oil
    - Could not measure viscosity of canola above 100 C because of device limitations

B.5 Summary of Viscosity Results

1) Pine II behaves as a Newtonian fluid at temperatures between 40 and 90 °C
2) Pine II viscosity is slightly shear thinning and highly dependent upon the sample drawn at 25 °C. For this reason, tests were performed with samples taken from the bottom of the tank which did show consistent and more Newtonian behavior.
3) Pine II viscosity does not follow an exponential decay function well
4) Pine II viscosity is more strongly dependent on temperature than on water content
5) Corn Fraction is highly non-newtonian, both with shear rate and time, with its behavior varying significantly with shear rate and temperature. A great deal more investigation is required to characterize the Corn Fraction behavior.
6) Pine II surface tension decreases linearly with temperature and is not dependent on water content

APPENDIX C. DISCUSSION OF SURFACE TENSION RESULTS

- Glass probe used in place of platinum probe
- Calibration is discussed in methods section of the thesis
- Uncertainties in surface tension measurements represent 68% confidence level (i.e. error bars represent plus or minus one standard deviation)

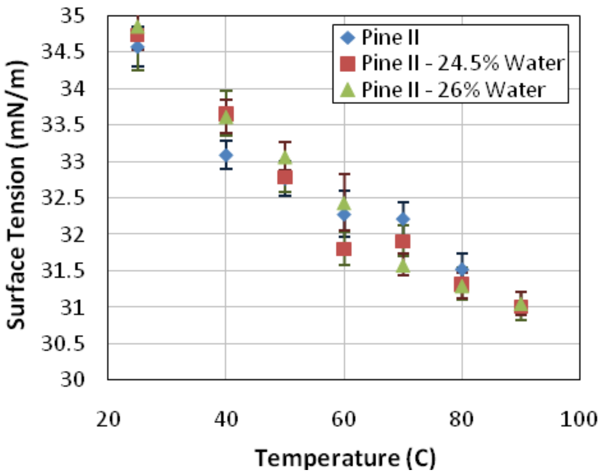

Figure C.1 Surface tension vs. temperature for Pine II samples of varying water content.

- Decrease in surface tension is near linear with temperature
- Error bars do not account for uncertainty in calibration curve(for now, it has been assumed that the calibration curve has zero uncertainty)
- Error is simply from standard deviation in measurements with glass probe

- Do not see any statistical difference between surface tensions as a function of varying water content from 23 to 26%

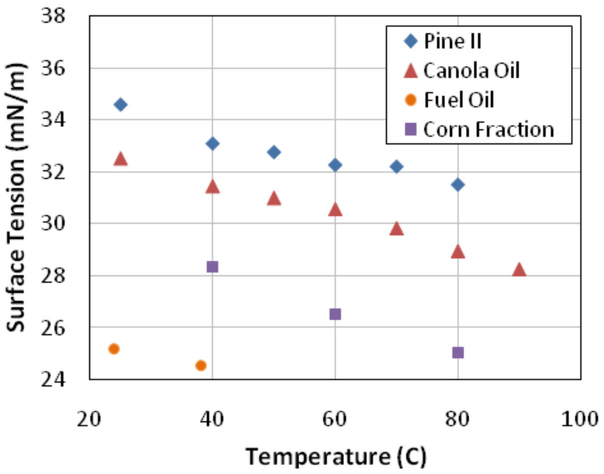

Figure C.2 Surface tension vs. temperature for Pine II, Canola Oil, Fuel Oil, and Corn Fraction oil.

- Canola oil also appears to have a near linear decrease with temperature
- Moreover its values are only approximately 8% lower than the surface tensions measured for pyrolysis oil.
- This, along with the viscosity data, show that canola oil serves well as a surrogate for preliminary evaluations of pyrolysis oil spray studies.

REFERENCES

1. Demirbas, A., *Current Technologies for the Thermo-Conversion of Biomass into Fuels and Chemicals.* Energy Sources, 2004. **26**: p. 715-730.
2. Huber, G.W., S. Iborra, and A. Corma, *Transportation Fuels from Biomass: Chemistry, Catalysts, and Engineering.* Chemical Reviews, 2006. **106**(9): p. 4044-4098.
3. Meier, D. and O. Faix, *State of the Art of Applied Fast Pyrolysis of Lignocellulosic Materials - A Review.* Bioresource Technology, 1999. **68**: p. 71-77.
4. Chiaramonti, D., A. Oasmaa, and Y. Solantausta, *Power generation using fast pyrolysis liquids from biomass.* Renewable and Sustainable Energy Reviews, 2007. **11**: p. 1056–1086.
5. Czernik, S. and A.V. Bridgwater, *Overview of Applications of Biomass Fast Pyrolysis Oil.* Energy & Fuels, 2004. **18**: p. 590-598.
6. Oasmaa, A. and D. Meier, *Characterisation, analysis, norms & standards.* , in *Fast Pyrolysis of Biomass: A Handbook*, A.V. Bridgwater, Editor. 2005, CPL Press: Newbury, UK.
7. Williams, A., *Combustion of Liquid Fuel Sprays*. 1990, Boston: Butterworths.
8. Borman, G.L. and K.W. Ragland, *Combustion Engineering*. 1998, Singapore: McGraw-Hill.
9. Turns, S.R., *An Introduction to Combustion: Concepts and Applications*. 1996, New York: McGraw-Hill.
10. Law, C.K., *Combustion Physics*. 2006, New York: Cambridge University Press.
11. Williams, A., *FUNDAMENTALS OF OIL COMBUSTION.* Progress in Energy and Combustion Science, 1976. **2**(3): p. 167-179.
12. Chiu, H.H., H.Y. Kim, and E.J. Croke. *Internal Group Combustion of Liquid Droplets*. in *Nineteenth Symposium (International) on Combustion*. 1982: The Combustion Institute.
13. Onuma, Y. and M. Ogasawara. *Studies on the Structure of a Spray Combustion Flame*. in *Fifteenth Symposium (International) on Combustion*. 1975: The Combustion Institute.
14. Onuma, Y., M. Ogasawara, and T. Inoue. *Further Experiments on the Structure of a Spray Combustion Flame*. in *Sixteenth Symposium (International) on Combustion*. 1977: The Combustion Institute.
15. Burgoyne, J.H. and L. Cohen, *The Effect of Drop Size on Flame Propagation in Aerosols.* Proceedings of the Royal Society A, 1954. **225**: p. 375-392.
16. LeFebvre, A.H., *Fuel Atomization, Droplet Evaporation, and Spray Combustion*, in *Fossil Fuel Combustion: A Source Book*, W. Bartok and A.F. Sarofim, Editors. 1991, John Wiley & Sons, Inc.: New York. p. 529-652.
17. Lefebvre, A., *Atomization and Sprays*. 1988: Hemisphere Pub Combustion: An International Series.
18. Kuo, K.K., *Principles of Combustion*. 2005, New York: John Wiley & Sons.

19. Gupta, A.K., D.G. Lilley, and N. Syred, *Swirl Flows*. 1984, Turnbridge Wells: Abacus Press.
20. Bowman, C.T., *Chemistry of Gaseous Pollutant Formation and Destruction*, in *Fossil Fuel Combustion: A Source Book*, W. Bartok and A.F. Sarofim, Editors. 1991, John Wiley & Sons, Inc.: New York. p. 529-652.
21. Haynes, B.S., *Soot and Hydrocarbons in Combustion*, in *Fossil Fuel Combustion: A Source Book*, W. Bartok and A.F. Sarofim, Editors. 1991, John Wiley & Sons, Inc.: New York. p. 261-326.
22. Warnatz, J., U. Maas, and R.W. Dibble, *Combustion: Physical and Chemical Fundamentals, Modeling and Simulation, Experiments, Pollutant Formation*. 2001, New York: Springer.
23. Brown, R.C., *Biorenewable Resources: Engineering New Products from Agriculture*. 2003, Ames, IA: Blackwell Publishing Co.
24. Longwell, J.P., *Interface Between Fuels and Combustion*, in *Fossil Fuel Combustion: A Source Book*, W. Bartok and A.F. Sarofim, Editors. 1991, John Wiley & Sons, Inc.: New York. p. 3-48.
25. www.epa.gov.
26. Corporan, E., et al., *Emissions Characteristics of a Turbine Engine and Research Combustor Burning a Fischer-Tropsch Jet Fuel.* Energy & Fuels, 2007. **21**: p. 2615-2626.
27. Huffman, D.R., A.J. Vogiatzis, and D.A. Clarke, *Combustion of Bio-Oil*, in *Bio-Oil Production and Utilization*, A.V. Gridgwater and E. Hogan, Editors. 1996, CPL Press. p. 227-235.
28. Preto, F., P.E.G. Gogolek, and J.K.L. Wong, *Nozzle Testing and Development for Bio-Oil Combustion*, in *Science in Thermal and Chemical Biomass Conversion*, A.V. Bridgwater and D.G.B. Boocock, Editors. 2006, CPL Press. p. 1480-1490.
29. VanDeKamp, W.L. and J.P. Smart, *Atomisation and Combustion of Slow Pyrolysis Oils*, in *Advances In Thermochemical Conversion*, A.V. Bridgwater, Editor. 1994, Blackie Academic & Professional. p. 1265-1274.
30. Oasmaa, A. and S. Czernik, *Fuel Oil Quality of Biomass Pyrolysis Oils*, in *Biomass: A Growth Opportunity in Green Energy and Value-Added Products*, R.P. Overend and E. Chornet, Editors. 1999, Elsevier. p. 1247-1252.
31. Oasmaa, A. and S. Czernik, *Fuel Oil Quality of Biomass Pyrolysis Oils - State of the Art for End Users.* Energy & Fuels, 1999. **13**: p. 914-921.
32. Oasmaa, A. and D. Meier, *Analysis, Characterisation and Test Methods of Fast Pyrolysis Liquids*, in *Biomass: A Growth Opportunity in Green Energy and Value-Added Products*, R.P. Overend and E. Chornet, Editors. 1999, Elsevier. p. 1229-1234.
33. Oasmaa, A., et al., *Norms and Standards for Pyrolysis Liquids. End-User Requirements and Specifications.* Energy & Fuels, 2005. **19**(5): p. 2155–2163.
34. Gust, S., *Combustion Experiences of Flash Pyrolysis Fuel in Intermediate Size Boilers*, in *Developments in Thermochemical Biomass Conversion*, A.V. Bridgwater and D.G.B. Boocock, Editors. 1997, Blackie Academic & Professional. p. 481-488.
35. Gust, S., *Combustion of Pyrolysis Liquids*, in *Biomass Gasification and Pyrolysis, State of the Art and Future Prospects*, M. Kalschmitt and A.V. Bridgwater, Editors. 1997, CPL Press. p. 498-503.

36. Shihadeh, A., et al. *Combustion Characterization of Wood-Derived Flash Pyrolysis Oils in Industrial-Scale Turbulent Diffusion Flames*. in *Proceedings of Biomass Pyrolysis Oil Properties and Combustion Meeting*. 1994. Estes Park, CO.
37. Branca, C., C. Di Blasi, and R. Elefante, *Devolatilization and heterogeneous combustion of wood fast pyrolysis oils.* Industrial and Engineering Chemistry Research, 2005. **44**(4): p. 799-810.
38. Moses, C. *Fuel-Specification Considerations for Biomass Liquids*. in *Proceedings of Biomass Pyrolysis Oil Properties and Combustion Meeting*. 1994. Estes Park, CO.
39. Czernik, S., D.K. Johnson, and S. Black, *Stability of Wood Fast Pyrolysis Oil.* Biomass and Bioenergy, 1994. **7**: p. 187-192.
40. Solantausta, Y., et al., *Wood Pyrolysis Liquid as Fuel in a Diesel Power Plant.* Bioresource Technology, 1993. **46**(1-2): p. 177-88.
41. Solantausta, Y., et al. *Preliminary Tests with Wood-Derived Pyrolysis Liquid as Fuel in a Stationary Diesel Engine*. in *Biomass Pyrolysis Liquid Properties and Bomsution Meeting*. 1994. Estes Park, CO.
42. Shihadeh, A. and S. Hochgreb, *Diesel engine combustion of biomass pyrolysis oils.* Energy and Fuels, 2000. **14**(2): p. 260-274.
43. Shihadeh, A. and S. Hochgreb, *Impact of Biomass Pyrolysis Oil Process Conditions on Ignition Delay in Compression Ignition Engines.* Energy & Fuels, 2002. **16**: p. 552-561.
44. Gros, S. *Pyrolysis Liquid as Diesel Fuel*. in *Seminar on Power Production from Biomass II*. 1995. Espoo, Finland.
45. Jay, D., et al. *Wood Pyrolysis Oil for Diesel Engines*. in *1995 Fall Technical Conference*. 1995. Milwaukee, WI: ASME.
46. Andrews, R.G., et al., *Results of Industrial Gas Turbine Tests Using a Biomass-Derived Fuel*, in *Making a Business from Biomass in Energy, Evironment, Chemicals, Fibers, and Materials*, R.P. Overend and E. Chornet, Editors. 1997, Pergamon. p. 425-435.
47. Kasper, J.M., G.B. Jasas, and R.L. Trauth, *Use of Pyrolysis Derived Fuel in a Gas Turbine Engine.* ASME Paper, 1983. **83-GT-96**.
48. Strenziok, R., U. Hansen, and H. Kunstner, *Combustion of Bio-Oil in a Gas Turbine*, in *Progress in Thermochemical Biomass Conversion*, A.V. Bridgwater, Editor. 2001, Blackwell Science Ltd. p. 1452-1458.
49. Andrews, R., et al. *Firing Fast Pyrolysis Oil in Turbines*. in *Biomass Pyrolysis Oil Properties and Combustion Meeting*. 1994. Estes Park, CO.
50. Andrews, R.G., S. Zukowski, and P.C. Patnaik, *Feasibility of Firing and Industrial Gas Turbine Using a Bio-Mass Derived Fuel*, in *Developments in Thermochemical Biomass Conversion*, A.V. Bridgwater and D.G.B. Boocock, Editors. 1997, Blackie Academic & Professional. p. 495-506.
51. Lopez Juste, G. and J.J. Salva Monfort, *Preliminary test on combustion of wood derived fast pyrolysis oils in a gas turbine combustor.* Biomass and Bioenergy, 2000. **19**(2): p. 119-128.
52. Kyto, M., P. Martin, and S. Gust, *Development of Combustors for Pyrolysis Liquids*, in *Pyrolysis and Gasification of Biomass and Waste*, A.V. Bridgwater, Editor. 2003, CPL Press. p. 187-190.

53. Oasmaa, A., M. Kyto, and K. Sipila, *Pyrolysis Oil Combustion Tests in an Industrial Boiler*, in *Progress in Thermochemical Biomass Conversion*, A.V. Bridgwater, Editor. 2001, Blackwell Science Ltd. p. 1468-1481.
54. Rossi, C., et al., *Combustion Tests of Bio-Oils Derived From Biomass Slow Pyrolysis*, in *Advances In Thermochemical Conversion*, A.V. Bridgwater, Editor. 1994, Blackie Academic & Professional. p. 1205-1213.
55. VanDeKamp, W.L. and J.P. Smart, *Evaluation of the Combustion Characteristic of Pyrolytic Oil Derived from Biomass*, in *Proceedings of Energy from Biomass Contractors' Meeting*. 1991: Florence, Italy.
56. Solantausta, Y., et al., *Low Boiler Emissions with a Cost Competitive Liquid Biofuel*, in *2nd World Conference and Technology Exhibition on Biomass for Energy, Industry and Climate Protection Rome*. 2004: Rome, Italy.
57. Wickboldt, P., R. Strenziok, and U. Hansen, *Investigation of Flame Characteristics and Emission of Pyrolysis Oil in a Modified Flame Tunnel*, in *Biomass: A Growth Opportunity in Green Energy and Value-Added Products*, R.P. Overend and E. Chornet, Editors. 1999, Elsevier. p. 1241-1246.
58. Huffman, D.R., A.J. Vogiatzis, and A.V. Bridgwater, *The Characterization of Fast Pyrolysis Bio-Oils*, in *Advances in Thermochemical Conversion of Biomass*, A.V. Bridgwater, Editor. 1994, Blackie Academic & Professional: Glasgow. p. 1095-1102.
59. Li, Y.-H., A.P. Watkinson, and P.V. Barr, *Firing a Pilot Lime Kiln with Bio-Oil*, in *Science in Thermal and Chemical Biomass Conversion*, A.V. Bridgwater and D.G.B. Boocock, Editors. 2006, CPL Press. p. 1491-1503.
60. Stamatov, V., et al., *Origin of NOx Emission from Bio-Oil Flames*, in *Science in Thermal and Chemical Biomass Conversion*, A.V. Bridgwater and D.G.B. Boocock, Editors. 2006, CPL Press. p. 1504-1510.
61. Stamatov, V., D. Honnery, and J. Soria, *Combustion properties of slow pyrolysis bio-oil produced from indigenous Australian species.* Renewable Energy, 2006. **31**(13): p. 2108-2121.
62. Bandi, A. and F. Baumgart, *Stirling Engine with FLOX Burner Fuelled with Fast Pyrolysis Liquid*, in *Progress in Thermochemical Biomass Conversion*, A.V. Bridgwater, Editor. 2001, Blackwell Science Ltd. p. 1459-1467.
63. Calabria, R., F. Chiariello, and P. Massoli, *Combustion fundamentals of pyrolysis oil based fuels.* Experimental Thermal and Fluid Science, 2007. **31**: p. 413–420.
64. D'Alessio, J., et al., *Thermo-Optical Investigation of Burning Biomass Pyrolysis Oil Droplets*, in *27th Symposium (International) on Combustion/The Combustion Institute*. 1998.
65. Shaddix, C.R. and S.P. Huey, *Combustion Characteristics of Fast Pyrolysis Oils Derived From Hybrid Poplar*, in *Developments in Thermochemical Biomass Conversion*, A.V. Bridgwater and D.G.B. Boocock, Editors. 1997, Blackie Academic & Professional. p. 465-480.
66. Shaddix, C.R. and P.J. Tennison, *Effects of char content and simple additives on biomass pyrolysis oil droplet combustion.* Proceedings of the 1998 27th International Symposium on Combustion, 1998. **2**: p. 1907-1914.
67. Wornat, M.J., B.G. Porter, and N.Y.C. Yang, *Single droplet combustion of biomass pyrolysis oils.* Energy & Fuels, 1994. **8**(5): p. 1131-1142.

68. Garcia-Perez, M., et al., *Spray Characterization of a Softwood Bark vacuum Pyrolysis Oil*, in *Science in Thermal and Chemical Biomass Conversion*, A.V. Bridgwater and D.G.B. Boocock, Editors. 2006, CPL Press. p. 1468-1479.
69. Wiemer, H.-J., et al., *Spray Characteristics for the Gasification of Pyrolysis Oil Slurries*, in *Science in Thermal and Chemical Biomass Conversion*, A.V. Bridgwater and D.G.B. Boocock, Editors. 2006, CPL Press. p. 1559-1564.
70. Oasmaa, A. and D. Meier, *Analysis, Characterisation and Test Methods of Fast Pyrolysis Liquids*, in *Fast Pyrolysis of Biomass: A Handbook*. 2002, CPL Press: Newbury, UK. p. 1229-1234.
71. Rover, M., *Personal Communication*. 2009.
72. *AVL 415S Variable Sampling Smoke Meter Operating Manual*. 2005, AVL List GmbH.
73. *Phase Doppler Particle Analyzer (PDPA)/ Laser Doppler Velocimeter (LDV) Operations Manual*. 2005, TSI Incorporated.
74. Meyer, T.R., et al., *Optical Diagnositcs and Numerical Characterization of a Trapped-Vortex Combustor*, in *38th AIAA/ASME/SAE/ASEE Joint Propulsion Conference and Exhibit*. 2002, AIAA: Indianapolis, IN.
75. Eckbreth, A.C., *Laser Diagnostics for Combustion Temperature and Species*. 1988, Cambridge: Abacus Press.
76. Meyer, T.R., et al., *Simultaneous Planar Laser-Induced Incandescence, OH Plana Laser-Induced Fluorescence, and Droplet Mie Scattering in Swirl-Stabilized Spray Flames.* Applied Optics, 2005. **44**(3): p. 445-454.
77. Miller, J.D. and T. Meyer, *Personal Communication*. 2009.
78. Brewer, C.E., et al., *Characterization of Biochar from Fast Pyrolysis and Gasification Systems.* Environmental Progress & Sustainable Energy, 2009. **[accepted for publication]**.
79. White, F.M., *Fluid Mechanics*. 5th ed. 2003, Boston: McGraw Hill.
80. Perry, R.H. and D.W. Green, *Perry's Chemical Engineer's Handbook*. 7th ed. 1997, New York: McGraw-Hill.

ACKNOWLEDGEMENTS

ConocoPhillips

Daren Daugard
Kristi Fjare
Lisa Myers

Faculty

Robert C. Brown (Co-major Professor)
Terrence R. Meyer (Co-major Professor)
Song-Charng Kong (Committee Member)
Brent Shanks (Committee Member)
Hui Hu (Committee Member)
Theodore Heindel

Post-Doctoral Researchers

Mikhail Slipchenko
Aravind Vaidyanathan

Graduate Students

Catherine Brewer
Mark Cecconi
Joseph Fuller
Praveen Kumar
Najeeb Kuzhiyil
Patrick Meehan
Joseph Miller
Anthony Phan
Marge Rover
Tim Rovince
Matthias Veltman

Undergraduate Students

Chloe Dedic
Tyler Dorin
Ben Franzen
Anthony Lanphier
Juston Lisk
Seth Nelson
David Prater
Travis Presto
Kyle Redfern
Katherine Schuller

Staff

Jim Dautremont
Warren Straszheim